UNIVERSITY OF CAPE COAST

RELATIONSHIP BETWEEN RECENT RAINFALL REGIME CHARACTERISTICS OVER SOUTHERN WEST AFRICA AND ASSOCIATED MESOSCALE CONVECTIVE SYSTEMS

BY

FRANCIS NKRUMAH

Thesis submitted to the Department of Physics of the School of Physical Sciences, College of Agriculture and Natural Sciences, University of Cape Coast, in partial fulfilment of the requirements for the award of Doctor of Philosophy Degree in Physics

JULY 2020

DECLARATION

Candidate's Declaration

I hereby declare that this thesis is the result of my own original research and that no part of it has been presented for another degree in this university or elsewhere.

..... Date: .....

Francis Nkrumah
(Candidate)

Supervisors' Declaration

We hereby declare that the preparation and presentation of the thesis were supervised in accordance with the guidelines on supervision of thesis laid down by the University of Cape Coast.

..... Date: .....
Dr. Nana Ama Browne Klutse

(Principal Supervisor)

..... Date: .....
Dr. Alfred Owusu

(Co-Supervisor)

..... Date: .....
Prof. Theo Vischel

(Co-Supervisor)

ABSTRACT

Extreme climate events, either being linked to dry spells or extreme precipitation, are of major concern in Africa, a region in which the economy and population are highly vulnerable to climate hazards. However, recent trends in climate events are not often documented in this poorly surveyed continent. Changes in surface temperature gradients and associated changes in wind shear have been found to be important for MCS intensification in recent decades. This analysis was extended to Southern West Africa (SWA) by combining 34 years of cloud-top temperatures with rainfall and reanalysis data. This study makes use of a large set of daily rain gauge data covering Southern West Africa (extending from 10° W to 10° E and from 4° N to 12° N) from 1950 to 2014. The evolution of the number and the intensity of daily rainfall events, especially the most extremes, were analyzed at the annual and seasonal scales. The north–south seasonal changes exhibit an increase in mean annual rainfall over the last decade during the second rainy season (September–November) linked by both an increase in the frequency of occurrence of rainy days as well as an increase in the mean intensity and extreme events over the last decade. Over the south-north gradient of West Africa, mesoscale convective systems (MCSs) tend to be responsible for the majority of annual rainfall. Trends in intense MCS correlate well with intense rainfall in both rainfall seasons over Southern West Africa. Coldest cloud tops (intense MCSs) tend to be modulated by positive trends in wind shear during the first rainy season and by the availability of moisture in the second rainy season, although both rainy seasons occur mainly under similar conditions.

KEYWORDS

Rainfall regime

Southern West Africa

Extreme events

Mesoscale Convective System

Storms

Mean rainfall intensity

Vertical wind shear

Shear-regime

Moisture-regime

African easterly jet

West african monsoon

Diurnal cycle

ACKNOWLEDGEMENTS

Foremost I would like to sincerely thank my supervisors, Dr. Nana Ama Browne Klutse, Dr. Alfred Owusu and Prof. Theo Vischel for their encouragement, tremendous mentoring, insightful supervision, valuable guidance, scholarly inputs, support and numerous helpful discussions from the beginning and completion of this project. The entire experience has been truly rewarding, as far as the learning process is concerned.

I would especially like to express my sincere appreciation to Dr. Geremy Panthou from the Institute of Environmental Geosciences, which is a Research Unit of CNRS, Grenoble INP, IRD and Université Grenoble Alpes in France, and also Prof. Christopher Taylor and Dr. Cornelia Klein from the Centre for Ecology and Hydrology, Wallingford, UK for their technical assistance and also giving me the opportunity to use their lab through the AMMA 2050 project.

Many thanks Mr. David Adukpo for his immense support throughout my period of study. My Thanks also go to all Professors, lecturers and staff, both teaching and non-teaching of the Department of Physics for their support. My appreciation to all members of MAP research group for their support in various ways at various points of my research programme.

I am much indebted to my wife, Frances, and my mum for their unparalleled sacrifices, spiritual and moral support in this feat. My sincere thanks go to all friends who were behind my progress throughout my studies. Pardon me if I did not mention your name.

DEDICATION

To my family for their constant support and unconditional love. I love you all dearly.

TABLE OF CONTENTS

LIST OF TABLES

LIST OF FIGURES

LIST OF ABBREVIATIONS

ITCZ	Intertropical Convergence Zone
SWA	Southern West Africa
WAM	West African Monsoon
MCS	Mesoscale Convective System
CAPE	Convective Available Potential Energy
MW	Microwave
IR	Infra-Red
BSR	Bi-Spectral Reflectance
CTT	Cloud Top Temperature
CTH	Cloud Top Height
ITD	Intertropical Discontinuity
ACT	Atlantic Cold Tongue
SHL	Saharan Heat Low
AEJ	African Easterly Jet
TEJ	Tropical Easterly Jet
SST	Sea Surface Temperature
AMJJ	April-May-June-July
SON	September-October-November
PV	Potential Vorticity
MFC	Moisture Flux Convergence
MSE	Moist Static Energy

CHAPTER ONE

INTRODUCTION

In a context where global warming is leading to a global intensification of the hydrological cycle, there is an urgent need to understand how this intensification takes place at regional scales and what is its link with regional climate structures. There is an urgent need for the understanding of how the intensification in recent rainfall events relate with the larger-scale climate. This thesis seeks to establish the observed characteristics and changes in the rainfall regime over Southern West Africa (SWA) and its relationship with trends in storm systems. It gives an overview of extreme rainfall events and the general climate of SWA using observed station data from 97 stations across SWA between 1970 and 2014. Various statistical and dynamical methods to assess rainfall events were used, and the related dynamics of Mesoscale Convective Systems (MCSs) were determined for rainfall intensification over the SWA. The frequency and spatial distribution of trends in MCSs are correlated with rainfall events to determine their relationship. Sensitivity analysis of the dynamics of MCSs are carried out to understand the different convective regimes that control the two rainy seasons over SWA. The following sections provide a background to the central theme, the rationale and justification of the thesis.

Background

West Africa marks the westernmost part of the African continent between 15°E - 16°W and 4°N - 28°N, lying north of the Gulf of Guinea and extending into the central Sahara. It consists of 16 countries with Liberia,

Ivory Coast, Ghana, Togo, Benin and Nigeria constituting the southern boundary. From the Guinean Coast to the Sahara desert, West Africa is characterized by east-west oriented climate zones. These climatic zones can be divided into four main regions: the tropical Guinea coast, the sub-humid Sudano-Sahel, the semi-arid Sahel and the Saharan desert in the North (Meynadier et al., 2010). The region of West Africa is subject to variabilities in rainfall on both spatial and temporal scales. Fundamentally, the rainfall pattern in West Africa is modulated by the annual change in the position of the ITCZ. Two types of annual cycles of precipitation persist in West Africa; a bimodal cycle south of 10°N and a unimodal cycle north of 10°N (Hayward & Oguntoyinbo, 1987). Figure 1 is part of the African map showing the Sahelian region and the Guinea coast region of West Africa. Focusing on the Guinea Coast region (4°N - 12°N), hereafter referred to as SWA, the seasons in SWA are characterized by two distinct rainfall patterns: a Sudanian climate, with one wet and one dry season in the northern part (~10°N) and a Guinean climate with two wet (bimodal) seasons in the southern part, also called the forest zone (Nguyen et al., 2011). The Sudanian rainfall season which is characterized by a unimodal rainfall regime extends from mid-March to the end of October (Yabi & Afouda, 2012) and peaks during the months of July and August.

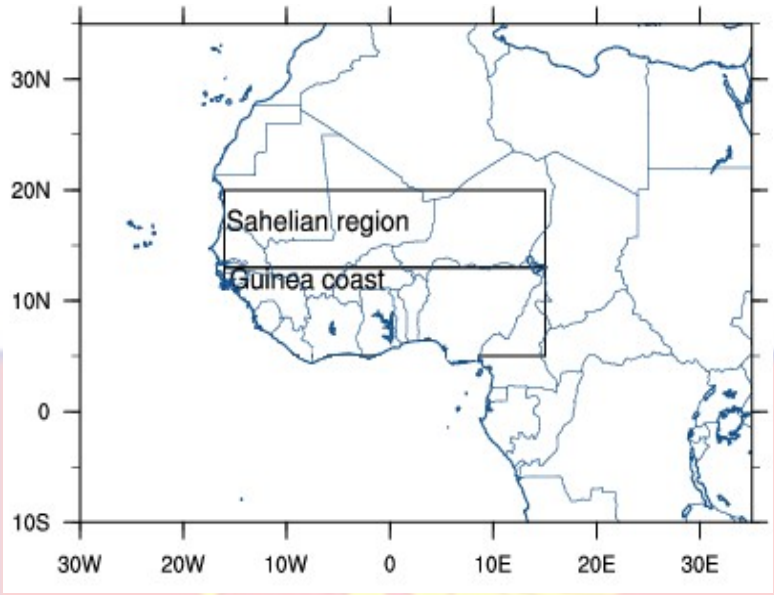

Figure 1: Map of part of Africa showing the Sahelian region and the Guinea Coast region of West Africa.

The southern part of SWA exhibits a humid to sub-humid climate with a bimodal rainfall distribution featuring two distinct rainy seasons related to the inland progression of the intertropical convergence zone (ITCZ) during March to June and its equatorward retreat between September and November, with different patterns over its coast and the inland region. This area where the seasonal cycle is bi-modal rarely moves beyond 7° N or 8° N (Balme-Debionne, 2004).

Figure 2 illustrates the point on some stations with relatively long data (over 40 years). They illustrate the cycle change in seasonal shift from a uni-modal cycle in the North (Sudanian region) to a bi-modal cycle in the south of the zone. Generally, the West African rainfall is basically controlled by the West African Monsoon (WAM) system and is known to undergo year to year and decadal time-scale changes (Diatta & Fink, 2014).

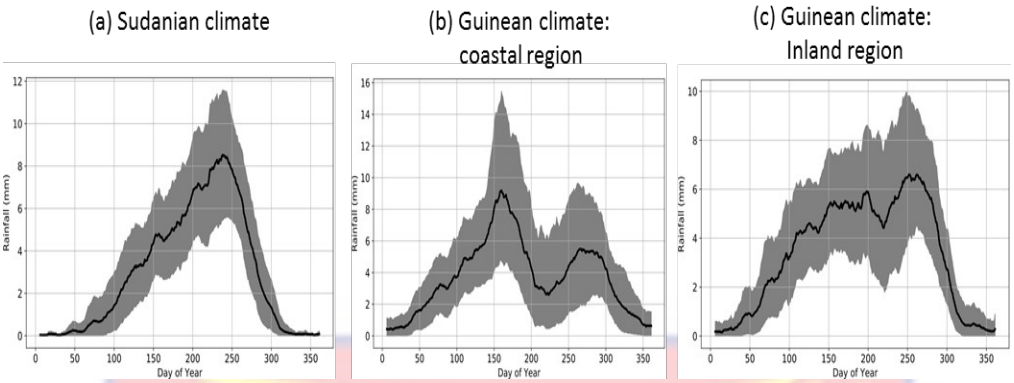

Figure 2. Graphs showing the seasonal cycle of rainfall over the (a) Sudanian climate, (b) Guinean climate: Coastal region and (c) Guinean climate: Inland region of SWA at 11 days moving average of the cumulative julian days for the period 1950-2014

The Coastal region displays a bi-modal rainfall cycle exhibiting a clear major rainy season which peaks in June and a minor maximum in September and October during the return of the rainbelt to the south, with some areas receiving in excess of 2000 mm of rainfall each year (Figure 3).

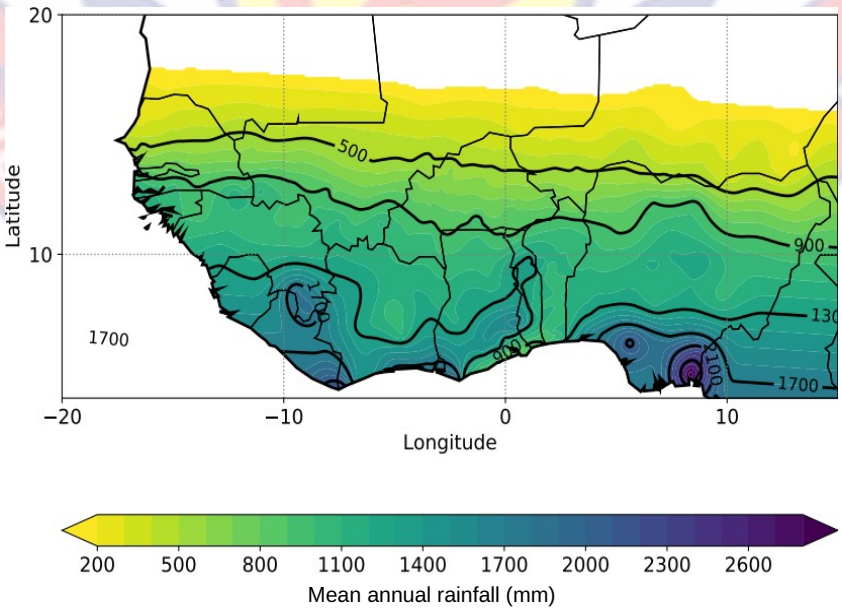

Figure 3. Average annual rainfall calculated over the period 1970 - 2015 using universal kriging (data presented in Chapter 3).

Figure 3 shows that the southern stations are wetter than the northern ones. The difference between these two rainfall seasons come from the phase of the monsoon (Le Barbé et al., 2002; Lebel et al., 2003). An “ocean phase” which is initiated on the coastal regions, with the monsoon sinking fast enough on the continent (monsoon jump) then enters the “continental phase” which bring rains to the most northerly regions (while the coastal areas are in the short dry season) and then retreat to the ocean by watering the southern regions that will observe a second rainy season. The first rainy season is marked by the wetting-up of soils, creating a conducive environment for strong surface temperature gradients, whilst during the retreat of the monsoon rainband a weaker effect with a declining effect on storms could be expected. The region located between 7°N - 8°N and 10°N - 12°N are influenced by both phases and have cycles that can be more complex. A local minimum is observed in August, marking the so-called “little dry season” (Le Barbé et al., 2002; Nicholson, 1981). This so-called “little dry season” is a tract of savannah with relatively little rain, which stretches from the coast of central Ghana running east through Togo and Benin. Over the studied region, it has been observed that rainfall totals of the 1970s and 1980s were ~200mm less as compared to events of the 1950s and 1960s (Le Barbé et al., 2002). Events such as droughts and floods are so distinct, that they not only whipped up international interests to food security and human displacement issues in these areas, but also triggered the interest of atmospheric scientists to investigate the mechanisms responsible for the atypical events and possibly their predictability. Observations also indicated that annual rainfall totals exceeding the annual average have been occurring more frequently in the 2000s.

WAM might be the most remarkable feature of the West African weather. Seasonal rains travel northward from the Guinean coast to the Sahel and back yet again from late March to October over the subcontinent (Figure 4).

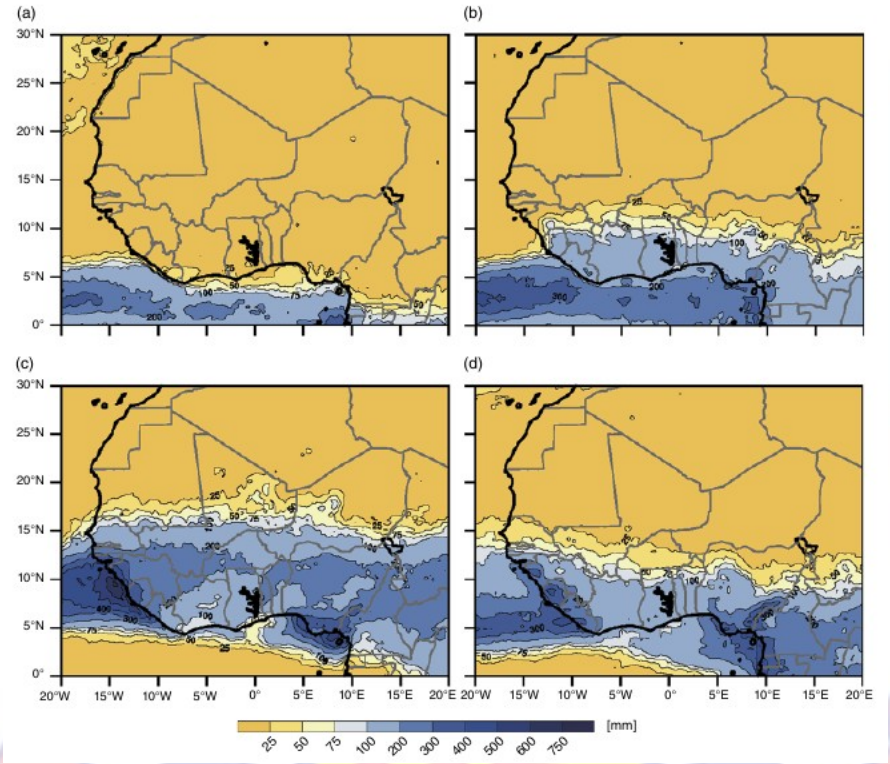

Figure 4. Mean monthly rainfall for (a) January (b) April (c) July and (d) October. Source: TRMM 3B42 Version 7, 1998-2012.

The WAM, which accounts for the majority of the annual precipitation, is of paramount importance to the population of West Africa that massively rely on rain-fed agriculture for survival. Due to the prevalence of smallholder farming and rain-fed agriculture in West Africa, delayed onsets of the monsoon rains, monsoon breaks, flash floods, larger-scale seasonal inundations and longer-term droughts have large socio-economic impacts. West Africa was identified as one of the worlds most vulnerable regions to climate change because of the combination of endemic poverty, complex

governance, insufficient infrastructure and technology, strong population growth and an extreme variability of the WAM (Change, 2014).

Relationship between rainfall events and MCSs

Understanding how intense rain events relate with the larger-scale climate has been a major challenge for researchers due to the inability of existing coarse resolution models to resolve convective rainfall systems. Since about 1950, there has been strong evidence for extreme rainfall events becoming more frequent than expected from natural variability alone (I.P.C.C., 2013; Min et al., 2011). The scientific community, therefore, faces an urgency of informing the society with expected changes in climatic conditions and high impact weather events in the future. The predictions of more frequent floods (Kundzewicz et al., 2013) and the increased frequency of extreme rainfall in many parts of the world due to global warming (Donat et al., 2016) send possible signals of an intensification of the global hydrological cycle (Huntington, 2006; Kingston et al., 2009; Murray et al., 2011). A large body of research work has looked into understanding observational trends in extreme rainfall (Min et al., 2011; Panthou et al., 2018; Panthou et al., 2014; Westra et al., 2013) and future projections in intense rain (O'Gorman, 2015; Westra et al., 2014). Most of the problems in the physical understanding of the changes in the rainfall regime come from mesoscale convective systems (Houze Jr, 2004). Over the south-north gradient of West Africa, MCSs are responsible for the majority of annual rainfall (Fink & Reiner, 2003; Laing et al., 1999). Previous studies have highlighted that a large portion of extreme rainfall events result from mesoscale convective systems (Maddox, et al.,

1979; Schumacher & Johnson, 2005, 2006), with highly organized MCSs being the major rain-bearing systems across much of tropical Africa (Jackson et al., 2009; Nesbitt et al., 2006). A lot of attention has been given to understanding the dynamics and climatology of MCSs due to the fact that they contribute to about 90% of the annual rainfall in the West African Sahel (Nicholson, 2013) and also produce about 56% of the annual rainfall in the Guinea Coast (Maranan et al., 2018). The nature of intra-seasonal rainfall variability has changed over the Sahel however, with a recent increase in the frequency of very intense MCSs separated by longer periods of little to no rainfall (Panthou et al., 2014; Taylor et al., 2017).

Past studies have also indicated an increasing role of other types of less-organized rainfall at the expense of MCSs towards the Guinea Coast (e.g. (Acheampong, 1982; Fink et al., 2006; Kamara, 1986; Omotosho, 1985), with little said about the thermodynamic environments in which they occur. Recent studies have provided rationale behind why the Sahelian MCSs are becoming more intense over the region presently, with (Taylor et al., 2017) associating the intensification to a threefold increase in the frequency of cold cloud-top MCSs over the Sahel since the early 1980s with an intensification of midday zonal wind shear. Zonal wind shear is seen to be very critical to the organization of convective systems through its ability to modulate the storm-available supply of moist buoyant air (Alfaro, 2017; Mohr & Thorncroft, 2006).

Topographic features such as the Cameroon Highlands, Ethiopian Highlands, Guinean Highlands, Jos Plateau and the Marra Mountains tend to be conducive areas for the formation of MCSs with basically westward

propagation and life spans ranging between a few hours to about 3 days (Fink et al., 2006; Mohr, 2004). The genesis of MCS occurs more frequently in the afternoon, while the associated rainfall has the tendency of becoming heavier during the early hours of the evening when the systems are mostly in their mature stage. Propagating storms with longer-lasting organized precipitation systems tend to be associated with higher values of convective available potential energy (CAPE) and strong vertical wind shear (Hodges & Thorncroft, 1997; Laing et al., 2008; Mohr & Thorncroft, 2006).

Motivation

Over the Sahel, increments observed in the frequency and trends in very intense MCSs correlate with the intra-seasonal variability of rainfall (Taylor et al., 2017). Despite their importance, trends in these cloud systems and their relationship to rainfall regime remain very poorly predicted in SWA.

Objectives

The major objective of this research is to improve our knowledge and understanding of the characteristics and changes in the rainfall regime in SWA. Specific objectives that form the basis of this thesis are:

1. To determine the presence of an intensification in the rainfall regime over SWA as observed in the Sahel.

2. To examine the interannual variability and trends in MCSs and their drivers.

3. To understand the relationship between trends in storm frequency and rainfall over Southern West Africa.

4. To characterize the effect of pre-storm environmental conditions on storm systems

For the entirety of this study, “pre-storm” environment refers to the region ahead of the convective system, which provides source air to the storm.

Thesis structure

This thesis is composed of five chapters. This introductory chapter outlines the motivation for this research and gives an overview of the recent rainfall events, its relationship with MCS and the general SWA climate. The motivation of the work and the arrangement of the thesis are also included in this chapter. Chapter two reviews literature on rainfall and its formation, large-scale drivers modulating rainfall over the West African region, MCSs, environmental setup for MCSs and its connection to tropical rainfall. Chapter three addresses the different dataset and the various methods used for the research work. The observed characteristics and changes in the rainfall regime over SWA and its relationship with trends in storm systems with the various dynamics controlling the convective regime in both rainy seasons are presented in Chapter four. Chapter five summarizes the findings, concludes the thesis and proposes future work in this area of study.

Chapter Summary

This chapter looked at the background of the changing rainfall regime over the SWA, characterizing these changes with frequency trends in MCSs and storm environmental conditions suitable for the formation of more intense storms. It also captured the motivation and objectives of the thesis.

CHAPTER TWO

LITERATURE REVIEW

Introduction

Rainfall variabilities, have over the years, contributed greatly to some of the most destructive natural disasters and continue to be a socio-economic menace to activities in the West African region (Hountondji et al., 2011). Within the scope of this work, it is critical to know changes in rainfall fluctuations and the attributes of weather features leading to the changes. This chapter provides a summary of rainfall variability in West Africa.

Formation of Rainfall

In order for rainfall to form, saturated air is heated (air cools down at dew point) and rises either by conventional currents, frontal action or against a mountain (Selase et al., 2015). The lifting air cools down as it rises. The air molecule attaches itself to tiny particles of dust and other particles in the atmosphere. These particles are commonly referred to as condensation nuclei. Condensation occurs when water droplets are attached to the surfaces of condensation nuclei to form raindrops. The development of rain drops happen as a result of cloud formation. Clouds become heavy and unstable as it progresses and cools down at the dry adiabatic rate. This adiabatic rate implies that for every 100 metres rise, there is a one degree Celsius of cooling in the temperature of water droplets (Selase et al., 2015). As the air rises, it cools and reaches its dew point. The formation of clouds can then take place due to the existence of condensation. Thus, clouds are formed when there is condensation of a parcel of air reaching its dew point. The rising clouds

become warmer than the surrounding air as the adiabatic lapse rate actual temperature becomes higher than the dew point. This makes the cloud unstable. As it develops further, it becomes very heavy and falls to the ground as rain. Factors responsible for the lifting of the saturated air brings about the different types of rain. Each type of rainfall requires a different mechanism that triggers the vertical movement of unstable air.

Types Of Rainfall

For both condensation and precipitation to take place there must be an appreciable lifting of an air mass. Since this lifting is brought about in three different ways, there are three classifications of rainfall types. These are: Convectional, Orographic or Relief and Frontal or Cyclonic Rainfall. Over West Africa, this system of classification is inadequate in terms of current knowledge of the region's precipitation dynamics. To begin with, West Africa has not recorded activity of cyclonic or frontal activity (Friesen & Diekkriuger, 2002). Also, large amounts of rainfall are observed to be produced by atmospheric processes aside from convection and orographic uplift. In some areas over 50 per cent of the total annual rainfall is derived from these extra sources. Over the West African region, there exist three rainfall origins: the convective systems which are divided into local rainstorms and MCSs as well as convergence rainfall from monsoonal air layers.

Convectional Rainfall

Convectional rainfall takes place when the surface of the earth is heated by the energy from the sun, causing water on the surface to evaporate to form water vapour (Figure 5). The air, which has become lighter, expands and rises (Met Office, 2019). As the air continues to rise, it cools and condenses around the condensation nuclei in the atmosphere and in turn lead to the formation of clouds high in the atmosphere. If this process continues rainfall will occur due to instability in rising cloud systems. West Africa mainly experiences this type of rainfall.

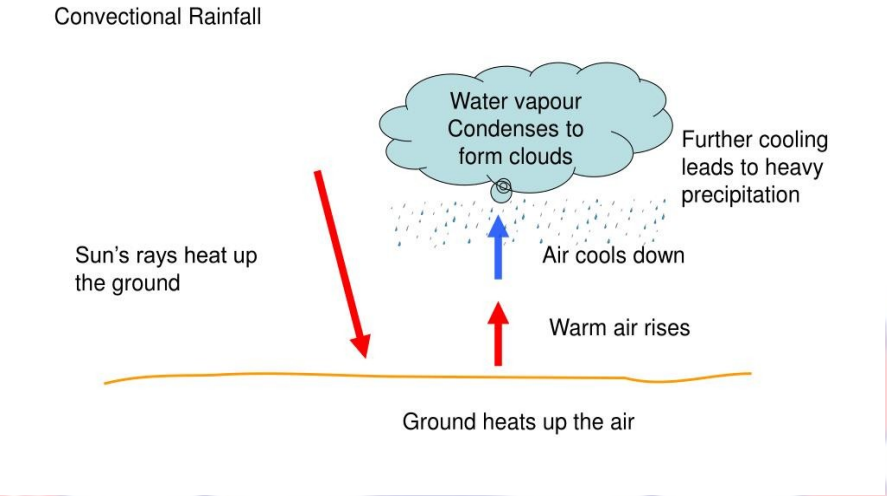

Figure. 5: Diagram showing the formation of convectional rainfall. (Source;https://foxriverkayakingcompany.com/types-of-rainfall/)

Orographic or Relief Rainfall

When wind lifts moist air over a mountain range, the mountain carries the moist air high into the atmosphere (Selase et al., 2015). As the air rises and cools, orographic clouds are formed, serving as a source of precipitation (Figure 6). They ascend further, become unstable water droplets and fall to the

ground as rain, with most of the event happening on the windward side of the mountain range. On the leeward side of the mountain range, rainfall is very low, and the area is mostly referred to as the rain shadow (WMO, 2017). Most heavy precipitation mainly take place windward of a prominent mountain range that is oriented across a prevailing wind from a warm ocean. The mountain here serves as the obstacle that forces the rain bearing winds or water vapour to rise.

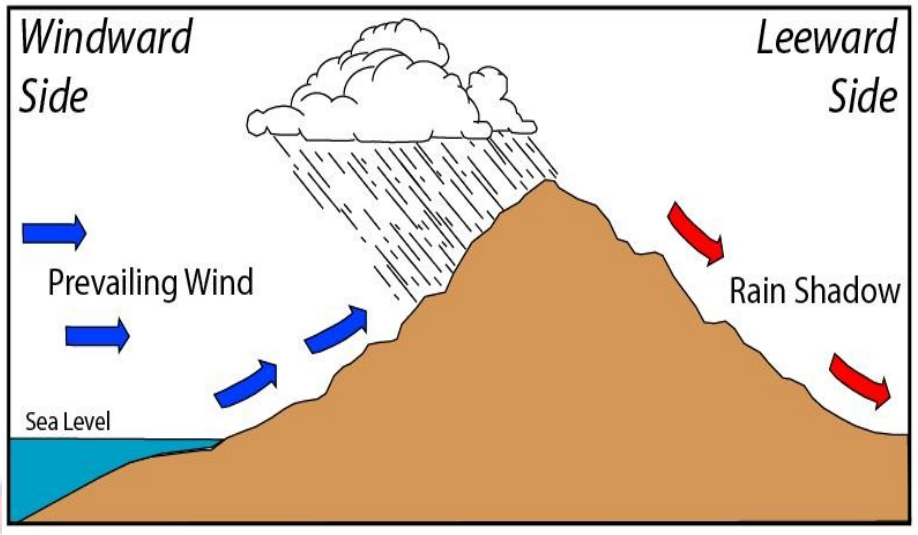

Figure. 6: Diagram showing the formation of orographic or relief rainfall. (Source: https://en.wikipedia.org/wiki/Rain_shadow)

Cyclonic or Frontal Rainfall

Cyclonic or Frontal rainfall take place when the leading edge of a warm, moist air mass meets a cool and dry air mass (cold front). When warm maritime air mass meets a cold air mass, the warm air mass is under-cut by the cold air mass (Figure 7). The warm air mass is forced to rise because it is lighter. The warm water vapor cools down as it rises (Met Office, 2019). The

rising air condenses to form clouds in the atmosphere. As the clouds rise further they become unstable due to more water droplets accumulating. They fall to the ground as cyclonic rainfall (Selase et al., 2015).

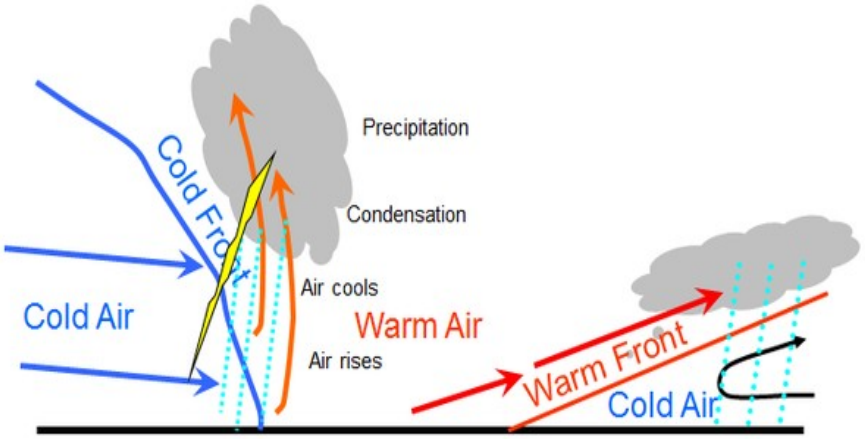

Figure. 7: Diagram showing the formation of cyclonic rainfall. (Source: https://www.quora.com/What-is-cyclonic-rainfall)

Forms of Clouds

Clouds are known to be fundamental in the global climate and all weather processes. Clouds are responsible for heat transport, for all forms of precipitation and they tend to influence solar and infrared radiation in complex ways (Stephens & Kummerow, 2007). Clouds are masses of water drops or ice crystals suspended in the atmosphere, and they form when water condenses in the sky. They appear in many different forms and at about 3 different heights within the troposphere. These different cloud forms can be divided into ten (10). The high level clouds are located at around 5 to 13 kilometres in altitude

and come in three different forms (AMS, 2019). These high clouds are generally thin, fuzzy and white. The high clouds only consist of ice crystals due to its height in the atmosphere. The high clouds are the *Cirrus*, *Cirrocumulus* and *Cirrostratus* clouds. The *Cirrus* clouds (figure 8a) are the most transparent type of clouds.

(a) Cirrus (b) Cirrocumulus (c) Cirrostratus

Figure 8: High-level clouds (Source: metoffice uk, 2019)

The ice crystals in the cloud are well separated, bringing about the transparency and detachment that comes with the cirrus clouds. Cirrus clouds are thin and wispy and often curve with the wind (WMO, 2017). Cirrus clouds appear in separate transparent bands and layers and hardly interfere with the penetration of sunlight. They become mostly yellowish because of the distance from the sunlight when near the horizon. Clouds of this type never produce any precipitation but can serve as a warning for a potential storm.

Cirrocumulus clouds (figure 8b) have a similar appearance to cirrus clouds (WMO, 2017). The major difference from that of cirrus is the way they appear in smaller patches. They're sometimes called 'mackerel skies' because they can sometimes have a grayish color which makes the clouds look a bit like fish scales. These clouds are not often seen; but both cirrus and cirrostratus clouds can transform into them. Cirrocumulus clouds show

features from both cumulus and cirrus clouds and generally come after the cirrus cloud during a warm frontal system. What is worth keeping in mind about cirrocumulus clouds is that they never generate rainfall nor do they interact with other types of clouds to form larger cloud structures but can mean cold weather.

Clouds that look like cirrus but instead fully cover the sky are known as cirrostratus clouds (figure 8c). They are dense like cirrocumulus but instead form one smooth layer. Cirrostratus clouds appear as white sheets covering the whole sky (WMO, 2017; AMS, 2019). They are quite translucent which makes it easy for the sun or the moon to peer through. Their color varies from light gray to white and the fibrous bands can vary widely in thickness. Purely white cirrostratus clouds indicate the presence of a warm frontal system. Some of the best cloud pictures involve cirrostratus clouds because the ice crystals beautifully refract light from the sun or moon producing a dazzling halo effect. Cirrostratus clouds can turn into altostratus clouds if they descend to a lower altitude. The sight of cirrostratus clouds usually mean rainfall is imminent in the next 24 hours.

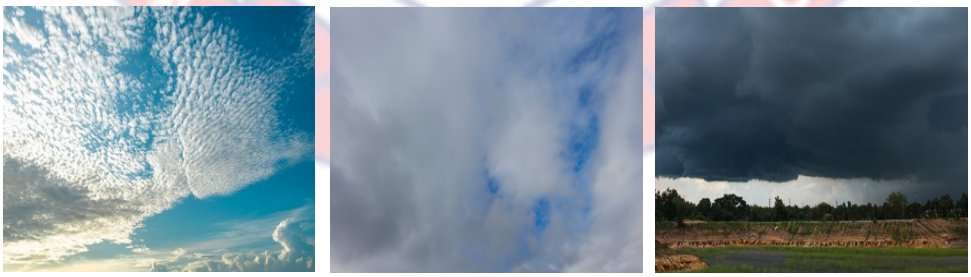

(a) Altocumulus (b) Altostratus (c) Nimbostratus

Figure 9 Mid-level clouds (Source: metoffice uk, 2019)

The mid-level clouds are found at an altitude of about 2 to 7 kilometres and have three different forms (Met Office, 2019). *Altocumulus* clouds (figure 9a) will often appear together with other forms of clouds and with layers at different heights. Altocumulus clouds normally form at a lower altitude and are therefore largely made of water droplets though they may retain ice crystals when forming higher up. They normally form between the lower stratus clouds and the higher cirrus clouds, and mostly precede the altostratus when there is a warm frontal system advancing. When altocumulus appears with another cloud type at the same time, a storm normally follows. Altocumulus clouds are common in most parts of the world. They usually grow by convection, in most cases after damp air rises to mix with descending dry air. Altocumulus clouds may also form in combination with other types of clouds like cumulonimbus. The amount of rainfall from altocumulus is projected from light to moderate.

Altostratus clouds (figure 9b) are a more dense and more grey version of cirrostratus clouds (Met Office, 2019). Altostratus often spread over thousands of square miles and are strongly linked to light rain. The sun can still be seen as a small shiny circle but as the precipitation intensifies, the clouds may transform into nimbostratus clouds (Figure 9c). These types of clouds are often seen in an advancing warm frontal system, preceding nimbostratus clouds.

Nimbostratus clouds occur at the lowest level of the middle level clouds, at a height of 2 kilometres (Met Office, 2019; WMO, 2017). These gloomy clouds are the heavy rain bearers out there forming thick and dark layers of clouds that can completely block out the sun. Nimbostratus clouds

develop as a result of the gradual accumulation of moist area over a large area as warm frontal systems lift the warm and moist area high up in the atmosphere where it condenses. A nimbostratus cloud can form from other types of clouds, like a descending altostratus as well as spreading cumulonimbus clouds. However, during precipitation they tend to lower more and disturb visibility.

Low-level clouds can rise up to 2 kilometres and come in four main forms. These clouds, just like the middle level clouds, consist solely of water droplets. These lower clouds generally look more soft, silky and dense. The *stratocumulus* clouds (figure 10a) come in various forms but can generally be described as big dense separate patches in rolls and layers (Met Office, 2019; WMO, 2017). Rays of sunlight appear in between but will never shine straight through them. Stratocumulus clouds can form light precipitation. The base of this type of cloud is well-defined and flat but the upper part of the cloud is ragged due to convection with the cloud itself. Depending on the thickness of the cloud, a stratocumulus will have light to dark gray hues.

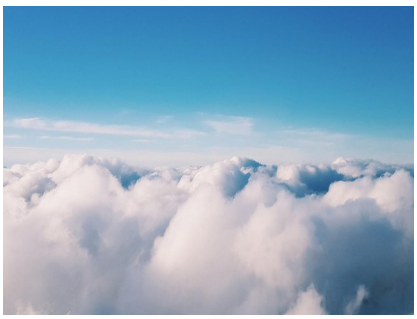

(a) Stratocumulus

(b) Cumulus

(c) Cumulonimbus

(d) Stratus

Figure 10: Low level clouds (Sources: metoffice uk, 2019)

Cumulus clouds (figure 10b) are a bigger, more separate form of the stratocumulus clouds. Also, they appear brighter and more white due to the sunlight that is able to reach different sides of these clouds. They will mostly be found on bright days with blue skies. It is the most recognizable out of all the types of clouds. Cumulus clouds are a sign of fair weather, though they may discharge rains sometimes in the form of a light shower.

Cumulonimbus clouds (figure 10c) are fluffy and white like cumulus but the cloud formations are far larger (Met Office, 2019). It is a vertical developing type of cloud whose base grows from one to up to eight kilometers, hence it is commonly referred to as the tower cloud. For the same reason, cumulonimbus is both a low-level and high-level type of cloud. At the low-altitude base, the cloud is mostly made of water droplets but the high-

altitude summit is dominated by ice crystals. These clouds bring darkness and precipitation which might be very intense, including hail, thunder and heavy winds. The presence of a cumulonimbus means there is a thunderstorm waiting to happen somewhere. Cumulonimbus clouds can be seen most commonly during the afternoons of summer and spring months when the Earth's surface releases heat.

Lastly, *stratus* clouds (figure 10d) are composed of thin layers of clouds covering a large area of the sky (WMO, 2017). When it forms close to the ground it becomes mist or fog. A stratus cloud can easily be distinguished by its long horizontal layers of cloud which have a fog-like appearance. The clouds form from large air masses that rise into the atmosphere and later condenses. However, if enough moisture is retained at the ground level, the cloud can transform into a nimbostratus. Stratus clouds are very common all over the world most especially in the coastal and mountainous regions.

Remote sensing of clouds

Existing methods

Many projects use various methods for the classification of clouds, rainfall estimation and weather forecasts. All these projects use the available satellite data in determining the physical relationships observed between various features and their characteristics. Used methods are generally based on either the emission or the scattering of radiation to space from our atmosphere and the clouds or ground within this atmosphere (Stephens & Kummerow, 2007). The emission-based methods extract information from both infrared

(IR) and microwave (MW) radiation while the scattering-based methods use the scattering of microwave radiation as the source for information.

Emission-based methods

The emission-based methods are limited to information from the upper layers of clouds. The optical thickness of cirrus clouds and their particle size can be determined using the absorption and emission of IR radiation by ice crystals of certain sizes and at certain wavelengths in the atmospheric IR spectrum. This method is known as the split-window method (Stephens & Kummerow, 2007). The difference observed in the brightness temperature of the radiance of a specified channel is related to the difference in the optical depth in specific wavelengths. This then becomes proportional with the size of the ice particle. The emission of MW radiation of clouds and water vapour at certain frequencies is useful for the estimation of the liquid water path of clouds. However, this method has been solely applied over oceans and seas until now. By measuring at frequencies near the water vapour absorption line (22 GHz) and at a higher frequency (e.g. 35 GHz) and by retrieving the MW brightness temperature and optical depth the water vapour column density can be attained. These measurements are not possible yet above the land; the MW emission from the ground is too variable and too big to detect the MW emission from the clouds with the current instruments. Many algorithms have been developed to derive precipitation values from MW emission using atmospheric models and radiative transfer equations (Menzel & Satellite, 2005).

Scattering-based methods

Scattering-based methods mostly use the scattering of sunlight and the scattering of MW radiation (Stephens & Kummerow, 2007). A very advanced way to retrieve optical properties of clouds is based on the reflection of sunlight. A widely developed method is the bi-spectral reflectance method (BSR). This method fundamentally relates the reflection of sunlight to the cloud optical depth and single scatter albedo (the capacity of reflection) by observing layers of clouds consisting of different particle sizes and optical depths. Rain clouds do consist of ice particles. The high frequencies of MW radiation (> 50 GHz) are then used to observe the scattering effects of these ice particles. At different frequencies with known particle sizes there exists a relationship between the brightness temperature caused by the scattering and the ice water path (IWP) of those clouds. From these relations information on the precipitation over land can be derived. However, they vary a lot over different regions. Even higher frequencies are used for snow algorithms based on the same information. All these methods aim to relate radiation to optical and water content properties of clouds and of precipitation. In many of these methods uncertainties arise due to assumptions that are made for micro physical properties of the atmosphere, clouds and of precipitation. According to Stephens and Kummerow, models might be too simple for the complex relations they describe and are therefore neglecting accurate errors and uncertainties (Stephens & Kummerow, 2007).

Cloud top temperature or brightness temperature

Cloud-top temperature or brightness temperature (TB) of convective storm tops depict probably a very key information source used to deduce the type of storm, its structure, its activity and its severity since the beginning of weather satellite information (So & Shin, 2018). The term TB has its origin from the physics of radiative processes. It depicts a virtual temperature at which an object (eg. solid surface, cloud top) would emit the radiance detected by the satellite, on condition that the observed emitting object behaves as an idealized black body (Norman & Becker, 1995). The TB obtained from observed radiance data tend to be lower than their actual (thermodynamic) temperature. This is due to the fact that most of the real opaque surfaces (such as optically thick cloud top layers) emit somewhat less than they would emit if they behaved as a perfect black body. TB is also referred to as the "black body temperature" (usually abbreviated as TBB). The significance of TB or cloud top temperature (CTT) is seen in their relationship to cloud top height (CTH). The higher the cloud, the lower its TB or CTT. It can be said that the coldest infra-red (IR) pixels generally represent the highest tops of clouds, referred to as "overshooting tops" of convective storms. Due to the height of the storm which is closely related to the strength of its updrafts, the highest tops (and lowest BT) are generally found above the most vigorous storms. The range of cloud-top temperature of convective storms rely not only on the storm itself (on its internal properties), but also on the tropopause height and on the geographical region where the storm forms. The higher tropopause heights result in colder storm tops and vice versa. For this reason the storms which form at high latitudes are typically much warmer than storms forming closer to

the equator and the convective storms (thunderstorms) in tropics and sub-tropics are usually very cold, much colder than the ones forming in mid-latitudes (Menzel & Satellite, 2005).

Factors affecting rainfall variability in Southern West Africa

The main factors contributing to rainfall variabilities over West Africa include the West African monsoon system, large scale circulations, regional circulations, sea surface temperatures, land use changes, synoptic scale circulations and mesoscale convective system. The complex interconnections of these factors regulate the rainfall amount realized across different areas of West Africa (Abiodun et al., 2008). Understanding of these systems, therefore, is very key in getting accurate knowledge about the fluctuations in rainfall patterns and also rainfall extremes over the region. West African rainfall is defined by a strong variability in intensity, spatial and temporal distributions. Several factors have been identified to modulate this variability of the rainfall.

West African Monsoon

The West African Monsoon (WAM) is recognised as the prominent atmospheric circulation feature and the major driver of rainfall in West Africa (Janicot et al., 2011). The WAM displays cool southwesterly winds during the summer monsoon and a contrasting warm, and dusty northeasterly Harmattan winds during the winter. Majority of places in West Africa demonstrate a well defined rainy and dry season, emanating from the interconnection between the two air masses: the northeasterly dry and dusty Harmattan wind and the southwesterly moist monsoon winds. The dry and dusty Harmattan wind from

the northeast counteracts the moist monsoon flow from the southwest. The Harmattan forms part of the trade wind system and is mainly characterised by the dry desert air originating from the Saharan region, from November to February. It sweeps over the whole West African subcontinent, reaching the Guinea coast occasionally (Cornforth, 2013). The confluence of both the Harmattan and monsoon flow is known as the intertropical discontinuity (ITD). A strong gradient in dewpoint or precipitable water is used in identifying the ITD. The ITD marks the northern boundary below which rainfall events occur. The ITD is found mainly on land close to the coastline of West African around 8°N. The ITD is sometimes misconstrued to be the ITCZ due to their similarities (Nicholson, 2009). From July to September however, a moist low-level southwesterly monsoon flow is initiated and maintained due to interactions between the differential heating of the ocean and the land surface. A band of rainfall travels from the Coast of West Africa to the Sahel and then retreats. The movement of the zone of maximum moisture convergence and rainfall is the ITCZ. In May, sea surface temperatures (SSTs) start decreasing in the southern parts of the Guinean gulf, initiating the Atlantic cold tongue (ACT) which is a phase of increased sea level pressure spreading to the Guinea coast (Thorncroft et al., 2011). The Saharan heat low (SHL) around this time strengthens and moves northward to about 20°N where it resides for the duration of the summer. The pressure gradient between the ocean and land around mid-June reaches a threshold that generates a sudden displacement of the ITCZ from ~5°N to 10°N, known as the 'monsoon jump', which marks the start of the rainy season in the Sahel. The span of the rainfall season increases equatorward with moist conditions at the Guinea Coast. The WAM features a

distinct seasonality. During boreal winter, the WAM has a different structure from that of boreal summer as depicted in Figure 11 (Parker, 2017a). During the major dry season (boreal winter) of the WAM period, areas of high pressure over the Azores, southern Atlantic and Libya controls the general low-level circulation over West Africa (Figure 11a). The flow of wind towards the low pressure region tends to move southwesterly once it is located in the northern hemisphere. This flow is typically referred to as the “monsoon flow”, which serves as the major source of moisture over West Africa.

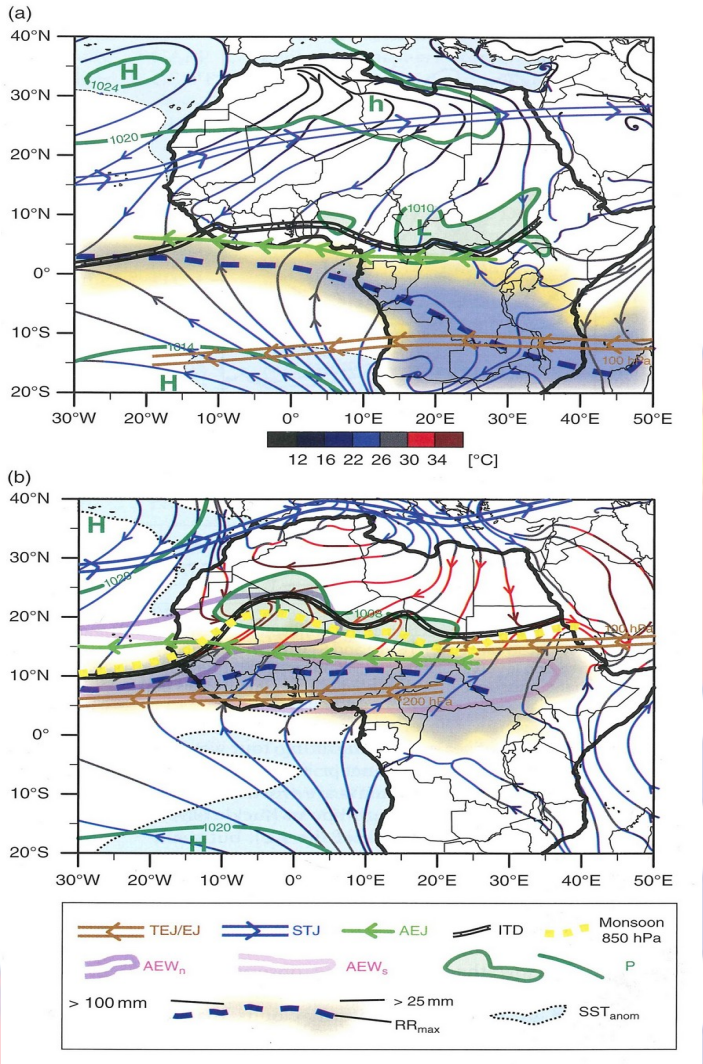

Figure 11: Schematic illustration of atmospheric and oceanic features determining the weather and climate of West Africa in a) January and b) July . (Source : Parker, 2017a).

The ITCZ lies offshore the coast of West Africa (dashed blue lines) during the boreal winter (Parker, 2017a). Interestingly, the immediate coast of SWA is mainly under the activity of the flow of the monsoon all year round due to the ITD's position onshore even during the dry face of the WAM. However, during the boreal summer, an increase in the meridional pressure gradient leads to deeper infiltration of the monsoon flow into the continent,

making the entire SWA moist. The ITD, during this period, navigates to around 20°N.

The TEJ, during boreal summer is found at around 6°N (brown arrowed lines). TEJ emanates from the orientation of temperature gradient between the cool Indian Ocean and the hot Tibetan plateau. A strong anticyclone in the upper level is established due to heating of the Tibetan plateau, with the TEJ shifting to the south of the anticyclone (Grist & Nicholson, 2001). Grist and Nicholson in 2001 related the behaviour of TEJ to changes in the WAM rainfall, that a stronger TEJ leads to wetter WAM seasons in the Sahel on an interannual timescale (Grist & Nicholson, 2001).

The mid-tropospheric AEJ, which is found between 600–700 hPa from April to November (Figure 11b), is mostly located between the ITD and the region of maximum rainfall (green arrow line) and forms due to the warming of the Sahara Desert and the surface high-pressure system with strong interannual variability. This AEJ occurs due to the baroclinicity imposed by the orientation of the temperature gradient between the hot Saharan region and the cooler Atlantic in the north-south direction (Thorncroft & Blackburn, 1999). The AEJ (and the ITCZ) contribute to the unstable nature of the environment during the rainy season by creating a potential vorticity gradient reversal throughout the atmosphere (Thorncroft & Blackburn, 1999). During the boreal summer, the maximum rainfall belt is located between 8-10°N, with the AEJ lying above the belt at around 15°N. In general, the position of the jet is important, as a strong AEJ is connected with low rainfall totals over West Africa. The AEJ also influences the development of the African Easterly Waves (AEWs), which lead to the initiation and maintenance of organized

convection (Fink & Reiner, 2003). The pink-coloured contours (Figure 11b) denote the presence of so-called AEW featuring a southern and a northern branch. AEWs are disturbances that occur over periods of 3 to 5 days and mostly evolve downstream of high terrain somewhere between 15°E and 30°E. The formation and evolution of these waves are influenced by the topography of tropical North Africa, specifically the Ethiopian Highlands and Darfur Mountains (Noble et al., 2014). These easterly waves, which propagate westward, are essential due to its link with convective rainfall and its provision of a favourable environment for the growth of tropical cyclones over the Tropical Atlantic (Mohr & Thorncroft, 2006). The mixture of both the Tropical Easterly Jet (TEJ) and the AEJ create a zonal circulation of moisture and energy within the region as in the case of the global Walker Circulation.

Atmospheric features

During the start of the WAM, the southerly circulation and its associated atmospheric characteristics move towards the poles (Flaounas et al., 2011). Figure 12 outlines the major features influencing the WAM's strength. The modulation of rainfall now occurs due to dynamical features such as the Tropical Easterly Jet (TEJ) and the African Easterly Jet (AEJ). The TEJ is an upper tropospheric circulation (observed within 200 mb and 100 mb) over the Asian monsoon (Flaounas et al., 2011) with a high interannual variability in wind velocities. The TEJ stems out from a thermal wind circulation, and is highly influenced by regions where the mid-tropospheric thickness is huge and the gradient reversed due to the intense heating over the desert. The excessive nature of rainfall over West Africa in a particular year can be associated with

an abnormally fast TEJ and vice versa (Fontaine & Janicot, 1992). El Houssein and Decleir further established that rainy days are well correlated with a significant increase of the speed of the TEJ, with dry days displaying opposing characteristics (El Houssein & Decleir, 1998).

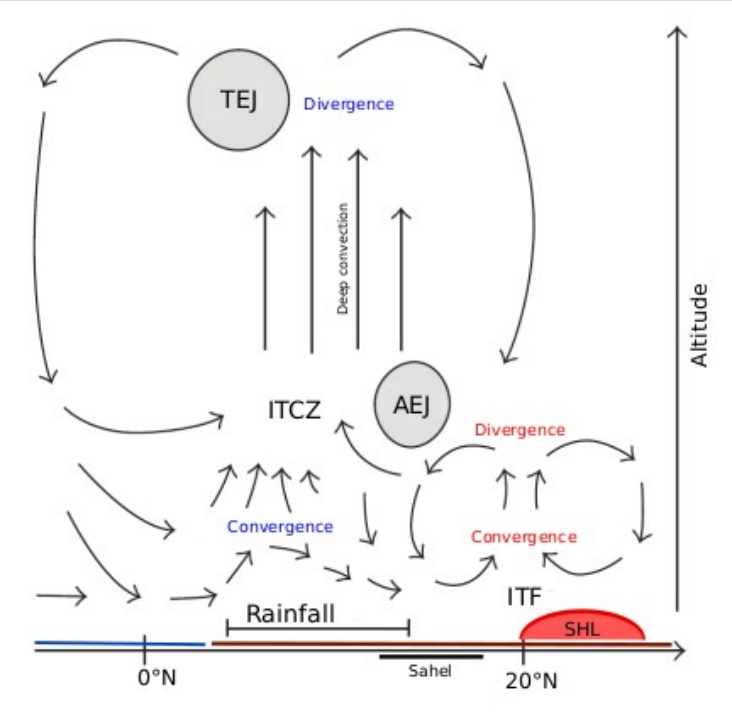

Figure 12: Schematic diagram of the WAM during its peak season (August), showing all governing atmospheric features.

Teleconnections

Sea Surface Temperature Teleconnections

Variations in WAM precipitation are known to be closely linked to the year-to-year variations in sea surface temperature (SST) patterns through teleconnections (Douville et al., 2007; Giannini et al., 2005). The impact of

SSTs on the atmosphere lead to significant changes in seasonal rainfall and other seasonal characteristics. The impact of these SST anomalies over the West African region is not evenly distributed between the Guinea Coast and the Sahel, with the transition zone (Soudan) experiencing a blend of the Guinea Coast and the Sahel responses to SST. SSTs have been associated with rainfall through the strengthening of the Land-Ocean surface pressure gradients that affects surface wind flow, and bring about convergence and cloud formation. The sea-breeze phenomenon can be seen as a common example of such an interaction on the local/mesoscale scale (Hastenrath, 1991). Also, low-level convergence generated from pressure gradients that are related with SST anomalies can feed into the regional and large-scale circulations (Lindzen & Nigam, 1987). It was illustrated that large tropical Atlantic SST anomalies accompanied anomalous tropical Atlantic surface atmospheric circulation patterns that altered the sub-Saharan rainfall (Lamb, 1978). Lamb also observed that warm SSTs anomalies ~300-500km south of 10°N and east of 35°W produce droughts whilst northward anomalies bring about higher rainfall totals in the months of July to September (Lamb, 1978). Fontaine and Janicot in 1996 determined that drought events in West Africa are associated with warm SST over the Indian Ocean and the eastern Pacific, although drought observed over the Sahel region corresponds to warm SST anomalies over the southern Atlantic with cold SST anomalies over the northern Atlantic (Fontaine & Janicot, 1996) . Fontaine and others utilized observational, remotely sensed and reanalysis datasets to determine the impact of Mediterranean SSTs on West African rainfall and confirmed that warm events lead to heavy rain periods, but also warming of the Eastern

Mediterranean affects the low-level wind flow such that it leads to a more northward shift of the WAM, an enhancement of the TEJ and a decrease in the AEJ (Fontaine et al., 2010). The Sahel rainfall was identified as being sensitive to SST anomalies and trends in the remote Pacific and Indian basins, and the local Atlantic basin (Giannini et al., 2003). Giannini further proposed that the warm equatorial Atlantic SST anomalies disrupt the WAM (Giannini et al., 2003). Correlations of WAM rainfall and SSTs over the tropical Pacific, between 1900 to 1970, have been found to be negative but insignificant (Camberlin et al., 2001; Janicot et al., 2001). Warm anomalies of the tropical Atlantic around the same period were observed to cause a significant southward migration of the WAM precipitation, creating wetter conditions over the Guinea Coast and drier conditions in the Sahel (Losada et al., 2010). From the 1970s, the Sahel rainfall showed a weaker correlation with the Atlantic SSTs while its correlation grew stronger with the Pacific SSTs. Over the Guinea Coast, there exists a more straightforward relationship between SSTs and rainfall variations. SST variabilities have little or no impact on rainfall variations outside the months of July to September (JAS). During JAS however, rainfall totals demonstrate a good relationship with SST anomalies over the neighbouring equatorial East Atlantic although there exists a break in the rainfall over the Guinea Coast. Vizy and Cook identified also that the response of Rossby waves to warmer-than-average SSTs produces anomalous rise along the Guinean Coast, therefore increasing rainfall amount (Vizy & Cook, 2001). Conversely, cooler SSTs along the Guinean Coast weaken the monsoon flow, giving rise to below-normal rainfall.

Land Use Changes

In West Africa, deforestation has been correlated with changes observed in the soil moisture, as well as sensible heat and latent heat fluxes. The albedo - precipitation effect is seen by scientists as the process linking deforestation to the rainfall fluctuations experienced in West Africa – the bare soil has a lower albedo than that of vegetation, thus the depletion of vegetation over an area would increase atmospheric subsidence which in effect reduces cloud formation. This then creates a feedback loop as drier situations might inhibit vegetation growth in the northern part and increase rainfall perturbations over the southern part of the region (Taylor et al., 2002; Xue & Shukla, 1993; Zeng et al., 1999). Afforestation is observed in this instance, to influence the rainfall in West Africa through the surface energy balance and the cloud cover interactions (Xue & Shukla, 1996). A relationship was observed between vegetation and regional circulations including the WAM (Eltahir & Gong, 1996). A team led by Taylor in 2002 demonstrated that the changes in land use in the Sahel before 1996 due to agricultural practices led to a conversion of approximately 4 percent of vegetated land to bare soil (Taylor et al., 2002). This change was observed to have caused a reduction in the annual rainfall totals and also inhibited the penetration of the band of maximum rainfall to the north of West Africa (Sahel) as observations indicate. In general, changes in land-use affect rainfall variability over West Africa leading to its contribution to monsoon circulation dynamics (Abiodun et al., 2012; Zaroug et al., 2013).

The role of the surface

The radiation coming from the sun and the energy reflected back into the atmosphere are associated with the land surface, and is expressed by the surface energy balance

$$R_{net} = SW_{in}(1 - \alpha_p) + LW_{in} - \varepsilon\sigma {T_s}^4 = LH + SH + G, \qquad (1)$$

where SW_{in} is the incoming solar radiation (Wm^{-2}), LW_{in} is the longwave radiation (Wm^{-2}) , α_p is the planetary reflectivity or albedo, and ε, σ and T_s are the surface emissivity, the Stefan-Boltzmann constant and the surface temperature (K), respectively (Laing & Evans, 2011). The net radiation is balanced by the fluxes of latent heat (*LH*, Wm^{-2}), sensible heat (*SH*, Wm^{-2}) and the ground heat flux (*G*, Wm^{-2}). The above equation is determined by their surface conditions on all sides. The surface conditions can greatly modulate the energy budget as latent or sensible heat. The effects of strong gradients of surface temperature, soil moisture and vegetation are felt as a result of surface-atmosphere feedback (Koster et al., 2004). Several research findings suggest different governing processes that connect various surface conditions to a considerable scale of spatio-temporal distribution of precipitation (Taylor et al., 2011). To produce positive feedback, favourable surface and atmospheric conditions need to be met. Therefore, the tenacity of various surface conditions is key for the likelihood that the atmosphere becomes sensitive within the time that the surface anomaly prevails (Dirmeyer et al., 2006).

Synoptic-scale Circulations

African easterly waves (AEWs) are the main synoptic systems that take place over the African tropics during the summer. Over West Africa, these wave disturbances are referred to as AEWs. AEWs are wave-like disturbances that propagate westward from northern Africa into the Atlantic Ocean every ~3-5 days during the boreal summer (Burpee, 1974). The AEWs noted for being precursors to the occurrence of MCSs and mainly in the Sahelian region (Gu et al., 2004; Janiga & Thorncroft, 2016) and also tropical cyclones in the tropical Atlantic. They are generated by the decreasing potential vorticity towards the north, that is, baroclinic-barotropic instabilities within the AEJ.

The role of African easterly waves in rainfall

AEWs can be characterized by low-level anomalies to the north of the AEJ and be associated with large MCSs such as squall lines as they propagate westward (Pytharoulis & Thorncroft, 1999). The mechanism by which AEWs form is still not certain although the instabilities realized in the AEJ is clearly a key factor. Near the AEJ (700 hPa), the meridional gradient of potential vorticity (*PV*) changes sign (i.e., the *PV* begins decreasing northward) during the warm season over parts of Africa (Burpee, 1972). The observed sign reversal in the meridional *PV* gradient satisfies criterion for jet instability as described by Charney & Stern (1962). The random perturbations created along the unstable AEJ due to horizontal and vertical wind shear gives rise to the development of the easterly waves. The meridional gradient of potential vorticity *PV*, is defined for a zonal flow as (Burpee, 1972)

$$PV = \left(\frac{-\partial u}{\partial y} + f \right) g \frac{\partial \theta}{\partial p} \quad (2)$$

where p is pressure (Pa), f is the Coriolis parameter, θ is the potential temperature and g is gravitational acceleration (m s^{-2}). Its relationship with the AEJ can be observed in Parker et al., (2005), which demonstrates a meridional cross section of the conditions surrounding the AEJ as well as locations of higher convective activity as shown in figure 13 (Parker et al., 2005). Further studies emphasised on the susceptibility of AEW triggering in this area of the AEJ (Hall et al., 2006). In advanced stages, the AEW can intensify through conversion of energy through barotropic (i.e. horizontal shear instability) as well as baroclinic processes (i.e. thermal advections), which is often further accompanied by energy from convection, as seen by the high fraction of AEW- convection couples (Fink & Reiner, 2003). The barotropic instability is created by the horizontal wind shear produced by deep convection around the AEJ, while the baroclinic instability comes about due to moisture, pressure gradients, temperature and the vertical wind shear. AEWs are formed mainly by convective forcing around the entrance zone of the AEJ (Thorncroft et al., 2008). At this zone a lower tropospheric circulation is created, making the AEW very sensitive to the positioning of the convection activity. The frequency of easterly waves can therefore be explained by fluctuations observed in the convective activity. Also, at the synoptic scale, heating from the ITCZ convection is seen to be more relevant to easterly wave activity than the AEJ.

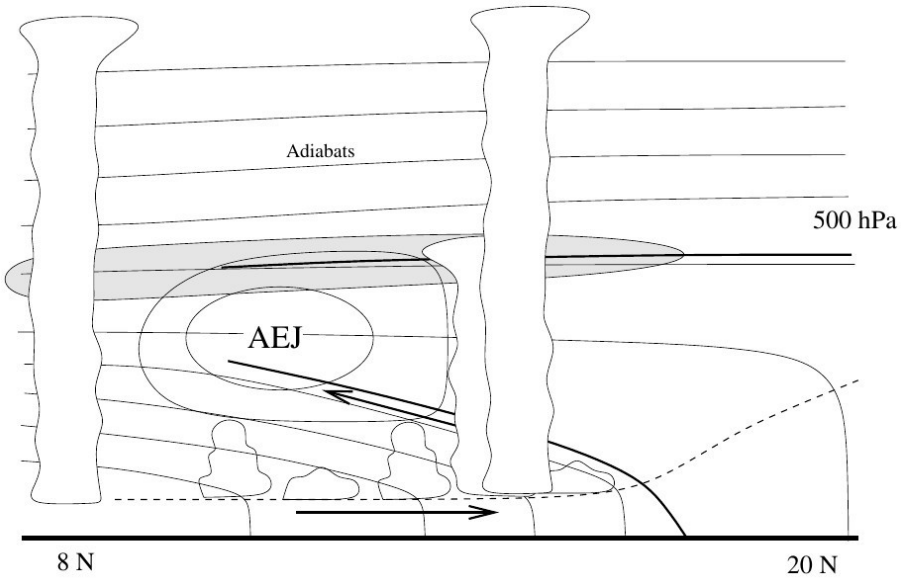

Figure 13: A schematic diagram of the thermodynamic structure on a latitude-height section through the African easterly jet system (Parker et al., 2005b).

In making synoptic weather predictions, observation of upstream convection favours the formation of easterly waves over West Africa due to the significant surge in convective activities over the Darfur Mountains which coincides with the entrance region of the AEJ (Leroux & Hall, 2009). Observations demonstrate that the Darfur Mountains and Ethiopian Highlands aid the initiation of AEWs and long-lived convective systems (Berry & Thorncroft, 2005). Convective activities initiated over high terrain due to dynamical response to vortex stretching, latent heating and increasing potential vorticity in the lee of mountain ranges also help in the formation of AEWs. Furthermore, deep convective clouds in MCSs mostly happen at or ahead of the AEW trough. Deep convection and organised MCSs, which mainly form south of the AEJ with the region of highest equivalent potential temperature, increase the positive PV anomaly equatorward of the AEJ (Thorncroft et al., 2003). MCSs commonly initiate east of the AEW vortices at

850 hPa but at its mature stage, most of the deep convection is located west of the southern vortex and east of the northern vortex. MCSs also grow behind the AEW trough and propagate into the region ahead of the AEW trough. However, convection is occasionally also found on the poleward side of the AEJ. The relationship between AEWs and rainfall can vary significantly due to the present situation. A large fraction of easterly waves carry convection (Schrage et al., 2006) and promote the fast passage of squall lines. Over West Africa, 42% of all squall lines were observed to be AEW-driven (Fink & Reiner, 2003). Overall, most of AEW activities in SWA are experienced in May and June, likewise September and October. Due to the much moist regime over SWA, other rainfall systems, aside organised convection, are known to influence SWA unlike in the Sahel.

Large-scale Circulations

Mesoscale systems over the tropics are modulated by large-scale circulations such as easterly waves, equatorial waves, and the Madden-Jullian Oscillation (MJO). West Africa forms part of the tropical regions with the dominant forcing of squall clusters where convergence is associated mainly with the ITCZ. A relationship between the diurnal behavior of convection and rainfall amounts was confirmed indicating an intraseasonal scale of rainfall variability also exists (Kuettner, 1974; Murakami, 1979). The interseasonal variability of rainfall has been linked to regional drivers, as well as smaller scale weather features such as MCSs. Although AEW troughs provide a favorably large-scale dynamic environment for enhancement of MCS precipitation, only 30- 40% of West African MCSs are associated with AEWs.

The variability of MCSs has more to do with regional thermodynamics, such as Convective Available Potential Energy (CAPE), convection initiated by elevated heating, and dynamics (e.g., low-level shear maxima) rather than enhancements due to the AEW regime (Maranan et al., 2018). Conversely, mesoscale convection affects the large-scale systems through heat, moisture, and momentum transport. Long-lived MCSs are an important link between the convective and large-scale atmospheric circulation because they modify the vertical distribution of heating and moisture. The Hadley circulation is a thermally-driven meridional circuit comprising of warm equatorial air rising and flowing toward the poles in the upper atmosphere, cooling while being transported aloft, and then sinking to the surface at subtropical latitude (Hartmann, 1994; Hastenrath, 1991; Holton, 2004). The Hadley circulation varies both temporally and spatially. These variations are closely coupled to the meridional solar heating and absorption due to seasons, according to the Earth-Sun relationship. During the boreal winter, there is cross-equatorial overturning within the Northern Hemisphere Hadley circulation i.e. the rising branch is in the Southern Hemisphere (Holton, 2004). The rising branch of the Hadley cell is associated with wet climates where precipitation is heavy and exceeds the evapotranspiration for much of the year. The sinking branch is associated with desert climates. The Inter-tropical Convergence Zone (ITCZ) is defined as the zone of the ascending branches of the Northern and Southern hemisphere Hadley circulations and is driven by the large-scale continuity of mass and momentum (Holton, 2004). The vertical thermodynamic structure of the ITCZ indicates that the atmosphere is conditionally stable above the middle troposphere, and as such, the large-scale upward mass in this

environment would lead to cooling aloft (and thus would not satisfy the heat energy budget in the tropics). In order for this energy to be transported aloft into the upper troposphere, the equivalent potential temperature has to be conserved as a parcel is traveling upwards. This is possible through deep cumulus cloud formations such as cumulonimbus clouds. Hence, the ITCZ is actually observed (especially visually on satellite images) as clusters of vigorous cumulonimbus and convection clouds divided by clear patches along the convergence zone of the Hadley cells. In West Africa, the north-south movement of the ITCZ as the seasons change between hemispheres is associated with the onset and ending of the rainy season.

Environmental conditions for rainfall over West Africa

From the standpoint of moisture flux in conjunction with large-scale controls, an extended view of the environmental conditions associated with rainfall over SWA during the poleward migration of the rainband was recently drafted as in figure 13 (Thorncroft et al., 2011). Their concept largely focuses on the development of the sea surface temperature (SST) over the Atlantic and the influence of the continental heat low, which, during the peak monsoon in July and August, reflects the SHL. Four phases were defined, during which the SSTs and the heat low change their characteristics that lead to different patterns in moisture flux convergence (Thorncroft et al., 2011). The “oceanic phase” ranges from November to mid-April (Figure 14a) and is characterised by warm SSTs (> 28^{o}C) and a heat low over land located around 10^{o}N. While the location of the main rainband is associated with the region of highest θ_e as well as strongest moisture flux convergence (MFC) over the ocean around 1^{o}N

(see solid black contours), the heat low over land induces a shallow meridional circulation with further MFC regions at the bottom of the upward branch (i.e. the ITD region) and in the region of the rainband (blue shaded clouds) at mid-levels. As the first rainy season over SWA progresses, the "coastal phase" (mid-April to June) features both the development of the so-called Atlantic cold tongue (ACT) and a northward migration and strengthening of the heat low (Figure 14b). The latter supports the establishment of the ACT, which in turn results in an enhancement of the monsoon flow due to higher meridional pressure gradients. In combination, the rainband shifts polewards to 4^{o}N close to the Guinea coastline, where, due to frictional deceleration of the monsoon flow from ocean to land, MFC increases. As mentioned before, this stage represents the wettest period over SWA (monsoon pre-onset). It is believed by Thorncroft et al., (2011) that this pronounced MFC at the coast may be an important factor for the slow poleward migration of the rainband (Thorncroft et al., 2011). At the same time, the more pronounced northern position of the heat low, now developing into the SHL, accordingly shifts the MFC patterns of the oceanic phase farther inland, improving the conditions for rainfall there.

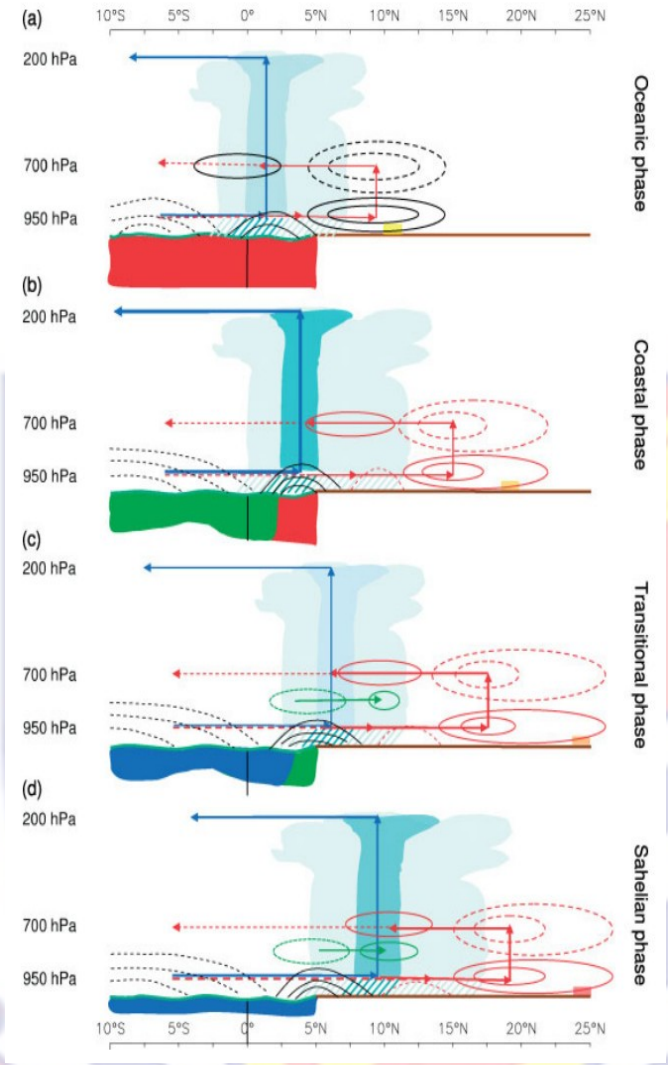

Figure 14: Schematic showing the four key phases of the annual cycle of the West African Monsoon. Thorncroft et al., (2011).

Figure 14 indicates the following features for each phase: the location of the main rain band (indicated by clouds and rainfall with peak values highlighted by darker shaded clouds and rainfall), the location of the Saharan heat-low (indicated by yellow, orange and red shading at the surface poleward of the rain band, with increased redness indicating increased intensity), the atlantic ocean temperature and associated mixed-layer depth (with decreased temperatures indicated by the red-to-green-to-blue transition), the moisture flux convergence maxima and minima (solid contours indicate moisture flux

convergence and dashed contours indicate moisture flux divergence), and the deep and shallow meridional circulations (blue and red lines with arrows). The moisture flux convergence quadrupole structure is highlighted by red contours and the dipole at 850 hPa structure is highlighted by green contours (Figure 14).

However, the midlevel MFC region at 700 hPa (solid red circle) has moved to the poleward side of the rainband, which is suggested to be important for the monsoon onset by deepening of the moist layer (Figure 14 c). The short "transitional phase" in the first half of July features a temporary weak rainfall period and marks the beginning of the monsoon onset (Figure 14 c). The SSTs at the coast decrease due to upwelling of cold water, potentially due to enhanced ocean surface stress by the monsoon flow (Vollmert et al., 2003). While the shallow meridional circulation associated with the SHL retains the MFC structure at a progressively more northern position, a secondary MFC region at 850 hPa (green solid circle) was observed Thorncroft et al. (2011) at around 10^{o}N, which ultimately becomes the new latitudinal position of the rainband and the final setting during the "Sahelian phase" (mid-July to September, Figure 14 d) (Thorncroft et al., 2011).

Extreme Rainfall Events

Extreme events are weather hazards or natural disasters that threaten humans' lives, properties and the environment. Different ways have been used in defining extreme events (e.g. extreme rainfall events). The Third Assessment Report (AR3) of the Intergovernmental Panel on Climate Change (Houghton et al., 2001) defines an extreme weather event as:

"an event that is rare within its statistical reference distribution at a particular place. Definitions of rare vary, but an extreme weather event would normally be as rare as or rarer than the 10th or 90th percentile. By definition, the characteristics of what is called extreme weather may vary from place to place."

However, in the literature (Frich et al., 2002; Groisman et al., 2001), an extreme rainfall event is often defined in three ways. Firstly, when an event exceeds a predefined threshold value, it is called an extreme event. Secondly, the return interval (period of recurrence) of an event of a specific magnitude is used to describe an extreme event. Lastly, an extreme event is defined as an event that is above a set percentile threshold of a given variable distribution. In the present study, an event is defined as an extreme rainfall event if the rainfall amount is equal to or exceeds the 95th percentile threshold of the daily rainfall distributions.

Impacts of Extreme Rainfall Events in West Africa

Extreme rainfall events are among the most destructive natural disasters that continue to threaten socio-economic activities in West Africa (Hountondji et al., 2011). Occurrence of extreme rainfall events often cause flooding and erosion, resulting in loss of lives, destruction of property, and displacement of communities (Paeth et al., 2011). For instance, between 1970 and 2015, extreme rainfall events killed 980 people and injured about 54 individuals across the region (Paeth et al., 2011). In 2007 alone, more than 869 human deaths, with over 2 million people displaced from their homes in West Africa due to floods induced by extreme rainfall, occurred (Tschakert et al.,

2010). Furthermore, for the period 1970 - 2015, about 5 million people were displaced and rendered homeless across the region; 47 communities and 680,000 persons were affected as a result of this destructive weather hazard (Tschakert et al., 2010). In the region, three countries were mostly affected, namely: Ghana (56 killed and over 330,000 affected), Burkina Faso (46 killed, 28,000 displaced and 93,000 affected,), and Togo (23 killed, 13,700 displaced and over 125,000 affected) respectively (Tschakert et al., 2010).

Furthermore, extreme rainfall events are often responsible for soil erosion and crop damage thus affecting agricultural production; they cause infrastructural damage and increase the risk of infection and outbreak of water-borne diseases (Hountondji et al., 2011; Paeth et al., 2011). It was reported that extreme rainfall events damaged infrastructure worth about US$270 million in West Africa in the period 1970-2013, and also destroyed US$2 million or 7,000 hectares worth of rice fields in Guinea, thus emphasizing the disastrous nature of such events in West Africa. Therefore, a major source of concern to West African residents is the damaging impacts of floods from extreme rainfall. Hence, there is a need for a skillful prediction or projection of the future characteristics of extreme rainfall events.

Mesoscale Convective Systems (MCSs)

MCSs are relatively large systems that are prolific precipitation producers and can lead to major flash flooding events (Doswell III et al., 1996; Maddox, 1980; Market et al., 2003; Schumacher & Johnson, 2005). An MCS is an organised complex of thunderstorms that produce a continuous area of convective instability measuring 100 km or more in at least one direction. An MCS system grows and exhibits deep, moist convective overturning from convective towers to convective-stratiform structures associated with vertical circulation. Over the dry Sahelian region of West Africa, MCSs represent the most important source of rainfall during the peak monsoon season in July and August (Fink et al., 2006; Mathon & Laurent, 2001; Mathon, et al., 2002). In West Africa, the main direction of MCS propagation is from East to West, with a speed of movement of the order of 10 ms^{-1} (Mathon et al., 2002). In general, MCSs include organized thunderstorms that persist for a few hours, and squall lines that persist longer (Figure 15). These squall lines are fast-moving and self-sustaining MCSs typically featuring a distinct convective line.

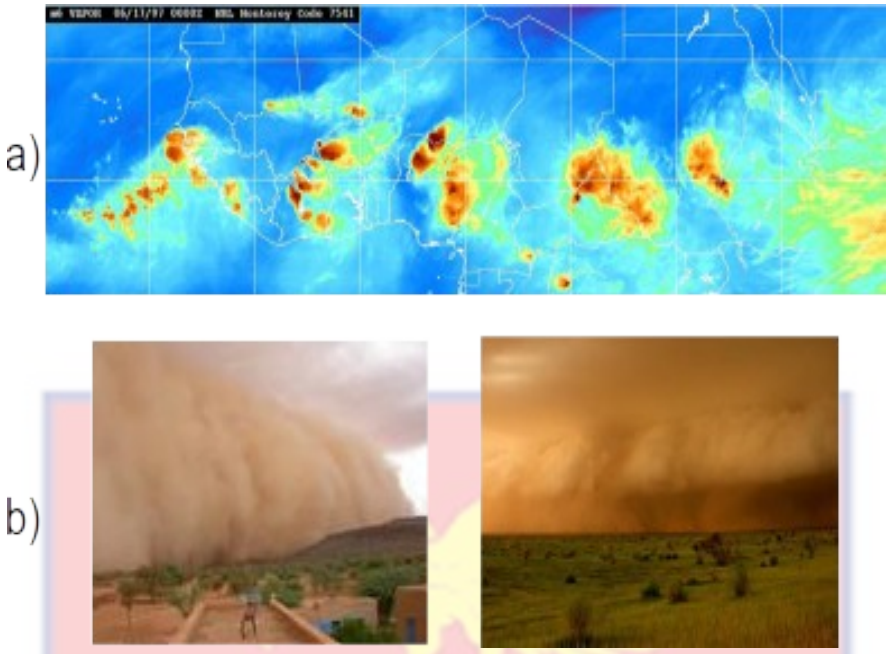

Figure 15. Mesoscale Convective Systems in West Africa. (a) Seen by infrared satellite - weather image (b) Seen from the ground photo (Panthou, 2013)

Zipser in 1982 coined the term Mesoscale Convective System (Zipser, 1982). In 1980, Maddox first explained the Mesoscale Convective Complex (MCC), which is a subset of the MCS (Maddox, 1980). He used infrared satellite imagery with specific criteria (e.g., the cold cloud shield, with an area of 50,000 km^2, will reach below -52^oC) in his identification of these MCCs. The term MCS is now typically used to refer to bow echoes, squall lines, MCCs and any system that meets the criteria MCS but does not fit into any of the other categories (Stensrud & Fritsch,1993). It should be noted however, that one system can fit into multiple sub-categories.

MCSs can be categorized based on a variety of features, aside being a squall line, bow echo, or MCC. Stensrud and Fritsch in 1993 categorized the MCSs in terms of a pre-cold front, quasi-stationary or warm front, and southward burst (Stensrud & Fritsch, 1993). These categories all have a low-

level warm air advection as a common feature. A different perspective to categorizing MCSs was identified by Parker & Johnson (2000) where MCSs were considered to be linear or nonlinear, then further classified as warm sector or non-warm sector (Parker & Johnson, 2000). MCSs are said to be linear on radar reflectivity when the convective line, either a straight or slightly curved line, is observed to be nearly contiguous, share a nearly common leading edge, and move approximately as one. Warm sector MCSs were defined as occurring in the warm sector where warm, moist, unstable air is constrained by synoptic fronts (e.g., cold front). Non-warm sector MCSs were defined as taking place outside the warm sector (Parker & Johnson, 2000). Another way to classify MCSs is by using the location of the stratiform precipitation region in relation to the convective region. These categories are generally termed “leading stratiform”, “parallel stratiform”, and “trailing stratiform”, where the stratiform region is the area where the secondary precipitation maximum is stationed within an MCS (Houze, 1989). “Trailing stratiform” implies that the stratiform region of the MCS is trailing behind the main convective line. With “leading stratiform,” the stratiform precipitation is ahead of the convective line and the convective line tends to be weaker than what is seen with the “trailing stratiform” cases. With “parallel stratiform,” the stratiform region is on at least one end of the convective line. Sixty percent of MCSs can be categorized as “trailing stratiform,” while “leading stratiform” and “parallel stratiform” each account for 20% of MCSs (Jirak et al, 2003; Parker & Johnson, 2000; Peters & Schumacher, 2014).

The structure of a squall line

A general conceptual model of a mature squall line is illustrated in figure 16 (Houze Jr et al. 1989). This model depicts the leading-convective and trailing-stratiform type of squall lines, with the shear vector directed orthogonally towards the idealised convective line. The trailing-stratiform type is the one discussed here. It can be roughly divided into three parts (Lafore et al., 2017): (1) the leading convective line, represented as dark-shaded areas denoting high values of radar rainfall reflectivity, (2) the trailing and widespread stratiform region featuring a slanted ascending front-to-rear flow, and (3) the region beneath the stratiform region having a descending rear inflow (Smull & Houze Jr, 1987). The translation of a squall line can be understood by the superposition of the movement of the cloud cluster being driven by the ambient mean wind field as well as the successive generation of new convective cells in the convective region. The arrows presented in Figure 16 denote the motion relative to the squall line with the downshear side to the right.

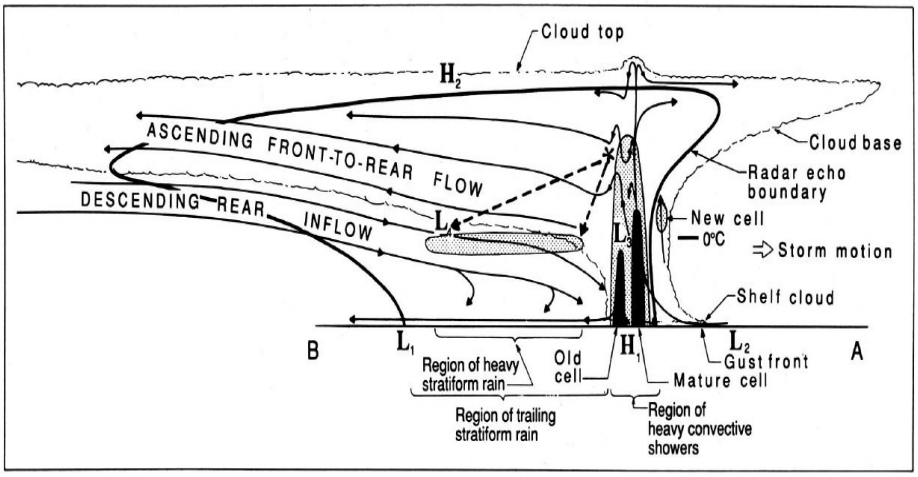

Figure 16: Conceptual model of a squall line with a trailing stratiform area oriented perpendicular to the convective line (i.e. parallel to its motion). More details in the text (Houze et al., 1989).

Squall lines, generally, are penetrated by air masses from front to rear. When an air parcel is lifted by the leading edge of a cold pool to its level of free convection (LFC), latent heating sets in and manifests as upward motion within the convective line and heavy convective precipitation region. The mid-level low-pressure perturbation ("L_3") is as a result of positive buoyancy within the updraught. Due to the motion of the storm, air parcels leave the convective updraught and release the remaining latent heat in the trailing stratiform region, which is reflected by a slow, slantwise ascent as well as the formation of another midlevel region of low pressure ("L_4"). The region underneath is normally accompanied by weak-to-moderate stratiform rainfall, which can last several hours (Fink et al., 2006). The rear inflow descends parallel to the slanted anvil of the trailing stratiform region and is induced by the aforementioned mesoscale low pressure systems L_3 and L_4. Since both L_3 and L_4 are largely of hydrostatic origin, i.e. a consequence of vertical

buoyancy gradients due to latent heating, the rear inflow increases in magnitude with higher CAPE, which can then become a “rear inflow jet”. The implication of the rear inflow over West Africa is that it is often an accelerated branch of the AEJ, which in turn is partly fed by the return flow of the dry convection region over the Saharan heat low. Thus, the rear inflow becomes very dry and enhances cooling through more efficient evaporation of the stratiform rainfall, which can aid the convective cold pool as well as the maintenance of the squall line.

Environmental setup of MCSs

In general, the environmental setup for convection needs atmospheric instability, wind shear (vertical), and some type of forcing (Weisman & Klemp, 1984). The environmental setup for MCSs can vary extensively with different forcing mechanisms and initial conditions, but there are conditions that exist in many MCS initiations (e.g., atmospheric instability, wind shear, development just upstream of an upper-level ridge, and storm relative helicity having values higher than 60 m^2s^{-2} (Jirak & Cotton, 2007)). MCSs can also be initiated from waves propagating out of an old convection triggering new cells that can eventually become an MCS. These waves can be triggered by the net positive buoyancy given by the latent heat (Houze Jr, 2004), or by weak gravity waves that can propagate upstream from an MCS and form new convection there (Stensrud & Fritsch, 1993). It is believed that the combination of the weak gravity waves, convergence already in place, and the maximum in the low-level jet (LLJ) is the most conducive to the propagation of MCSs. While MCSs can be affected by waves propagating outward from

the old convection, cold pool dynamics (Houze Jr, 2004). New convection can be triggered or suppressed by the cold pool depending on its strength. Other conditions observed in MCS initiation environments include divergence at 300 hPa, stronger winds at multiple levels, and warm air advection at 700 hPa. The maximum of the warm air advection at 700 hPa is typically located in the region of the MCS initiation. MCSs normally initiate in environments with high values of CAPE. The high values of CAPE would generally be necessary to sustain a long-lived convective system (Houze Jr, 2004). Also, low level wind shear, low level warm air advection, and instability are key in the upscale growth of a concentrated group of thunderstorms/ convection into an MCS (Jirak & Cotton, 2007).

Convective Available Potential Energy (CAPE)

CAPE is a measure of the amount of energy available for convection. CAPE is directly related to the maximum potential vertical speed within an updraft; thus, higher values indicate greater potential for severe weather (Wallace & Hobbs, 2006). On a thermodynamic diagram this is called positive area and can be seen as the region between the lifted parcel process curve and the environmental sounding, from the parcel's level of free convection to its level of neutral buoyancy. CAPE may be expressed as follows:

$$CAPE = \int_{P_f}^{P_n} R_d(T_{vp} - T_{ve}) d\ln p \qquad (3)$$

where T_{vp} is the virtual temperature of a lifted air parcel from the level of free convection to the level of neutral buoyancy, T_{ve} is the virtual temperature of the environment, R_d is the specific gas constant for dry air, P_f is the pressure

at the level of free convection, and P_n is the pressure at the level of neutral buoyancy. The value depends on whether the moist-adiabatic process is considered to be reversible or irreversible (conventionally irreversible, or a pseudoadiabatic process in which condensed water immediately falls out of the parcel) and whether the latent heat of freezing is considered (conventionally not). It is assumed that the environment is in hydrostatic balance and that the pressure of the parcel is the same as that of the environment. Virtual temperature is used for the parcel and environment to account for the effect of moisture on air density (Wallace & Hobbs, 2006).

Equivalent Potential Temperature (θ_e)

θ_e is known to be a thermodynamic property that relies mainly on temperature and moisture. The θ_e of an air parcel is the potential temperature of the parcel when all the water vapor has condensed and its saturation mixing ratio, w_s is zero (Wallace & Hobbs, 2006). When the parcel's mixing ratio is brought to zero by condensation, the resultant latent heat warms the parcel. A greater value of low-level θ_e implies a high CAPE, energy released if the environmental lapse rate is greater than the moist adiabatic lapse rate. This makes the parcel buoyant with respect to its environment and allows the parcel to be accelerated upward. The air is then compressed dry adiabatically to the standard pressure of 1000 hPa, at which point it will attain the temperature. Equivalent potential temperature is a useful atmospheric parameter due to its conservative nature with respect to both dry and saturated adiabatic processes. Any parameter which remains constant during certain atmospheric transformations is said to be "conserved". Since θ_e is conserved during both

dry and saturated atmospheric processes, it can be used as a valuable diagnostic tracer (Wallace & Hobbs, 2006). The θ_e of a parcel can be changed by adding or removing moisture, or by diabatic heating or cooling. When height is used in place of pressure as the independent variable, the conserved quantity during adiabatic or pseudoadiabatic ascent or descent with water undergoing transitions between liquid and vapor phases is the moist static energy (MSE).

Wind Shear

Wind shear is often a critical factor controlling thunderstorm formation and destruction. Wind shear occurs when there is a sudden change in wind speed and/or direction resulting from a variety of meteorological conditions (Laing et al., 2008). These include temperature inversions, land and sea breezes, frontal systems, strong surface winds and, significantly, thunderstorms. Severe wind shear is defined as a rapid change in wind causing aircraft airspeed changes of greater than 15 knots, or changes in vertical speeds greater than 500 feet per minute (Fujita, 1985). The wind shear associated with thunderstorms in the horizontal direction is referred to as a microburst (the vertical element is also known as a downburst). A microburst is a localized column of sinking air (downdraft) that spreads radially on the ground (FAA, 1987). A microburst comprises vertical, horizontal components and vortices. The vertical component is a powerful downdraft. The horizontal component is the divergent surface wind. The third element are the vortices around the downburst area. Microbursts are associated with convective weather, cumulus congestus and cumulonimbus clouds, and grow in strength

as storm clouds mature. The downbursts can normally be expected below thunderstorm clouds, but the downburst may be at an angle which adds to the unpredictability of the downburst location. When the downburst hits the earth's surface it radiates, and the strength of the horizontal winds may also be asymmetrical. There could be a greater flow in one direction and a lesser flow in the other direction. Around a divergent area, vortices form that can have an upper limit of nearly 2000 feet above ground level, and they feed air back into the cloud (Fujita, 1985). The thunderstorm related downburst is usually a few hundred feet to a few thousand feet in diameter, about 100 m to 1000 m (Fujita, 1985). Wind shear contributes to thunderstorm development by highly modifying the structure of the simple single cell conceptual model. This is that if a thunderstorm forms in an unstable environment with no wind shear, then a vertically-oriented updraft and downdraft will form. The updraft forms from unstable air close to the surface and the downdraft forms from the entrainment of cold, dry air and falling precipitation. As the thunderstorm matures, the downdraft becomes more dominant, choking the updraft and the supply of warm, moist air from the surface that is essential to sustain the thunderstorm. They are most common in the tropics and are known as single cell thunderstorms, popcorn thunderstorms or airmass thunderstorms, because they typically form within a single airmass.

Chapter Summary

This chapter in summary reviewed existing literature and knowledge in the field of study. It provides a basis for the discussions on the rainfall regime and mesoscale convective systems, and their interactions over the West

African region. It is not intended to present a full account of the field of study, but rather the necessary facts to familiarise the reader with the context in which the investigations were performed.

CHAPTER THREE

MATERIALS AND METHODS

Introduction

This section focuses on describing the area, period and the different dataset sources that were used in the study. The different stages of data processing - from the source to the final set of data used in this study - are described in the following sections. The datasets considered in this study involve variables for daily rainfall, cloud-top temperatures and daily atmospheric circulation variables.

Area and period of study

The study concentrated on the area extending from 10°W to 10°E in longitude and from 4°N to 12°N in latitude (Figure 17). This follows the description of the SWA region by Maranan in 2018 (Maranan et al., 2018). On one hand, the period has to be sufficiently long to robustly estimate local return values; on the other hand, it is required to use enough stations for evaluating the spatial statistical models. The study period was therefore chosen to be the best compromise between having a sufficiently large period length (45 years) and the number of daily rainfall series (97 rain gauges) that have less than two years of missing data over this period.

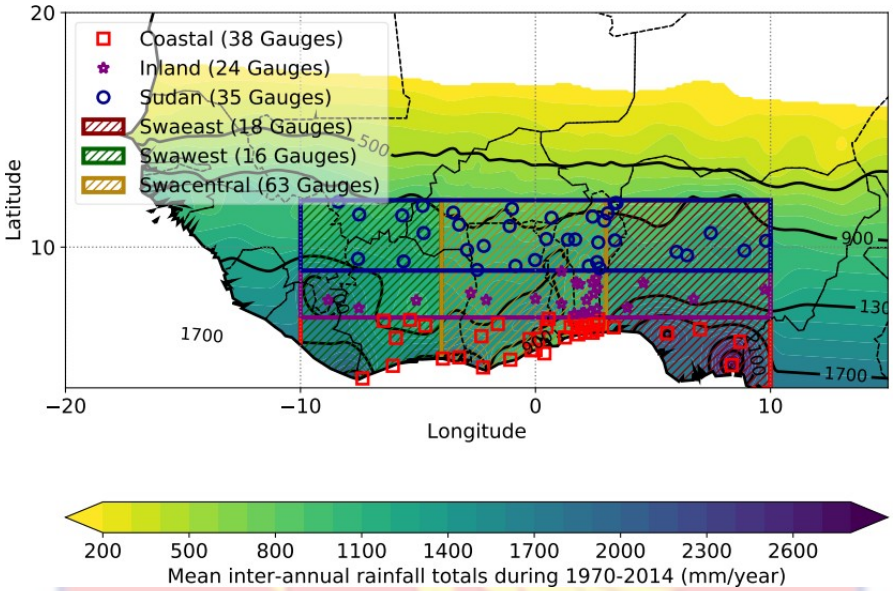

Figure 17: Long term daily rainfall series used to quantify rainfall over subregions at daily scale and over the SWA area; mean annual rainfall totals over the West African region from rain gauge data (shading) are also represented for the period 1970 - 2014.

Rainfall dataset

The primary daily rainfall series used in this work are observations coming from different sources: (i) the Institut de Recherche pour le Développement (IRD) which provided rain gauge data over the West African region until 1985; (ii) collaborative research undertaken by the Laboratoire d'étude des Transfert en Hydrologie et Environnement (LTHE) and national services from various countries allowed an update to the previous data base for the period 1985-2000; (iii) data for the 2000s, were provided by national meteorological services in the framework of the African Monsoon Multidisciplinary Analysis (AMMA) project. The dataset has been scrutinized using specific algorithms to check and visualize the data. A lot of issues with

the dataset (e.g. spurious and erroneous data - monthly data instead of daily, wrong unit, gap-filled data; incorrect date - offset of one day and bad month number) were detected. As a result, changes have been applied to the dataset to better aid the documentation (adding or removing some missing values) and cleaning (e.g. removing erroneous data) of the dataset. Throughout the long life cycle of the dataset, the various kinds of data problems/errors encountered in the past have been studied. Thus, a set of algorithms has been developed to enable the detection of possible problems/errors in the data (e.g. day-by-day spatial coherency check, time-series analysis, distribution checking, etc). In the present study, these tools were used since they permit a continuous, homogeneous, and fast processing of data integration.

For this work, the database over the SWA box defined in this study contains a total of 335 stations over the period 1900-2016. The locations of these stations as well as the year by year number of stations in operation are plotted in figure 18. It should be noted that at this stage, the dataset contains only two types of data: positive float values and missing values (nan). From this large dataset, attention was paid to assess changes in rainfall characteristics over the longest period 1950-2014 in order to analyze the decadal variability of rainfall regime. The study aims at studying rainfall regime changes at the scale of the entire SWA and also within the study region. Indeed, recent studies showed that contrasted rainfall trends can be observed inside climate entities as for instance in the Sahel (Blanchet et al., 2018; Lebel & Ali, 2009; Maranan et al., 2018; Panthou et al., 2018). However, it was not possible to select one single dataset able to cover at the

same time the longest record period (1950-2014) and the study region with enough density to allow a robust analysis in sub-domains.

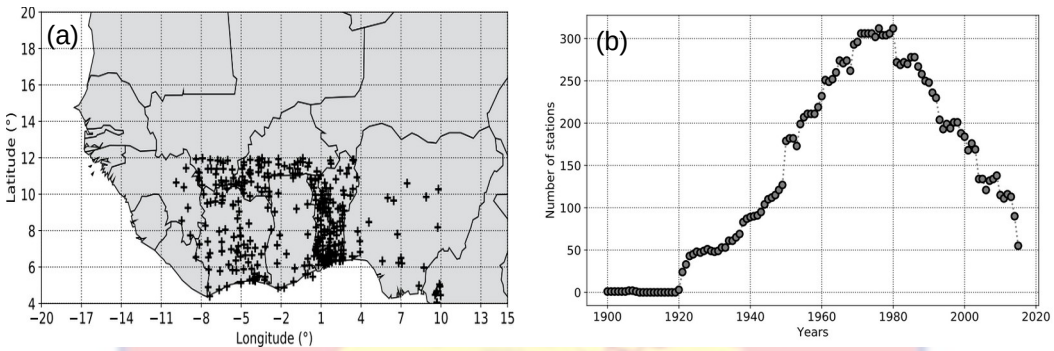

Figure 18: Dataset over the SWA region: a) locations of stations (varying length in the series); b) evolution of the number of stations in the dataset.

Two complementary datasets were thus considered in this study. The first dataset was selected to analyze rainfall changes over the entire study region covering the period from 1950 to 2014. The method for data checking and quality control is fully explained in Panthou et al. (2018), where a criterion is used to classify a year as missing (Panthou et al., 2018). The annual aggregation of a missing year is achieved by attributing a flag value at each of these steps:

- if its annual totals is 2 (resp. 5) times below or higher than the mean annual total of the whole series, then flag equal 1(resp. 2) else flag equals 0;
- same algorithm for the mean number of wet days;
- same algorithm for the mean intensity of wet days;
- an interannual average of monthly totals is computed, and rainy/dry months are classified according to a threshold of 90 mm, then the flag

value is equal to the number of months that belong to the interannual rainy months but that have not recorded rains.

The aggregated flag of a particular year is given by the sum of the 4 flags. If the aggregated flag is ≤ 1, the year is marked as valid. This procedure is somewhat strict but leads to confidence in the quality of information available for a year qualified as valid. The optimization of the rain gauge network spatial coverage over these sub-domains is done at the expense of the time record length. The analysis was focused on the most recent time period by starting from 2014 and going backwards in time in the rainfall series while preserving the maximum spatial coverage. The period 1970-2014 was retained as a good compromise between record length and spatial coverage. The corresponding dataset consists of 97 rain gauges evenly distributed over the study region (Figure 1) with less than 10 % missing years per station over the 45 years. These daily missing values are excluded when computing the annual statistics.

The second dataset was designed to analyse spatial contrasts in rainfall changes by selecting stations covering homogeneously six sub-domains:

- The Coastal region, the southernmost sub-division of SWA from 4°N to 7°N;
- The Inland region, representing the middle sub-division of SWA from 7°N to 9°N
- The Sudan region, the northernmost sub-division of SWA from 9°N to 12°N;
- The West region of SWA (referred to as swaWEST) from 10°W to 3°W;

- The Central region of SWA (referred to as swaCENTRAL) from 3°W to 3°E;
- The East region of SWA (referred to as swaEAST) from 3°E to 10°E

Note that, altogether, for the retained station-years, there are only 5% of missing daily data during the period of study. These daily missing values are excluded when computing annual statistics.

Cloud-top temperature data

The evolution of MCS attributes can be assessed using cloud-top temperatures detected from thermal infrared measurements on various geostationary satellites. These geostationary Meteosat satellites are positioned at around 0°N and 0°E, so therefore have the ability to capture the whole of tropical Africa. This data can be downloaded freely for the period from 1982 to the present from Eumetsat's website (http://www.eumetsat.int). The satellites provided infrared data (10.5 - 12.5 μm) at intervals of 30 minutes with a resolution of about 4.5 km around the equator. The geostationary Meteosat Second Generation (MSG) satellites became operational from 2004, providing higher temporal resolution of 15 minutes at an approximate irregular horizontal spatial resolution of 3 km over the West African region. The Spinning Enhanced Visible and Infrared Imager of the geostationary MSG channel 9 satellite uses thermal infrared brightness temperature data centered at 10.8μm. For addressing the challenges facing climate research, the homogenization of these satellite data have resulted in the production of the global GridSat climate dataset.

This dataset was developed by the International Satellite Cloud Climatology Project (ISCCP) using advanced high resolution radiometer data onboard polar-orbiting satellites. The error associated with the predicted evaluation in this product is observed to be below 0.1°C per decade. The Gridsat data are available every 3 hours. This study considered GridSat data traversing January 1982 to December 2017.

ERA-Interim reanalysis

The ERA-Interim is a global atmospheric reanalysis (Dee et al., 2011) which is provided by the European Centre for Medium-Range Weather Forecasts (ECMWF) and a follow-up of the ERA-40 reanalysis (Uppala et al., 2005). ERA-Interim covers a time period from 1979 to present, with continuous updates in near real time up to the present day. One major objective of the product was to solve various challenges regarding data assimilation (e.g. use of satellite data), which were found during the production of ERA-40. The reanalysis is produced using ECMWF's Integrated Forecast System (IFS) cycle 31r2 released in September 2006. The horizontal resolution of the data set is ~79 km (T_L255 spectral grid) on 60 model levels from the surface up to 0.1 hPa (an altitude of about 65 km). The system applies four-dimensional variational analysis (4D-Var) with a 12 h analysis window. The analysis produced at 00 UTC on a given day involves observations taken between 15 UTC on the previous day and 03 UTC on the present day; the analysis at 12 UTC involves observations between 03 UTC and 15 UTC. The ERA-Interim assimilation and forecast suite are provided for 00:00, 06:00,

12:00 and 18:00 UTC. For this study, we retrieved the ERA-Interim data on a 0.75°×0.75° horizontal grid and on all model levels from ECMWF.

Climate Hazards Group InfraRed Precipitation with Station data (CHIRPS)

CHIRPS are gridded monthly precipitation estimates developed at the University of California at Santa Barbara (UCSB) in collaboration with the U.S. Geological Survey (USGS) Earth Resources Observation and Science (EROS) center. Data from 1981 to 2017 were obtained through the CHIRPS webpage. As described by Funk et al. (2015), the CHIRPS algorithm (i) is built around a 0.05° climatology that incorporates satellite information to represent sparsely gauged locations, (ii) incorporates monthly 1981-present 0.05° infrared cold cloud duration-based precipitation estimates, (iii) blends station data to produce a preliminary information product with a latency of about 2 days after the end of a pentad and a final product with an average latency of about 3 weeks, and (iv) uses a novel blending procedure incorporating the spatial correlation structure of infrared cold cloud duration estimates to assign interpolation weights (Funk et. al., 2015). CHIRPS was validated using various rainfall observation data, and the results indicate good performance for drought monitoring. Annual trends over Africa also fall in general agreement with other observational data (Maidment et al., 2015). This dataset was also found to reproduce adequately several characteristics of precipitation along the coast of the Gulf of Guinea in West Africa (Bichet & Diedhiou, 2018).

Rainfall Analysis

Regional Averaging of daily timescale indices

The following three steps are considered in computing the regional annual means – number of wet days (NWD), mean intensity of wet days (MWD) and annual total (AR):

(i) Computing the mean interannual values at each station k ($\overline{N_k}$, $\overline{M_k}$, and $\overline{AR_k}$ - c.f. equations 1, 5, and 9). At a given station k, all the available years Y_k are used in attaining the above indices (Panthou et al., 2018). In the case of no missing values, Y is a vector such that $|Y|$ = 65 of values ranging from 1950 to 2014 for the entire region datasets (resp. $|Y|$ = 45 values from 1970 to 2014 for the subregional datasets).

(ii) Computing the mean regional interannual values ($\overline{\overline{N_S}}$, $\overline{\overline{M_S}}$ and $\overline{\overline{AR_S}}$) - c.f. equations 2, 6, and 10).

(iii) In attaining NWD, MWD, and AR, the mean regional anomaly for year y is obtained and added to the mean regional interannual values (equations 3, 7, and 11).

In the situation where there exists one or more missing stations for a given year *y*, it is best to filter the latitudinal gradient by working on the anomalies (when working on raw values, a missing station in the south of the study domain would have more weight than if it is located in the north).

The corresponding equations for *N* are:

$$\overline{N_k} = \frac{1}{|Y_k|} \sum_{y}^{Y_k} N_k(y) \qquad \forall k \in K \tag{4}$$

$$\overline{\overline{N_S}} = \overset{K}{\mathbb{E}} \left[\overline{N_k}\right] \tag{5}$$

$$NWD = \overline{\overline{N_S}} + \overset{K}{\mathbb{E}}\left[N_k(y) - \overline{N_k}\right] \qquad \forall y \in Y \qquad (6)$$

where $N_k(y)$ is the number of rainy days at station k for year y, K denotes a vector containing all the stations, and $\overset{K}{\mathbb{E}}$ is an averaging operator that is either an arithmetic mean or a kriging average (Panthou et al., 2018). It should be noted that a day is considered rainy when the daily accumulation exceeds 1 mm.

The corresponding equations for M are:

$$M_k(y) = \frac{1}{N_k(y)} \sum_{d=1}^{N_k(y)} r_k(d, y) \qquad \forall y \in Y_k; \forall k \in K \qquad (7)$$

$$\overline{M_k} = \frac{1}{|Y_k|} \sum_{y}^{Y_k} M_k(y) \qquad \forall k \in K \qquad (8)$$

$$\overline{\overline{M_S}} = \overset{K}{\mathbb{E}}\left[\overline{M_k}\right] \qquad (9)$$

$$MWD = \overline{\overline{M_S}} + \overset{K}{\mathbb{E}}\left[M_k(y) - \overline{M_k}\right] \qquad \forall y \in Y \qquad (10)$$

where $r_k(d, y)$ is the daily rainfall of rainy day d of year y at station k.

A similar set of equations is used for AR:

$$AR_k(y) = \sum_{d=1}^{N_k(y)} r_k(d, y) \qquad \forall y \in Y_k; \forall k \in K \qquad (11)$$

$$\overline{AR_k} = \frac{1}{|Y_k|} \sum_{y}^{Y_k} AR_k(y) \qquad \forall k \in K \qquad (12)$$

$$\overline{\overline{AR_S}} = \overset{K}{\mathbb{E}}\left[\overline{AR_k}\right] \qquad (13)$$

$$AR = \overline{\overline{AR_S}} + \overset{K}{\mathbb{E}}\left[AR_k(y) - \overline{AR_k}\right] \qquad \forall y \in Y \qquad (14)$$

It should be pointed out that the spatial averaging of the computed values for each individual station - denoted by $\overset{K}{\mathbb{E}}$ - was implemented using both the

simple arithmetic mean operator and a kriging operator (ordinary kriging for anomalies - equations 3, 7, and 11; and universal kriging for interannual values in order to take into account the north - south gradient - equations 2, 6, and 10). In analysing the year to year evolution and the long-term trends of the different rainfall regime statistics, the outputs of both methods are equivalent, but differ when estimating the mean regional interannual values ($\overline{\overline{N_S}}$, $\overline{\overline{M_S}}$ and $\overline{\overline{AR_S}}$) - especially when the gauge network is not evenly distributed over a selected region. In such a case, the universal kriging permits to reduce the network distribution effect by estimating an external drift along latitude and longitude, thus allowing for taking into account the north-south gradient of rainfall statistics (Panthou et al., 2018). Results presented are consequently based on a kriging of the point values to estimate the different spatial averages ($\overset{K}{\mathbb{E}}$ in equations 2, 3, 6, 7, 10, and 11).

Assessing uncertainty

The uncertainty of the indexes due to the spatial averaging was predicted by the use of non-parametric bootstrap method (Efron & Tibshirani, 1994) which comprises the following steps:

(i) The vector of station K is resampled using the Monte Carlo resampling method with replacement until its length becomes equivalent to the length of the original vector. The obtained bootstrap vector of stations is named K_{boot} .

(ii) Mean regional interannual values are computed using equations 2, 6 and 10 and applied on the K_{boot} vector of stations.

(iii) Mean regional annual values are then obtained using equations 3, 7 and 11 and applied on the K_{boot} vector of stations.

(iv) The obtained annual indexes for this bootstrap - NWD_{boot}, MWD_{boot} and AR_{boot} are then saved.

The steps used to find the uncertainties are repeated 100 times to generate 100 K_{boot} vectors of stations. Given a particular index, a vector of 100 values is obtained for each individual year. Confidence intervals are thus computed on these 100 values. It should be pointed out that these confidence intervals represent the uncertainty due to the network configuration only.

Statistical testing

The use of statistical tests were employed in this study. In determining possible relationships among precipitation and MCSs, different methods are considered. To decide which way to go, the present data must be studied accurately. In determining various rainfall indexes, two sets of statistical tests were applied firstly to test: i) the significant difference in the central tendency of two samples and ii) if an index presents a significant trend (figure 18). In both tests, parametric and non- parametric tests are found. The parametric ones assume normality of the data in the case of a central tendency comparison.

The non-parametric counterparts - Wilcoxon rank-sum test for central tendency comparison (Mann & Whitney, 1947; Wilcoxon, 1945) - are rank-based and do not need to achieve the normality assumption. In terms of statistics and significance, both tests give the same results.

Other statistical tools

Basic probability tools are employed to get an in-depth understanding of data relationships. If Ω be the sample space of all possible events. The probability P is said to be a set function that assigns a number $P(A)$ to every possible event A in Ω, such that:

- if $A \in \Omega, P(A) \geq 0$
- $P(\Omega) = 1$ (15)
- if for $A_1, A_2, A_3, .. : A_i \cap A_j = \phi$ for $i \neq j$, the finite union then gives $P(A_1 \cup A_2 \cup ... \cup A_i) = P(A_1) + P(A_2) + ... + P(A_i)$ and the infinite union becomes $P(\bigcup_{i=1}^{\infty} A_i) = \sum_{i=1}^{\infty} P(A_i)$.

An event A_1 given that event A_2 has occurred is said to be a *conditional probability* and can be defined as follows:

$$P(A_1 \mid A_2) = \frac{P(A_1 \cap A_2)}{P(A_2)} \tag{16}$$

$$P(A_2) > 0.$$

The probability mass function (*PMF*) of a discrete random variable X is a function $P(X = x) = p(x)$ such that:

- $p(x) > 0 \; if \; X \in \Omega$ (17)
- $\sum p(x) = 1$

If $p(x)$ in equation (17) refers to the *PMF* of the discrete random variable X, then the expected value of X, denoted by $E(X)$, can be written as

$$E(X) = \sum_i x_i p(x_i) \tag{18}$$

provided that $\sum_i \mid x_i \mid p(x_i) < \infty$.

The expected values of X, $E(X)$, can be referred to as the *mean* of X, which is often denoted by μ. If X is a random variable with an expected value $E(X)$, the *variance* of X, is then defined as

$$Var(X) = E\left\{[X - E(X)]^2\right\} \tag{19}$$

provided the expected value exists. The *standard deviation* of X is known to be the square root of the variance. For large datasets, this will be referred to as the *sample mean* $\bar{x}$, *sample variance* σ^2 and *sample standard deviation* σ instead

$$\bar{x} = \frac{x_1 + x_2 + ... + x_n}{n} = \frac{1}{n}\sum_{i=1}^{n} x_i \tag{20}$$

$$\sigma^2 = \frac{(x_1 - \bar{x})^2 + (x_2 - \bar{x})^2 + ... + (x_n - \bar{x})^2}{n-1} = \frac{1}{n-1}\sum_{i=1}^{n}(x_i - \bar{x})^2 \tag{21}$$

$$\sigma = \sqrt{\sigma^2}. \tag{22}$$

Also, if X and Y are two random variables with means μ_X and μ_Y. The *covariance* of X and Y, denoted by $Cov(X, Y)$ or σ_{XY}, can be defined as

$$Cov(X, Y) = \sigma_{XY} = E[(X - \mu_X)(Y - \mu_Y)]. \tag{23}$$

For large data sets the *covariance* will be defined as

$$\sigma_{XY} = \sum_{(x,y)} \sum_{\in \Omega} (x - \mu_X)(y - \mu_Y) f(x, y). \tag{24}$$

Correlation

The correlation coefficient measures basically the strength of a possible statistical relationship, between two variables. There exist different types of correlation.

The Pearson correlation coefficient

This measures the linear correlation. The sample correlation coefficient r_{xy}, given that there are n pairs of data $\{(x_1, y_1), ..., (x_n, y_n)\}$, can be defined as:

$$r_{xy} = \frac{\sum_{i=1}^{n}(x_i - \bar{x})(y_i - \bar{y})}{\sqrt{\sum_{i=1}^{n}(x_i - \bar{x})^2}\sqrt{\sum_{i=1}^{n}(y_i - \bar{y})^2}}. \quad (25)$$

the coefficient takes on a dimensionless value between -1 and 1. Both -1 and 1 describe a strong linear relationship, either negative or positive, depending on how close it is to the extreme ends. If the coefficient takes on 0, it means there is no linear correlation between the two variables.

Spearman's rank correlation coefficient

This type of correlation coefficient is the nonparametric version of the Pearson correlation coefficient and it is based on the ranking of the variables: ordering the variables based on the size of their values. *Spearman's rank correlation coefficient*, for sample size n and converted x_i and y_i to ranks $rg(x_i)$ and $rg(y_i)$, can be defined as:

$$r_s = 1 - \frac{6\sum d_i^2}{n(n^2 - 1)} \quad (26)$$

with $d_i = rg(x_i) - rg(y_i)$, being the difference between the two ranks of each observation. This measures the correlation between the ranks of the variables. The coefficient value shows whether the relationship between the two variables can be described by a monotonic function. From a coefficient of 1 we can derive that $x_i - x_j$ and $y_i - y_j$ always have the same sign, and from a coefficient of -1 always the opposite sign. The benefit of the Spearman's rank

coefficient over the Pearson correlation coefficient is that the Spearman is less sensitive to outliers.

Significance tests

In statistics many different ways are used in testing for significance. Assume a correlation coefficient r has been found between 0 and 1. To test the significance a null hypothesis and an alternative hypothesis are settled respectively:

H_0 r is not significantly different from *0*

H_a r is significantly different from *0*.

In testing for the significance, the *p-value* (a well known statistical value for validating an hypothesis) is often used. In this case, if the null hypothesis is rejected based on the *p-value*, it can then be concluded that *r* is statistically significant. Prior to the testing there should be decided on a significance level α. Generally α takes on values like 0.05. The *p-value* then represents the probability that the extreme event happens while the null hypothesis is true. If the *p-value* is found to be lower than the significance level α, the null-hypothesis will be rejected.

Standardized Precipitation Index (SPI) for annual totals

Using long historic rainfall data, the SPI is computed based on the cumulative probability of a rainfall event taking place at a given station. With a mean of zero and standard deviation of one, the cumulative probability is attained by transforming the probability distribution into a standard normal random variable. The SPI therefore depicts the number of standard deviations

from the mean at which an event takes place. This tool is approved by the World Meteorological Organization to aid in determining the scarcity of a drought at a given time scale of interest for a particular rainfall station with long historic rainfall data. SPI can also be used to determine periods of anomalously wet events. The SPI for annual rainfall totals can be computed as:

$$SPI_{AR}(i) = \frac{r_i - m_{AR}}{std_{AR}} \quad (27)$$

where $SPI_{AR}(i)$ is the standardized annual rainfall index for year *i*, r_i is the annual areal rainfall over the region for year *i* – computed by kriging the *J* = *97* annual point totals – m_{AR} and std_{AR} being the mean and standard deviation, respectively, of the annual areal rainfall series.

Mesoscale Convective System (MCS) Analysis

Lookup tables provided by Eumetsat are used to convert the data from effective radiances to brightness temperatures. The associated discontinuities and biases in pixel size existing due to changes in satellites (from Meteosat First Generation; MFG to Meteosat Second Generation; MSG) are minimized by downgrading to an approximately common resolution of 9 km. On the temporal resolution, only half-hourly MSG data were used. An MCS in this study is defined as a contiguous cold-cloud system larger than 5000 km^2 at different temperature thresholds, defining the average and especially intense (-70^{o}C threshold) MCSs as in Figure 19 (Mathon et al., 2002, Taylor et al., 2018).

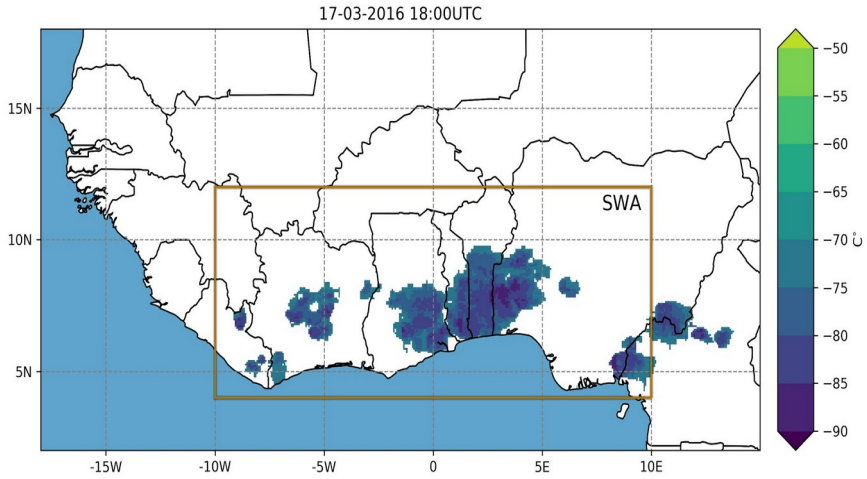

Figure 19. Cloud top temperatures of MCSs with an area threshold larger than 5000 km^2 and temperatures below -50°C (shading). Dark green areas indicate the subset of intense MCSs below -70°C. Box shows the study region of SWA (orange box, 10°W - 10°E, 4°N - 12°N)

Three temperature thresholds are subsequently used: -40°C, -60°C and -70°C. MCS properties are computed for half-hourly images for the period of the rainfall seasons over the SWA region. All MCSs located within the region of interest were counted to be the sum of MCSs divided by the number of available images for the particular rainfall period. When assessing spatial variations in trends, for each image the fractional coverage of pixels within an MCS at 1° spatial resolution is computed. The sensitivity of MCS properties to different temperature thresholds using independent observations were explored to verify if lower temperature thresholds are representative of more intense MCSs.

Trends in MCS frequency at other times of day to ascertain the time of maximum MCS activity were taken into consideration. Focusing on the frequency of MCSs at different temperature thresholds which is a measure that

is rather insensitive to biases and drifts in brightness temperature, the MFG and MSG datasets are used together to produce half-hourly frequency trends of MCS for the two rainy seasons (AMJJ and SON) in SWA. This is to verify the propagation of frequency trends in MCSs relative to observed trends in average rainfall and rainfall extremes. Only MCSs that were identified at 1800 UTC were analysed to prevent multiple counting of one MCS over consecutive hours and also to ensure a similar level of development of MCS samples. At 1800 UTC, majority of MCSs reach their maximum vertical extent and therefore the possibility of observing intense rainfall is maximised. Correlations of the 35-year time series are computed between average MCS frequencies at 1800 UTC and rain gauge data for some rainfall indices to understand how changes in MCS trends influences rainfall intensification. The trends in MCS frequency based on the Eumetsat data at a temperature threshold of -70^{o}C over SWA are used to identify the average annual cycle of positive trends during its latitudinal propagation. Imperatively, the GridSat dataset is used to reproduce observed trends in frequency of MCS as depicted by the Meteosat First/Second Generation dataset. Trends in MCSs produced from the GrisSat data, due to climatic research, are compared with rainfall indices and their correlations calculated.

In computing for average MCS cloud cover, a fractional area containing contiguous pixels below -40^{o}C and larger than 5000 km^{2} at a 0.5^{o} scale, whilst intense MCS cloud cover is computed based on a fragmentary area containing contiguous pixels below -70^{o}C.

The Mann-Kendall test is used in identifying linear trends in cloud top temperatures and atmospheric variables. Correlations are then carried out on

detrended time series data to cut off inter-annual variability. In addition to interannual trends and variability, event-based analyses relating concurrent snapshots of cloud top temperature and rainfall from the CHIRPS gridded dataset with pre-event atmospheric conditions were carried out. This will help understand the condition of the atmosphere prior to an event.

Analysis of trends in atmospheric variables like humidity and wind shear are derived from monthly ERA-Interim data for the same period as that of GRIDSAT (Dee et al., 2011). Associated pre-storm atmospheric conditions are based on hourly ERA-Interim data. If not otherwise stated, all atmospheric data is sampled at 1200 UTC, before the convective peak in the afternoon. The sampled ERA-Interim pixel corresponds to the location of the centered westernmost pixel of the respective MCS, approximately representing the front of the storm.

This dataset is used to analyse atmospheric conditions such as specific humidity, zonal and meridional wind, total column water vapour (tcwv), wind shear, equivalent potential temperature (θ_e) and moist static energy (MSE).

The interest here is in MCS snapshots, which means that the distribution of maximum rainfall here is not representative of the maximum rainfall within an entire MCS lifecycle.

Specific Humidity

In a system of moist air, the mass of water vapor, m_v in a unit mass of air (dry air plus water vapor) is called the specific humidity q, that is

$$q \equiv \frac{m_v}{m_v + m_d} = \frac{w}{1 + w} \tag{28}$$

where w is the mixing ratio, which is the ratio of the mass m_v of water vapor to the mass m_d of dry air.

Equivalent Potential Temperature

The ideal gas law which is $P = \rho RT$ can be written as $P\alpha = RT$, where α is the specific volume $(1/\rho)$. One way that the 1st law of thermodynamics can be expressed is

$$dQ = C_v dT + d(P\alpha) - \alpha dP \tag{29}$$

From the ideal gas law, $d(P\alpha) = RdT$, so

$$dQ = C_v dT + RdT - \alpha dP = C_p dT - \alpha dP \tag{30}$$

Therefore,

$$\frac{dQ}{T} = C_p \frac{dT}{T} - \frac{\alpha}{T} dP = C_p \frac{dT}{T} - R\frac{dP}{P} \tag{31}$$

The potential temperature is then defined such that

$$\ln \theta = \ln T + \frac{R}{C_p}(\ln P_0 - \ln P) \tag{32}$$

The derivative is

$$C_p \frac{d\theta}{\theta} = C_p \frac{dT}{T} - R\frac{dP}{P} \tag{33}$$

Plugging (3) into (5) gives

$$C_p \frac{d\theta}{\theta} = \frac{dQ}{T} \tag{34}$$

The next step is to convert the latent heat associated with condensation into raising the air parcel temperature.

$$dQ_s = -L_v dw_s = -L_v dr_s \tag{35}$$

where $w_s = r_s = r_{vs}/r_d$ is the saturation mixing ratio and r_{vs} and r_d are the densities of the water vapor at saturation and dry air. Notice that this heat

input is the latent heat input per mass of dry air. Combining equation 35 with equation 34 yields

$$C_p \frac{d\theta}{\theta} = \frac{-L_v dw_s}{T}$$

$$\frac{d\theta}{\theta} = \frac{-L_v dw_s}{C_p T} \tag{36}$$

Assuming,

$$\frac{L_v dw_s}{C_p dT} \approx d\left(\frac{L_v w_s}{C_p dT}\right) \tag{37}$$

then,

$$\frac{d\theta}{\theta} = d\ln\theta = \frac{L_v dw_s}{C_p dT} \approx d\left(\frac{L_v w_s}{C_p dT}\right) \tag{38}$$

This last expression can be integrated to give

$$\frac{L_v(T_2)w_s(T_2)}{C_p(T_2)T_2} + \frac{L_v(T_1)w_s(T_1)}{C_p(T_1)T_1} = \ln\theta(T_2) - \ln\theta(T_1) \tag{39}$$

It is known that at the extremely low w_s which occurs in very cold air in the high altitudes where there is virtually no water left to condense out, $\theta_e = \theta$. We use this limit to do the following:

$$\frac{L_v(T_1)w_s(T_1)}{C_p(T_1)T_1} = \ln\theta_e(T_2) - \ln\theta(T_1) \tag{40}$$

where T_2 represents the temperature of the air parcel after it has been lifted into the upper troposphere which is sufficiently cold to set the $w_s(T_2) \sim 0$.

$$\theta_e = \theta\, exp\left(\frac{L_v w_s}{C_p T}\right) \tag{41}$$

Moist Static Energy (MSE)

Here, the changes in MSE are analyzed with a view to understand the precipitation changes over SWA. A thermodynamic variable (analogous to

equivalent potential temperature) calculated by hypothetically lifting air adiabatically to the top of the atmosphere and allowing all water vapor present in the air to condense and release latent heat. The MSE measures the total energy contained in an air parcel, except its kinetic energy.

It sums up dry air enthalpy C_pT, energy associated with the vaporization/condensation of water (L_vq) and potential energy (gz):

$$MSE = C_pT + gz + L_vq \quad (42)$$

where C_p is the heat capacity per unit mass of dry air (1004 $J\ K^{-1}\ kg^{-1}$) at constant pressure, T the temperature (K), L_v the latent heat of vaporisation (2500 $kJ\ kg^{-1}$, irrespective of its negligible temperature dependence) which is nearly the same as w, q is the specific humidity ($g\ kg^{-1}$), g the acceleration of gravity (9.81 $m\ s^{-2}$) and z the altitude (m). The first term on the right side of equation (42) is the enthalpy per unit mass of air. The second term is the potential energy, and the third term is the latent heat content. The first two terms are the dry static energy. When air is lifted dry adiabatically, enthalpy is converted into potential energy and the latent heat content remains unchanged. In saturated adiabatic ascent, energy is exchanged among all three terms on the right side of equation (42): potential energy increases, while the enthalpy and latent heat content both decrease. However, the sum of the three terms remains constant.

Chapter Summary

In this chapter, descriptions of methods employed to achieve the objectives of this study are outlined, with specifics on the region of interest. The definitions of how events were selected for further analysis are clearly

outlined. The different types of datasets used were also described together with their respective used in achieving the objectives of this study.

CHAPTER FOUR

RESULTS AND DISCUSSIONS

Introduction

Before examining the factors leading to the changes in the rainfall regime over SWA, it is important to first confirm if there has indeed been an intensification in the rainfall regime over the region of study. This will help in authenticating the changes identified in the environmental conditions surrounding these events. This chapter therefore focuses on the detection of rainfall intensification over the SWA region and also evaluates the systems that are responsible for these trends and the atmospheric drivers responsible for the changes.

Characteristics of West African Rainfall

Figure (20) represents the spatial distribution of the mean annual rainfall from rain gauges distributed all across the West African region. Spatially, the average inter-annual accumulation of precipitation calculated over the period 1970 - 2014 (Figure 20) indeed shows a latitudinal gradient particularly visible in the Sahelian region. This organization stems from the WAMs zonal structure. It was noticed, however, a certain "dip" of isohyets to the Southeast. The 900 mm isohyet, for example, was located at ≈ 13.5°N on the Senegalese coast and about 11°N. A stretch of relatively low amount of rainfall from the coast of central Ghana running east through Togo and Benin was observed to record a mean annual rainfall of about 900 mm, although regions to the west and east of this stretch records rainfall amounts ranging from 1700 mm to 2100 mm annually.

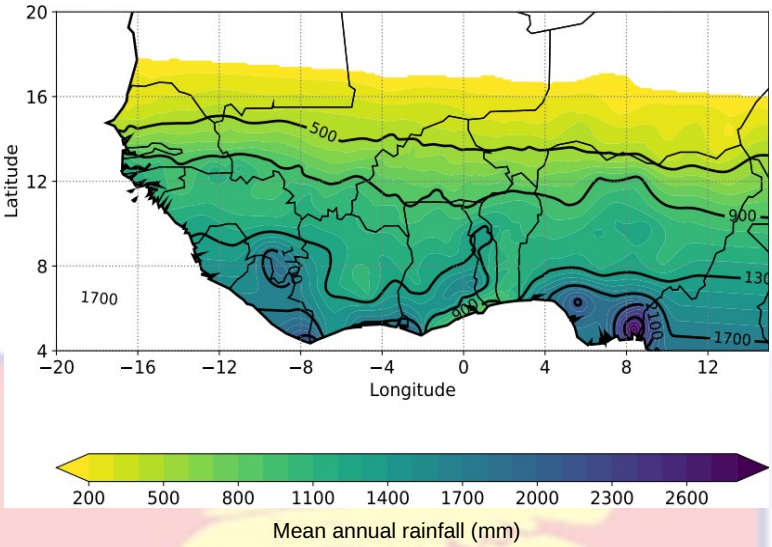

Figure 20: Average annual rainfall calculated over the period 1970 - 2014

Climate evolution at annual timescales

A general analysis was undertaken firstly over the entire Southern West Africa for the 1950-2014 period. Figure 21 shows the SPI of annual rainfall totals (AR) and annual maxima (AM) with their corresponding 11-year moving means. The 1950s and 1960s observed high levels of annual precipitation that exceeded the documented norms (Figure 21a). This wetter regime was followed by an abnormally severe drought during the 1970s and 1980s that led to extensive hunger and population displacements. A gradual recovery of annual rainfall and annual maxima is observed in the beginning of the 90s through to the 2000s, reaching the long-term mean in the late 2000s, after the low values observed during the 70s. Recent years, have observed a more mixed signal with the cumulative mean annual precipitation greater than during the severe drought period, but still less than the pre-drought regime. Annual maxima show (Figure 21b) similar trend as annual rainfall, although

the 11yr moving mean exhibit a little bit steeper upward trend in the extremes in terms of AM as compared to the AR. As expected, the interannual variability in the annual maxima index was larger than that of the annual totals, with more positive values of SPI_{AM} during the dry years as compared to SPI_{AR}. A paucity in both annual rainfall totals and annual maxima was observed over recent years as compared to the wet period between 1950 and 1970, with years after the wet period recording below average values although these events reach the mean in later years of the recent decade.

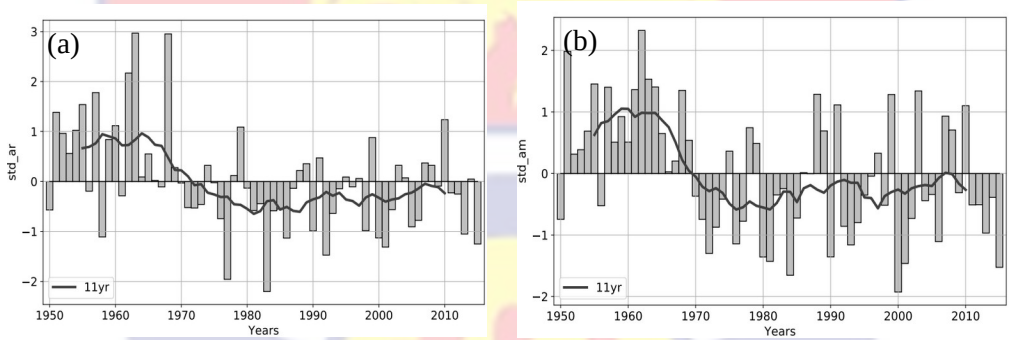

Figure 21: Standardized precipitation indices calculated over SWA for (a) annual rainfall totals; (b) annual maxima, for the period 1950 - 2015

Regional rainfall trends

A general analysis was done to ascertain the recent trends in some particular rainfall indices over the region of study. The SWA regional mean AR was examined and reported with the interannual evolutions of the NWD, the MWD and the 90th percentile (q0.9). The SWA mean AR displays a reduction in rainfall amount between 1960 and 1980 with a slight increase at the end of the 1980s, which was far below what was realized in the 1950s (Figure 22a). A similar pattern to that of AR was depicted in the number of wet days (NWD), with a decrease from the mid-1960s to 1980, which was

followed by a slight upward trend after 1980s (Figure 22b). From 1960 to mid-1970, the MWD depicts a similar pattern over the entire region with a sharp decrease and a clear increasing trend from 1980s through 2014 (Figure 22c). It should be noted that the relative recovery observed over 1980 - 2014 in MWD was larger than the increase in NWD. Events above the 90th percentile (q0.9) have increased from 1980s to 2000s recording extremes close to that observed in the 1950s. It is worth noting that MWD tend to increase with increasing q0.9 (Figure 22d). In all succeeding figures, we keep the 1950 - 2014 curves as a comparison with the period 1970 - 2014.

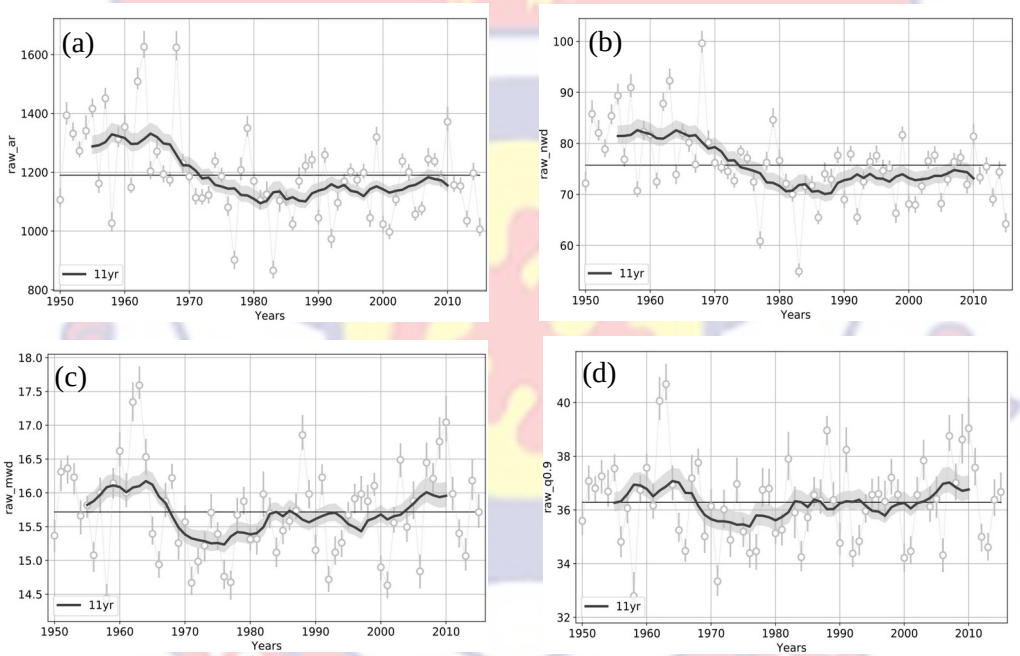

Figure 22: Plots of the 11-year moving averages of (a) AR (mm); (b) NWD (days); (c) MWD (mm/day) and (d) q0.9 (mm/day).

South - North (Coastal – Sudan) disparity

An analysis was made to understand the behaviour of the rainfall regime of daily indices across the south-north sub-divisions for the period

between 1970 and 2014 (Figure 3). Rainfall patterns over all sub-divisions seem to observe similar trends in AR and NWD as portrayed over the entire region. Nevertheless, changes in MWD were observed during the mid-90s, with the coastal and Inland regions realizing an increment in MWD and the Sudan region observing a slightly downward trend. These observed changes in MWD are noticeable over the Coastal region, as seen in the extreme index (q0.9). The Inland and Sudan regions do not observe clear changes in extreme events. Extreme rainfall above the 90th percentile observed a steady increase in the Coastal region from 1990, while the Inland and Sudan regions observed an increase between 1970 and 1990, followed by a stabilization through to current years.

Decadal differences observed at these sub-divisions show that the Coastal region was observed to be wetter with about 5% more rainfall over the recent decade (2005 - 2014) as compared to an earlier decade (1970 - 1979) (Table 1). The Inland region observed 4% more rainfall over 2005 - 2014 as compared to 1970 - 1979 and a 1% decrease in rainfall in the Sudan region over 2005 - 2014 as compared to 1970 - 1979, although all these changes were not significant.

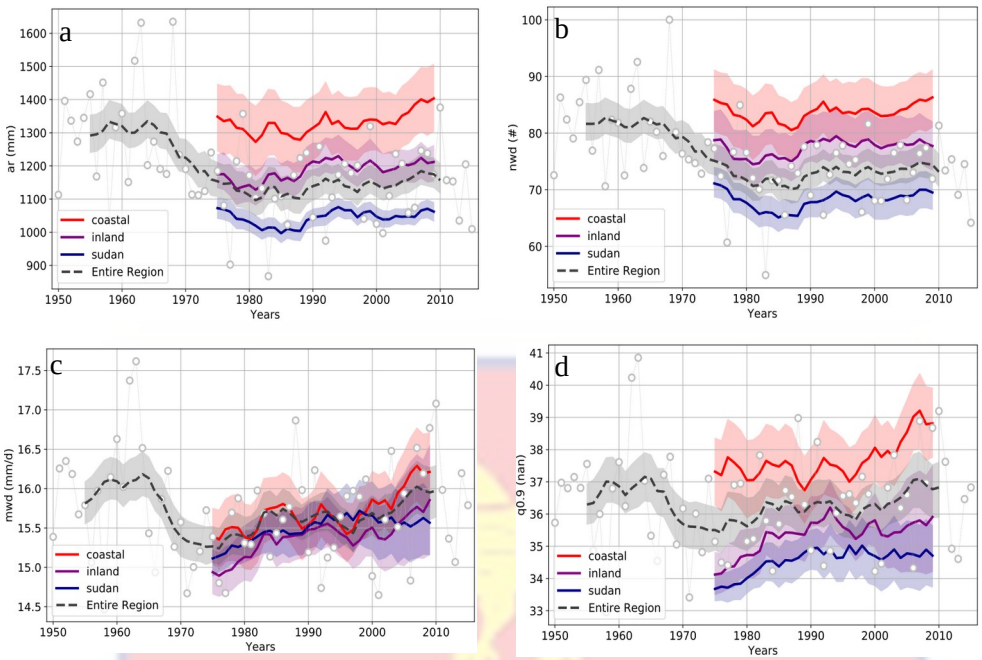

Figure 23: Plots of the 11-year moving averages of (a) AR (mm); (b) NWD (days); (c) MWD (mm/day) and (d) q0.9 (mm/day) for coastal, inland and sudan sub-divisions.

The differences observed in the last two decades also show a non-significant increase of rainfall amount, with wetter conditions 4% more rainfall over 2005 - 2014 as compared to 1995 - 2004 over the Coastal region, a decrease of 1% in mean annual rainfall in the Inland region over 2005 - 2014 as compared to 1995 - 2004 and the Sudan region recording a 1% increase in rainfall amounts over the last two decades. There is therefore a latitudinal decline in annual rainfall as we move away from the coast.

Trends of NWD between 2005 - 2014 and 1970 - 1979 show an insignificant increase of 1% in NWD in Coastal region and deficits of 1% and 3% in the Inland and Sudan regions respectively (Figure 23 and Table 1). The recent two decades experienced overall insignificant trends with an increment in NWD of 2% and 1% in the Coastal and Sudan regions respectively, with the

Inland region still observing a decrease of 2% in NWD. On the other hand, it was observed that the MWD realizes a 6% significant increase over 2005 - 2014 as compared to 1970 - 1979 over the Coastal and Inland regions, and the Sudan region recording a 4% significant increase. Over the last two decades (i.e. 2005 - 2014 and 1995 - 2004), there has been insignificant changes over the region such that the Coastal region had a 3% increment in MWD, the Inland region had an increment of 2% and the Sudan region had no change in MWD. Considering the contribution of extreme rainfall to annual rainfall, a significant increase of 10% was realized in the Sudan region over the last decade as compared to 1970 - 1979, with the Coastal region observing a non-significant 6% increment (Table 1). The Inland region, on the other hand, observed a 3% reduction in this index, although not significant. Changes in the last two decades show no significant trend, although the Inland region observed a decline of about 7% in the contribution of extreme events to annual rainfall while the Coastal and Sudan regions depicted an increase of 2 % and 4% respectively.

Table 1. Relative variation of some key statistics of the rainfall regime: (1) over 2005 - 2014 as compared to 1970 - 1979, and (2) over 2005 - 2014 as compared to 1995 - 2004. These two differences are separated by a semicolon (1; 2). Stars indicate the significance level of the T-Student test: 10% (*), 5% (**), and 1% (***).

sub-division	Annual totals	No. of wet days	Mean intensity of wet days	Extreme / annual totals
Coastal	5% ; 4%	1% ; 2%	6%** ; 3%	6% ; 2%
Inland	4% ; -1%	-1% ; -2%	6%** ; 2%	-3% ; -7%
Sudan	-1% ; 1%	-3% ; 1%	4%** ; 0%	10%** ; 4%

East – West disparity

The AR were first analyzed for the general behaviour of annual rainfall over the swaEAST, swaCENTRAL and swaWEST (Figure 24). Due to similarities in the swaCENTRAL over all mean trend of the whole SWA region, this discussion focused much on the disparity between the swaEAST and the swaWEST. AR depicted a decrease from the 1970s to the start of 1990 in all sub-divisions. All three sub-regions observed an increase after 1990 although swaWEST seems to have observes a decrease from 2000 with a slight increase at the end of that decade (Figure 24a). NWD displayed a similar evolution as in AR with a decrease between 1970 and late 1980s in all sub-regions followed by a slight recovery through to the current decade while swaEAST displayed a decrease in the number of events from late 1990s (Figure 24b). MWD observed an interesting behaviour with swaEAST and

swaWEST displaying almost a 'mirror' pattern after a steady trend between 1970 and 1990. swaEAST depicted an increase surpassing the events in the 1950s while swaWEST displayed a decrease from the 1990s (Figure 24c). An overall similar pattern was observed with the 90th percentile index, showing an increase in extreme rainfall over swaEAST from 1990 onwards. As a result, extreme rainfall were seen to be roughly above levels observed in the 1950s (Figure 24d). The swaWEST region on the other hand, displayed a continuous decrease from 1990 to the late 2000s after which a sharp increase was observed. From these observations, it can be said that swaWEST remains drier (5% less rainfall over 2004 - 2014 than over 1970 - 1979) while the swaEAST recorded a wetter decade (7% more rainfall over 2004 - 2014 than over 1970 - 1979). These differences in behaviour between the swaEAST and swaWEST hold also in the evolution of NWD and MWD. In NWD, the West observed a decrease from 1970 to the end of the 80s, followed by an increase of about 3% above the mean average of the 1970 - 1979 period (Table 2). The Eastern sub-region, on the other hand, recorded a decrease (2% less wet days over 2004 - 2014 than over 1970 - 1979). Consequently, while MWD have significantly increased (10%) over swaEAST in the recent decade compared to 1970s, the swaWEST recorded a significant 5% decrease in mean intensities after a steady trend in the 1970s. Similar patterns persisted in observations made with q0.9, with the east region realizing an increasing trend after the 1980s and the west region recording a significant decrease after the 1980s. It can be noted that the trends observed in mean rainfall intensity correlate well with trends in extreme events over the SWA region.

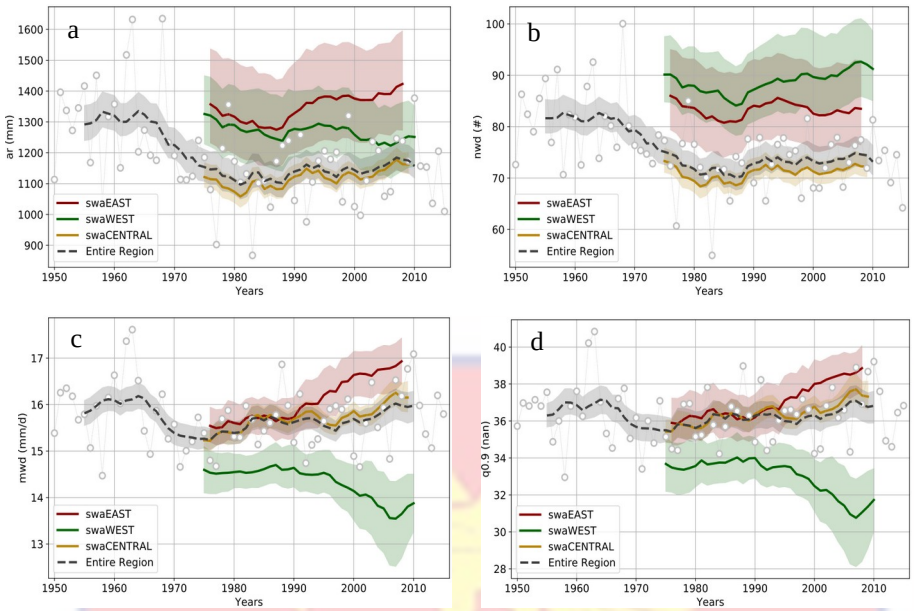

Figure 24 : Plots of the 11-year moving averages of (a) AR (mm); (b) NWD (days); (c) MWD and (d) q0.9 for east, west and central sub-divisions.

The observed disparity was also evident when taking into account the contribution of extreme events to annual rainfall – which increased significantly by 14% in the East and decreased significantly by 17% in the West (Table 2). It should be pointed out that the swaEAST region (which observed similar trends as that of the Central region) displayed a clear contrast in recent trends to that of the swaWEST region. An increment in an index in the East corresponded with a reduction in an index at the West, and vice versa. Comparisons made between the last two decades (i.e. 2005 - 2014 and 1995 - 2004) showed slight changes in patterns, however these changes were not significant. It was realized that the swaEAST region observed an increase across all indices while swaWEST recorded a decrease in all indices with an exception in the number of rainy days which realized a non significant increase.

Table 2. Relative variation of some key statistics of the rainfall regime: (1) over 2005 - 2014 as compared to 1970 - 1979, and (2) over 2005 - 2014 as compared to 1995 - 2004. These two differences are separated by a semicolon (1;2). Stars indicate the significance level of the T-Student test: 10% (*), 5% (**), and 1% (***).

sub-division	Annual totals	No. of wet days	Mean intensity of wet days	Extreme / annual totals
swaEAST	7%* ; 4%	-2% ; 1%	10%*** ; 2%	14%***; 5%
swaWEST	-5% ; -1%	3% ; 3%	-5%**; -2%	-17%***; -8%
swaCENTRAL	4% ; 2%	-2% ; 0%	6%** ; 2%	9% ; 2%

Disparities between SWA Coastal and Inland regions during the two rainy seasons (AMJJ and SON).

Rainfall variability over the Forest Zone (region exhibiting bimodal distribution), with a focus on the two rainfall seasons was carried out. Two general comments can be drawn from Figure 25. First of all, seasonal rainfall indices (AR, NWD, MWD and q0.9) over the AMJJ continued to record higher values in the Coastal region as compared to other sub-seasonal divisions. Secondly, rainfall indices for the Coastal region displayed higher values than for the Inland region, with the exception of the MWD and q0.9 indices for the SON period. AR reached its lowest values in late 1980s over the Coastal region. It increased afterwards to averages observed in the mid-1970s. The Inland region recorded a steady even trend throughout the period in the first rainy season. The SON rainfall season on the other hand, have

observed an increase in annual rainfall over the Inland region from the mid-1980s, with the Coastal region realizing an increasing trend in the 1990s (Figure 25a, b).

For NWD in AMJJ, both regions observed an initial decrease during the 1970s, and remained fairly stable, depicting a general decrease in the frequency of occurrence of wet events over the Forest zone of SWA region during AMJJ. Nevertheless, the SON season recorded an increase in NWD after a downward trend from 1970 to the late 1980s (Figure 25c, d).

It is worth noting the increasing trend of MWD in AMJJ rainfall season over both Coastal and Inland sub-domains from the 1970s to recent decade. In the SON season, the Inland sub-division, MWD observed a gradual increase until the start of the last decade and then, a sharp gain was recorded during the last decade. The Coastal sub-division witnessed an unstable trend with the 1980s recording high intensities compared to the 1970s. The index reached its lowest values in the mid-1990s; it sharply increased afterwards (Figure 25e, f). During the AMJJ season, q0.9 index observed an increment from the late 1980s in the Coastal sub-division with the Inland sub-division realizing a fairly steady trend over the whole period. The pattern realized over the SON season for the q0.9 index depict the trends observed in the MWD index for the same season (Figure 25g, h).

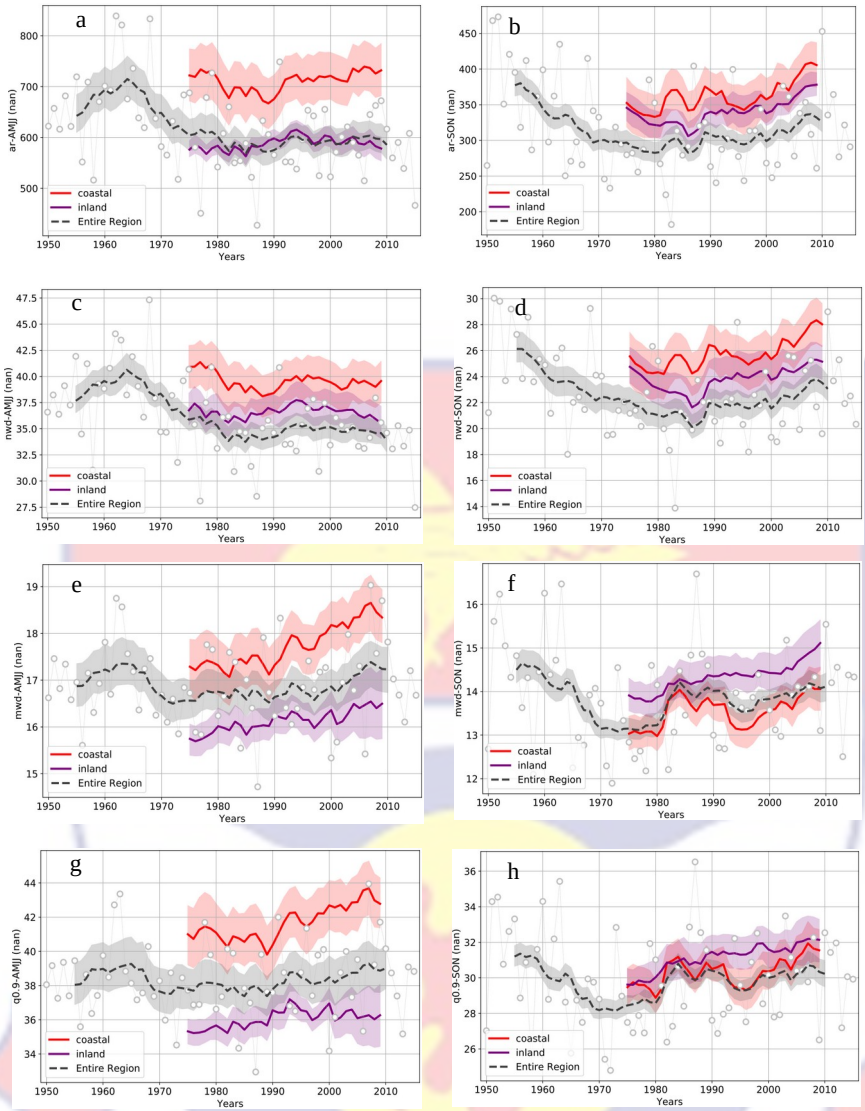

Figure 25: Plots of the 11-year moving averages of (a, b) seasonal rainfall total; (c, d)NWD (days), (e, f) MWD (mm) and (g, h) q0.9 for April-May-June-July (AMJJ) (left panel) and September-October-November (SON) (right panel) rainfall seasons for coastal and inland sub-divisions.

It can be inferred from Figure 25 that changes in seasonal rainfall over SWA was driven by storms becoming more intense before and early in the first rainfall season whiles predominantly becoming more frequent with weaker intensity increases after the 1980s (Klein et al., 2021).

To ascertain stations that are contributing to the rainfall intensification over the SWA region, a spatial representation of station trends for the two rainy seasons were displayed in Figure 26. In the first rainy season (AMJJ), it was observed that annual rainfall amount tend to fluctuate over the region with almost an even number of increasing and decreasing trends (Figure 26a). This pattern of evenly distribution of increasing and decreasing trend was exhibited in the mean intensity and extreme rainfall during the season with the increasing trends being very significant (Figure 26c, g). This confirms earlier findings that mean annual totals are not changing much although extreme rainfall events tend to increase. It can be observed that for number of wet days most station recorded a decreasing trend over SWA (Figure 26e). It can be pointed out also that most stations situated at the western part of SWA recorded a downward trend in all analysed indices as compared to the central and eastern part of SWA.

During the SON season, we realised that the region is dominated with upward station trends in all the indices (Figure 26). This suggests an intensification pattern mainly during the second rainy season of the year with significant increases in mean rainfall intensity and extreme rainfall, as well as mean annual totals in the recent decade.

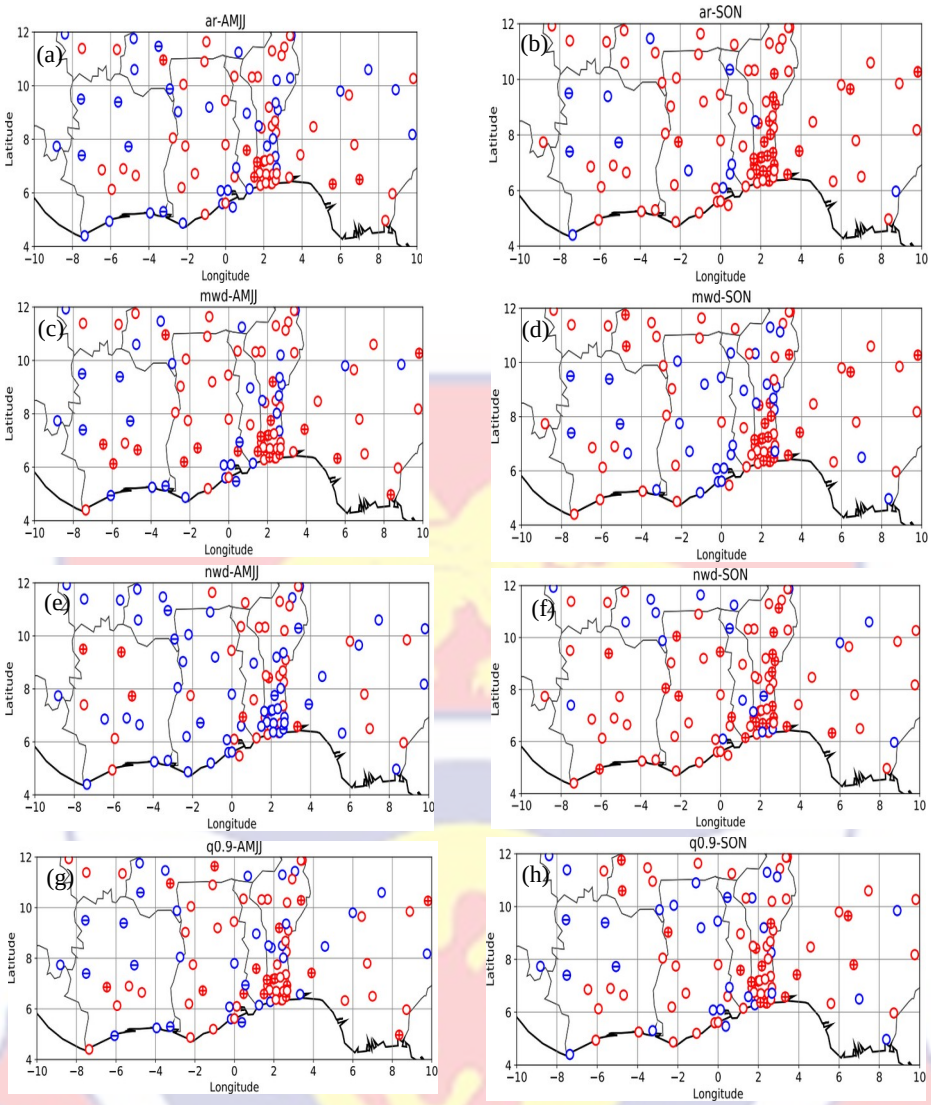

Figure 26: Map of trends of (a, b) seasonal AR; (c, d) MWD (mm); (e, f) NWD (days) and (g, h) q0.9 for AMJJ (left panel) and SON (right panel) rainfall seasons from 1970 - 2014; red (blue) circles indicate an increase (decrease) in trend of extreme rainfall. The plus (minus) sign indicate the significance at 5% level of significance.

One notable behaviour to point out is the cluster of significant increasing trends over Benin. The western part of SWA continued to exhibit stations showing significant downward trends in extreme rainfall events but an increase in number of wet days. The contrasting behaviour in the western and

eastern part of the SWA region raises the question of whether different systems contribute to trends in these two areas in both rainy seasons.

Spatial distribution of MCS trends

Figures 27 and 28 show the trends in MCS frequency at selected times of day using computed average MCS frequencies over all 48 images within the day during the two rainy seasons. Three different temperature thresholds were used: -40°C, -60°C and -70°C, over the SWA domain (10°W to 10°E, 4°N to 10°N; plotted in Figure. 27). MCS properties for every available half-hourly image for the two rainy seasons in SWA were computed. Each MCS centered within the domain was counted as the sum of MCSs divided by the number of images available in each season. In the first rainy season (AMJJ), it was observed that, trends in minimum temperature for each MCS at all observed thresholds of -40°C, -60°C and -70°C propagate westward as time progresses. MCS trends increased during its passage. Systems gained maximum frequency at about 1800 UTC representing the start of the mature phase, after which they saw a decline into the night (Figure. 27). Over the Coastal region, there seemed to be a belt of decreasing trend in average MCS frequency, whereas no clear trend existed for cold and very cold cloud systems. Comparing daily station trends to average MCS frequency over SWA for AMJJ, it was realized that the absolute trends in annual rainfall totals, as depicted in Figure. 26a followed well the behaviour of average MCS frequency in terms of spatial distribution as observed in trends for -40°C MCS frequency.

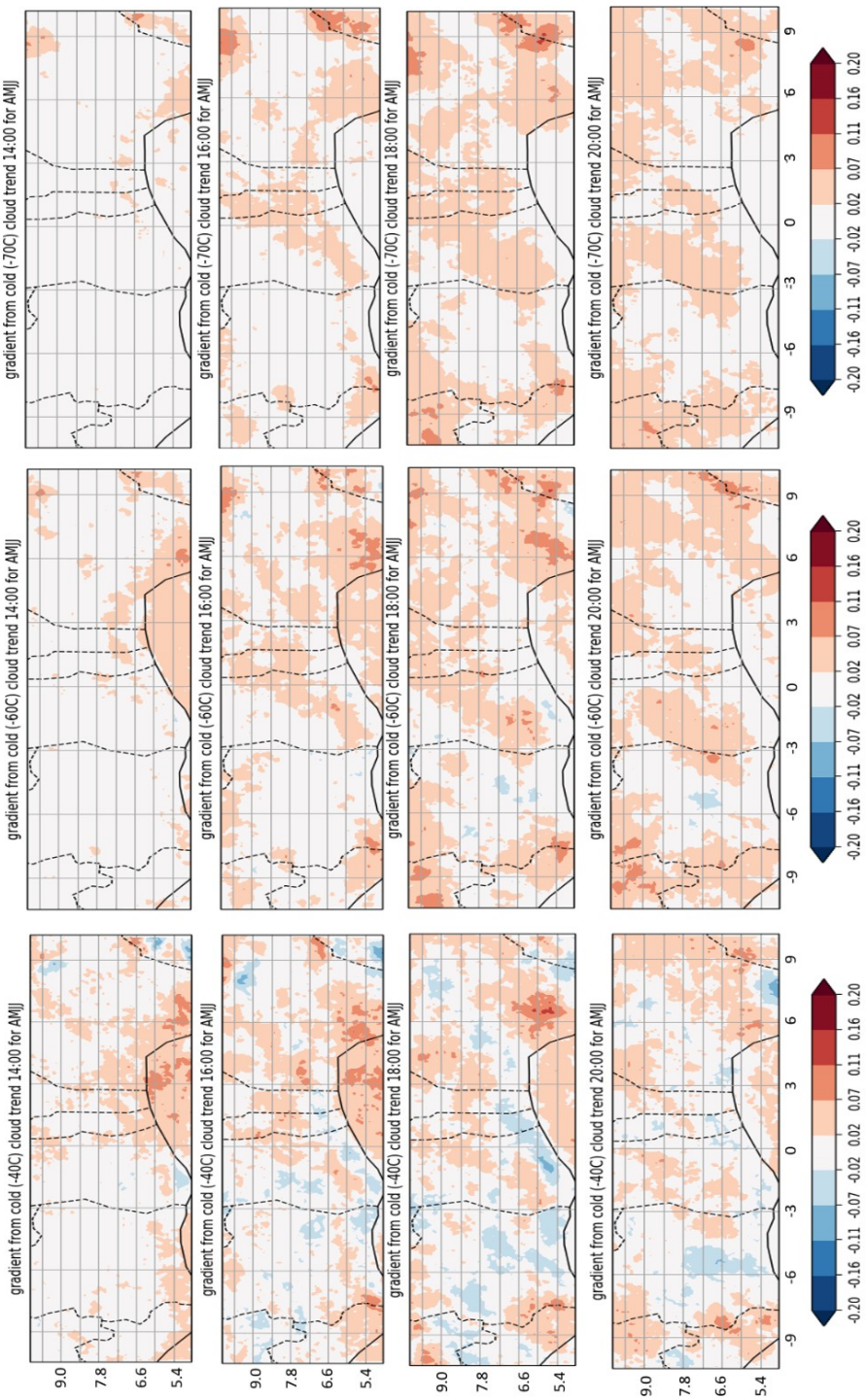

Figure 27: Significant trends ($P < 0.05$) in MCS cloud cover at 1400,1600, 1800 and 2000 UTC using temperature thresholds of -40°C, -60°C and -70°C for AMJJ

During the AMJJ season, it was realised that the northern and south-eastern part of Nigeria observed a significant trend in MCS cloud cover for -70°C and -60°C but not for -40°C. The same happens over some part of Ghana, Ivory Coast and Guinea mainly during the mature stage of average MCS activities. This showed that storms since the 80's have become colder and more intense rather than more frequent over such areas(Taylor et al., 2017). Thereby postulating the idea of the expectancy of extreme convective activities over parts of SWA that observed more intense storms during the AMJJ season. It was also observed that more frequent activities of storms occur over the ocean although not very cold. Another observation made was that the negative/positive trend patterns in -40°C average MCS frequency reflect the negative/positive areas in the annual rainfall totals from the rain gauge analysis.

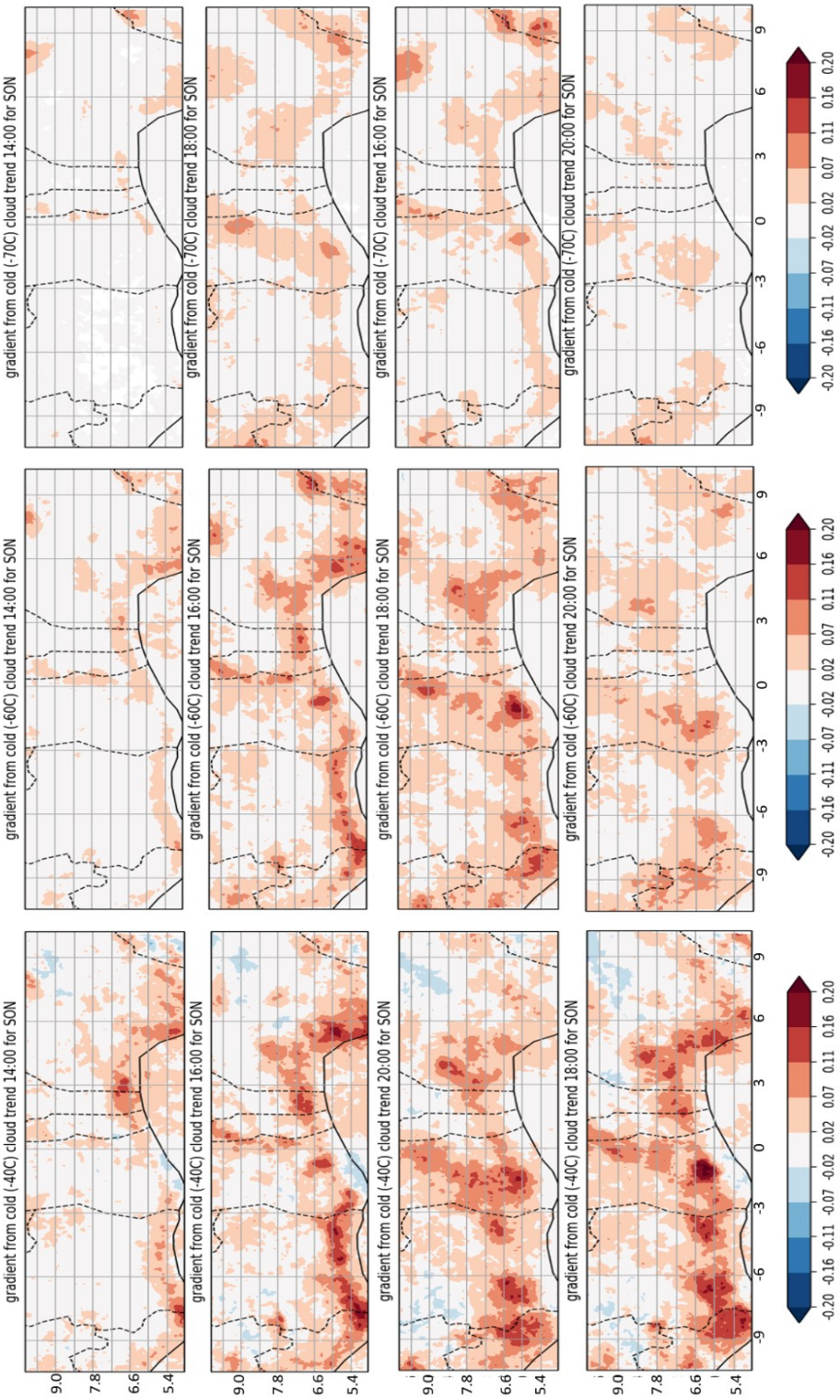

Figure 28: Same as figure 27, but for SON.

During the SON season, trends in MCS at all temperature thresholds still propagated westward with stronger positive trends mainly over the coastal belt which was not the case in the first rainy season (Figure 28). This clearly shows how MCS activities have become very frequent during the SON season although not traveling far west enough as in the AMJJ season. There existed a positive trend that rose along the greenwich meridian over the SWA region in the afternoon when the storms were in their development stage. This trend over the meridian attained its maximum as well as reaching its mature stage, by gaining more intensity, at around 1800UTC. This pattern in trend, during the mature stage of MCS was observed to be well traced out by absolute trends observed in annual rainfall and extreme events over the SWA region during the SON season.

Analysis of the diurnal cycle (Figure. 29) demonstrated that positive trends in MCS frequency at the different temperature thresholds (-40°C, -60°C and -70°C) at all times of day, and were in phase with the general life cycle of an MCS with an initiation in the afternoon, peak frequency during the evening, and a decay in the morning hours. It was realised in figure. 29 however, that trends observed due to the total coverage of very cold systems was dominated by changes in frequency. MCS frequency is observed to attain its peak at around 1800 UTC, with most events happening between the hours of 1500 – 2100 UTC. It can be noted that the likelihood of observing intense rainfall rates will be maximized during the period 1800 – 2100 UTC, which was associated with mature MCSs. This observation was made in both rainy seasons, although daily frequencies in the first rainy season (AMJJ) tend to be high as compared to the second rainy season (SON). The diurnal phase of

these MCS frequency implies that they are controlled by more intense convection during late afternoon and evening, and therefore bringing about long-lived MCS systems overnight.

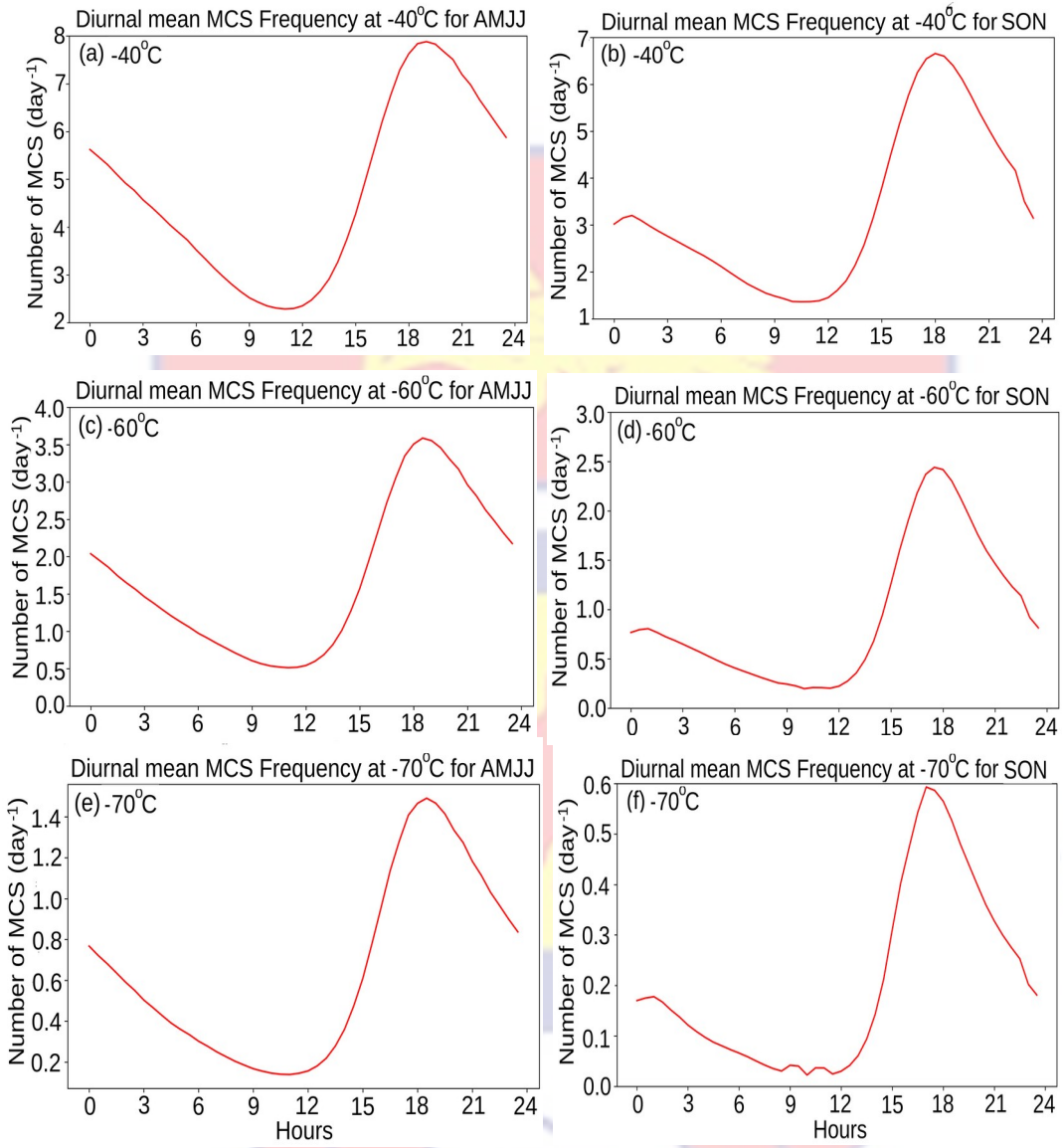

Figure 29: Diurnal mean MCS frequencies (AMJJ; left panels) and (SON; right panels) for temperature thresholds of -40 °C (a, b), -60 °C (c, d) and -70 °C (e, f).

Temporal distribution of MCS trends with Rainfall

In Figure 30, trends in MCS frequency are sampled at 1800 UTC - a time of day when, most MCSs have reached their mature phase (Futyan & Del Genio, 2007). It was also realised that as the temperature threshold reduced, the time series start to resemble strong linear trends in both seasons across all sub-divisions in SWA.

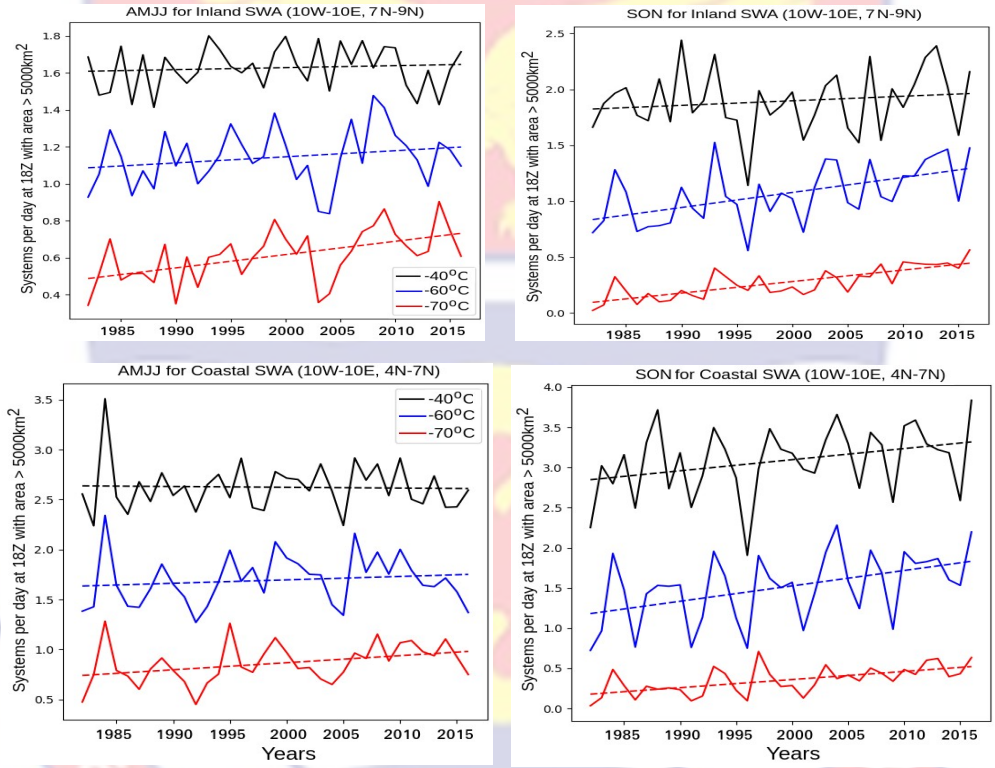

Figure 30: Regional MCS frequency at 1800 UTC at different temperature thresholds, derived directly from measurements onboard the Meteosat geostationary satellites for AMJJ (left) and SON (right). Linear trends are shown as dashed lines

It was observed also that the Sudan sub-division realised clear increasing trends in both rainy seasons for all threshold. In the absence of a clear trend in mean annual rainfall (which is driven by the not-so-clear trend in MCS mean temperature) in the first rainy season, the frequency of intense

MCSs continue to rise. In the SON season, it could be seen that mean annual rainfall increased as well as the intensity of rainfall (Nkrumah et al., 2019). This was evident in the clear increasing trends in both average MCSs and intense MCSs during the second rainy season for all three sub-divisions.

Trends in cloud frequency in the annual time series for each month is analysed over sub-divisions in SWA at different temperature thresholds (-40^{o}C, -60^{o}C and -70^{o}C) with that of selected rainfall events. This was to ascertain if trends observed in the rain gauge dataset can be linked with trends in cloud cover frequency. In doing this, monthly cloud cover frequency trends were analysed instead of seasonal to know particular months contributing to most of the changes in the seasonal intensification over SWA, with interest over the Inland and Coastal sub-divisions which portray a bimodal rainfall pattern. Frequency of cold clouds at temperature thresholds (-40^{o}C, -60^{o}C and -70^{o}C) were compared with daily mean rainfall, mean intensity of rainfall and average monthly maximum rainfall.

For the Inland sub-division, strong intensification trends were observed during the early part of the year in February, March and April at all three MCS thresholds with significant increases at -60^{o}C and -70^{o}C (Figure 31). It was noticed that very cold systems realised a clear significant trend across the whole year. Trends in MCS frequency tend to significantly increase at all thresholds in June and October, depicting a general increase in storm activities mainly during these months over the inland sub-division. This can be a reason for clear trends in rainfall intensification and the not-much changes in rainfall totals over the first rainy season. The second rainy season realised a clear trend increase at -60^{o}C and -70^{o}C MCS in October and November. This trend was

clearly observed in the rainfall regime over this region in terms of rainfall intensification (Nkrumah et al., 2019).

Daily mean rainfall was observed to have clear increasing trends in February, October and November. It was interesting to note that the daily mean rainfall correlated well with MCS frequency at all temperature thresholds in February and March, just before the start of the first rainy season, with a maximum correlation value of 0.8 recorded in February for average and cold clouds (Figure 31). A good relationship of average MCSs with July daily mean rainfall can also be observed with a 0.69 correlation value.

During the second rainy season, it was noted that there existed a positive correlation between daily mean rainfall and all temperature thresholds in October. In November, the daily mean rainfall showed a good relationship only with average MCSs.

Comparing MWD to MCS frequency at the diffierent temperature thresholds, it was observed that there was not much of good correlation over the period except for February and June which display appreciable relationship for the daily intensification of rain and average and cold cloud systems (Figure 32). It was however realised that mean intensity of rainfall in the month of November realised a clear increase in trend after 2005. This trend increase could be observed also in average and cold cloud systems in the same month, insinuating the possibility of a good relationship between mean intensity and MCS frequency in the last decade.

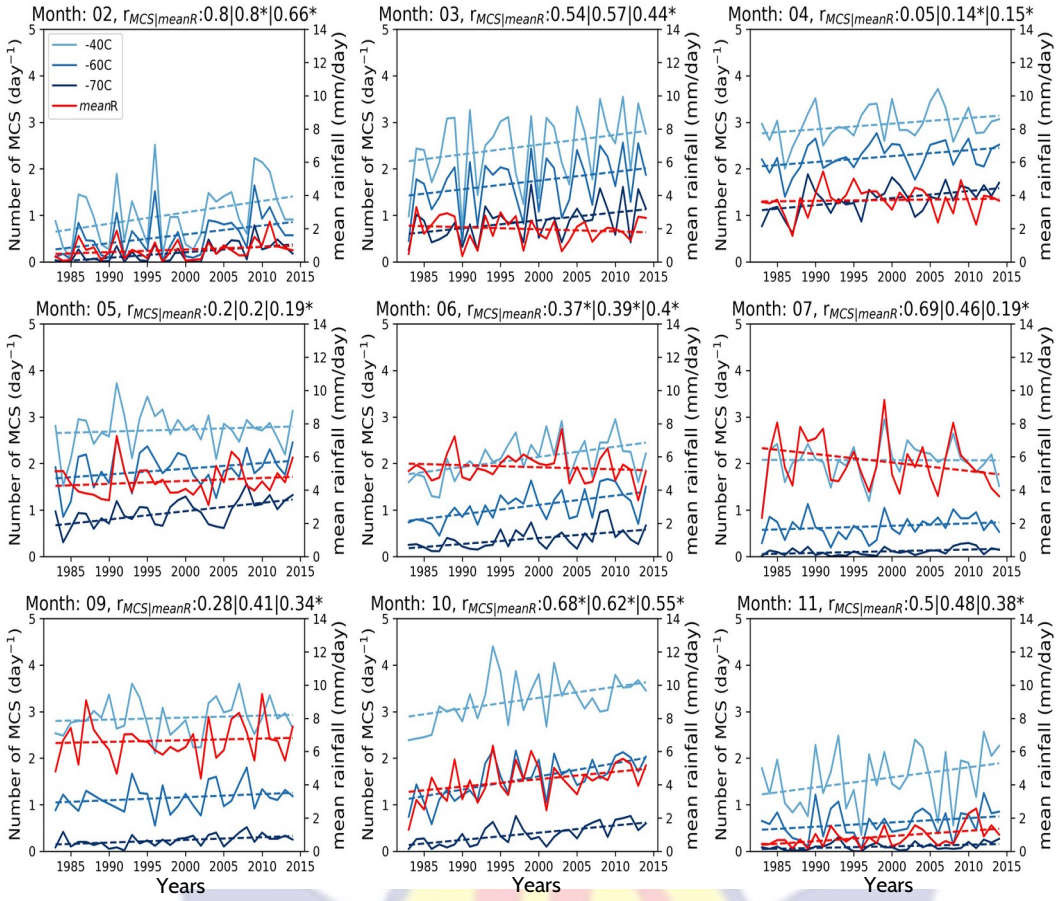

Figure 31: Regional MCS frequency identified from GridSat data using temperature thresholds of -40°C, -60°C and -70°C, sampled at 1800 UTC and daily mean rainfall from rain gauge stations over Inland sub-division of SWA as monthly averages. Dashed lines denotes trends. Titles show the correlation coefficients between temperature thresholds and daily mean rainfall, with asterics showing significant MCS frequency trend ($p \leq 0.05$) for temperature thresholds of -40°C, -60°C and -70°C.

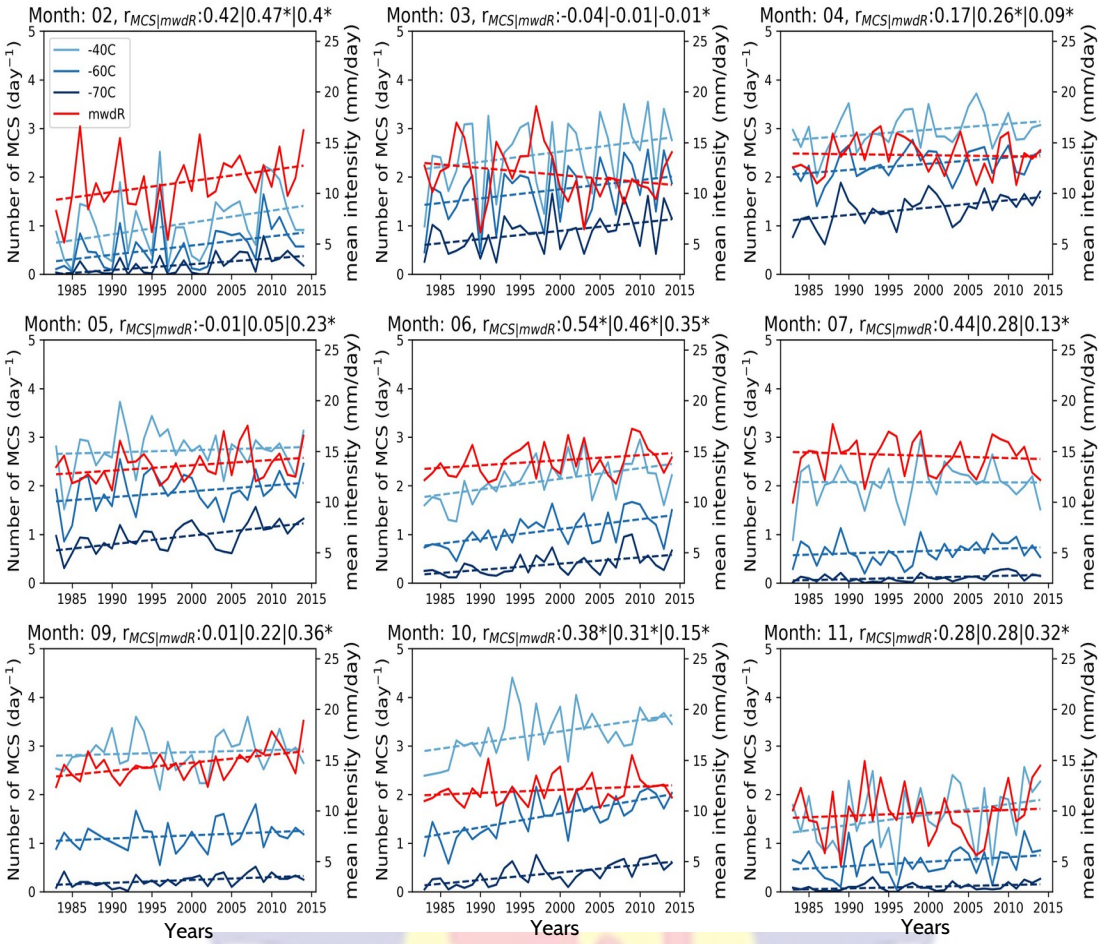

Figure 32: Same as figure 31, but for mean intensity of rainfall

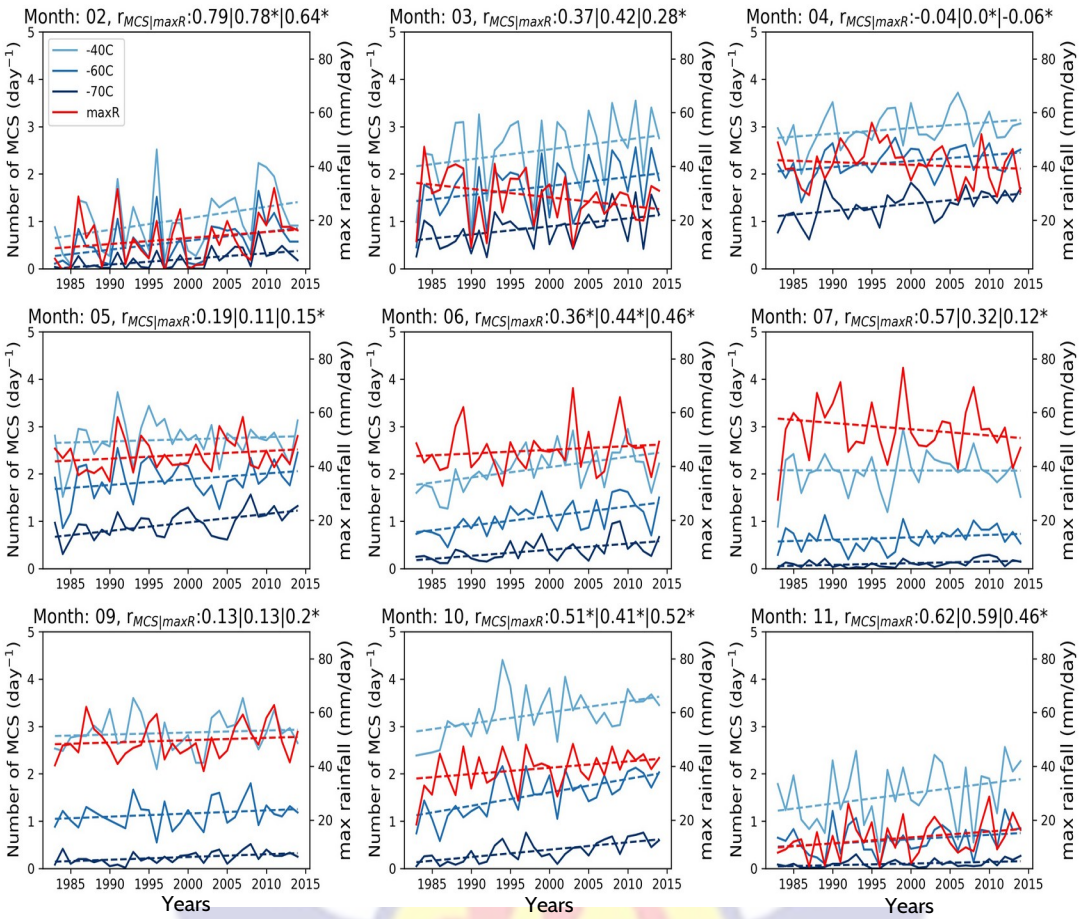

Figure 33: Same as figure 31, but for average maximum rainfall

The average maximum rainfall trend was correlated with the different temperature thresholds of interest. It could be noted that average maximum rainfall correlates well with MCS frequency at all temperature thresholds in February, with a maximum correlation value of 0.79, 0.7 and 0.64 for average, cold clouds and very cold clouds respectively (Figure 33). Average MCSs in July correlated positively with average maximum rainfall with a 0.57 correlation value. June tend to show an appreciable positive correlation between Average maximum rainfall and all temperature thresholds.

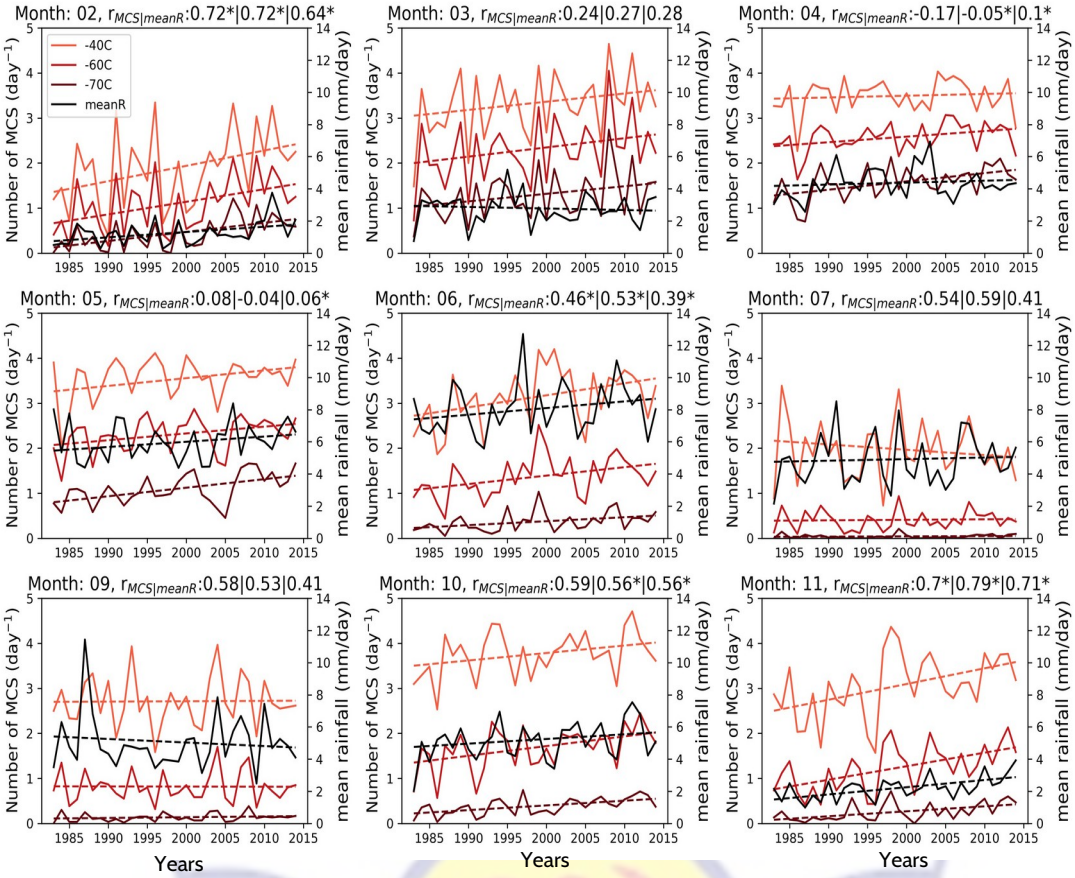

Figure 34: Regional MCS frequency identified from GridSat data using temperature thresholds of -40°C, -60°C and -70°C, sampled at 1800 UTC and daily mean rainfall from rain gauge stations over Coastal sub-division of SWA as monthly averages. Dashed lines denotes trends. Titles show the correlation coefficients between temperature thresholds and daily mean rainfall, with asterics showing significant MCS frequency trend ($p \leq 0.05$) for temperature thresholds of -40°C, -60°C and -70°C.

During the second rainy season, it could be noted that there existed a positive correlation between average maximum rainfall and all temperature thresholds in October and November. In November, the daily mean rainfall showed a good relationship only with average MCSs. It was observed that average maximum was to be influenced by the frequency increase in MCS

trends clearly during the second rainy season, but the same was true in the early part of the year.

Over the Coastal sub-division (Figure 34), trend increase in MCS temperatures behaved just like over the Inland sub-division (Figure 31), only that the February signal doesn't look like a trend, but more of an increase from 1999 onward which is in tandem with (Taylor et al., 2018). Nevertheless, February, June and November have -40^{o}C ,-60^{o}C and -70^{o}C increasing significantly, with November again not depicting a smooth trend, but more of a change around 1997 (Figure 34). Cold and very cold clouds observed significant increases in April, May and October. These changes contribute to changes in the rainfall regime over the Coastal region of SWA. It was realised that more of the changes in seasonal trends in the rainfall changes over SWA in the first rainy season was contributed in the month of June, whilst in the second rainy season most of the contribution was observed in the months of October and November (Figure 34).

A comparison between the daily mean rainfall and the different temperature thresholds of MCS frequency over the Coastal sub-division was carried out. It could be observed that a good positive correlation existed between each temperature threshold and mean rainfall in the month of February, which was before the start of the major rainy season.

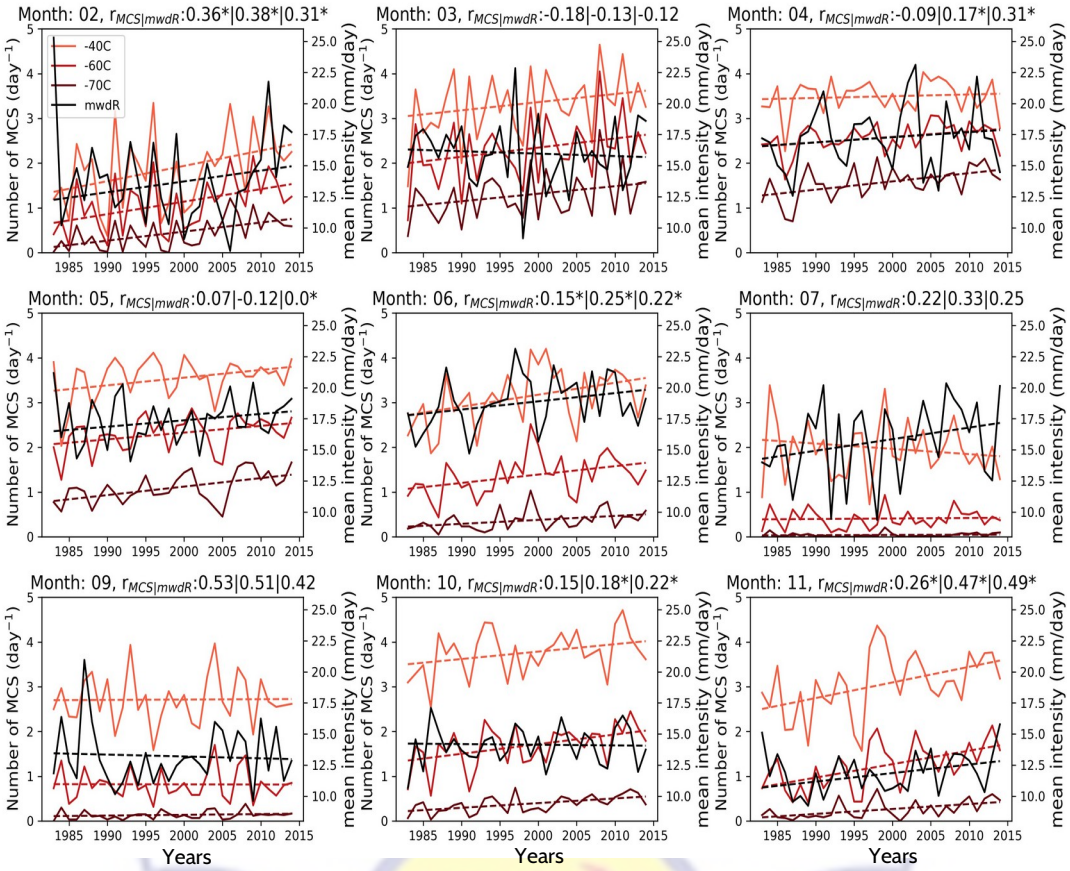

Figure 35: Same as figure 34, but for mean intensity of rainfall

During the first rainy season (AMJJ), it was realised that daily mean rainfall increased as MCS frequency increased at all temperature thresholds in June and July. In the second rainy season, there existed a good correlation between observed parameters in September, October and November, with November recording a least correlation of 0.7 for average MCS trends and its relationship with daily mean rainfall. This depicts the influence of storm systems on trends in daily mean rainfall in the second rainy season over the Coastal sub-division.

A look at the relationship between mean intensity and MCS frequency at the different temperature thresholds showed clearly an appreciable positive correlation only in September and November in the second rainy season over

the Coastal sub-division of SWA (Figure 35). It could be noted then that rainfall intensification over the second rainy season in recent decades could be attributed to the intensification in cold cloud trends over the Coastal region. Also, although there exist an intensification of rainfall in the first rainy season, it is not much influenced by cold cloud trends. Considering how MCS frequency influence average maximum rainfall over the Coastal sub-division, it was observed that there existed a good positive correlation between the various MCS thresholds and maximum rainfall in February and November (Figure 36).

It was interesting to note that cold cloud frequency trends correlated well with rainfall events in months leading to the first rainy season (mainly February). On the other hand, cold cloud frequency trends well correlated with rainfall events during the months in the second rainy season. The pronounce increase in February cold MCSs could point to an early onset in intense mesoscale convective systems over the Coastal as well as the Inland sub-divisions of SWA. Similar trends were observed over the Congo Basin (Taylor et al. 2018).

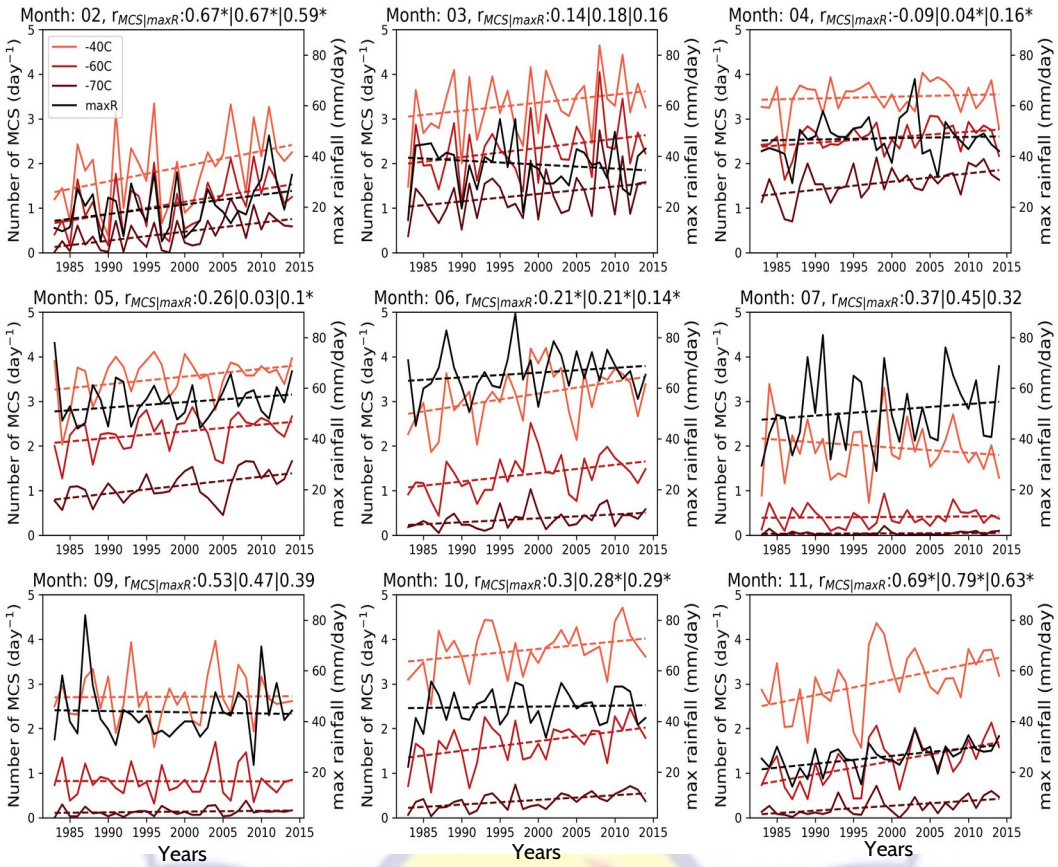

Figure 36: Same as figure 34, but for average maximum rainfall

Annual cycle comparison of large-scale shear- and moisture-related environment

In the following, the annual cycle of MCS cloud top temperatures and its related atmospheric drivers in the Coastal and Inland sub-divisions of SWA were analysed. A further analysis was carried out to ascertain how these MCSs over the year could be associated with wind shear and low-level atmospheric moisture.

It was observed over the Coastal sub-division that average cold cloud temperatures get to its lowest temperature in April, although temperature for cold cloud for March was as well low (Figure 37a). It should be pointed out

here that rainfall over this region peaks two months after the cloud top records its lowest temperature. Interestingly, it was realised that the lowest rainfall rate coincides with the warmest cloud temperatures in August. This is mainly due to the position of the rainband, which lies north of SWA in the month of August. Cloud top temperatures become colder again during the second rainy season with a peak of -61.36^{o}C in November (Not so different from the -60.88^{o}C recorded in October), although rainfall peaked in October. It was noticed also that both the low-level atmospheric moisture and wind shear followed the path of the cloud top temperature, with both atmospheric drivers peaking in April and realising their lowest events in August. Both atmospheric drivers also recorded a second peak in October as observed in the rainfall pattern (Figure 37b).

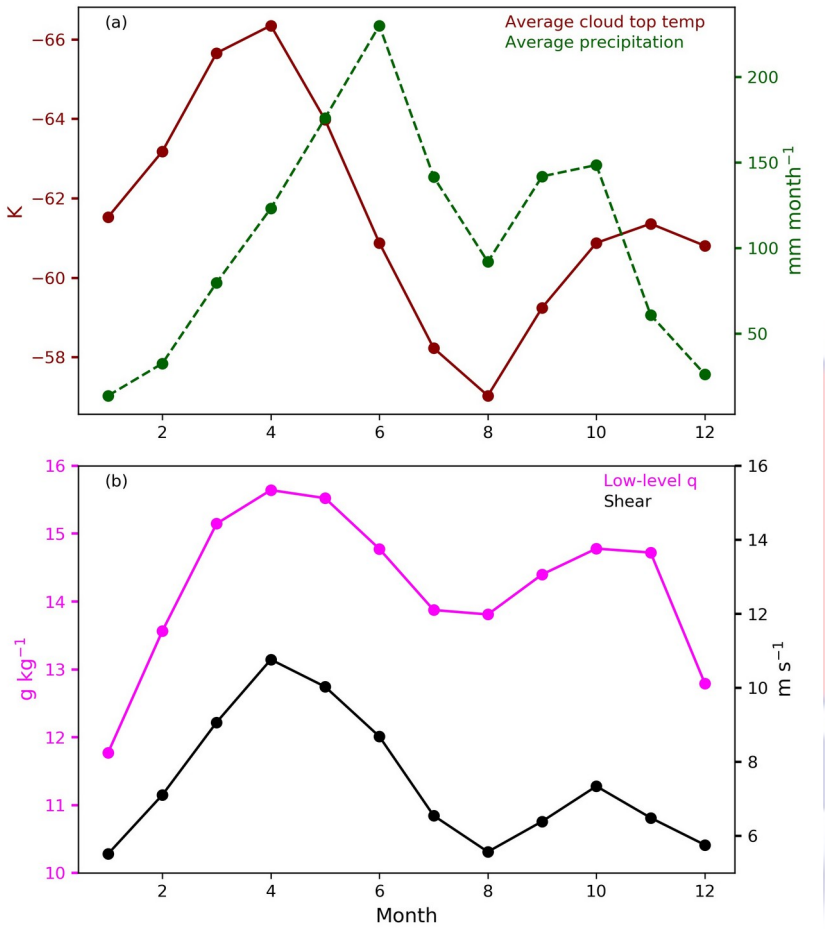

Figure 37: Regional average annual cycle of (a) cloud top temperature at 1800 UTC and precipitation from rain gauge data and (b) low-level moisture and shear at 1200 UTC over the Coastal sub-division of SWA.

One notable pattern was that wind shear reduced greatly in the second season by almost 3 ms^{-1} from the first rainy season, whiles low-level moisture reduced slightly and therefore dominated the second rainy season.

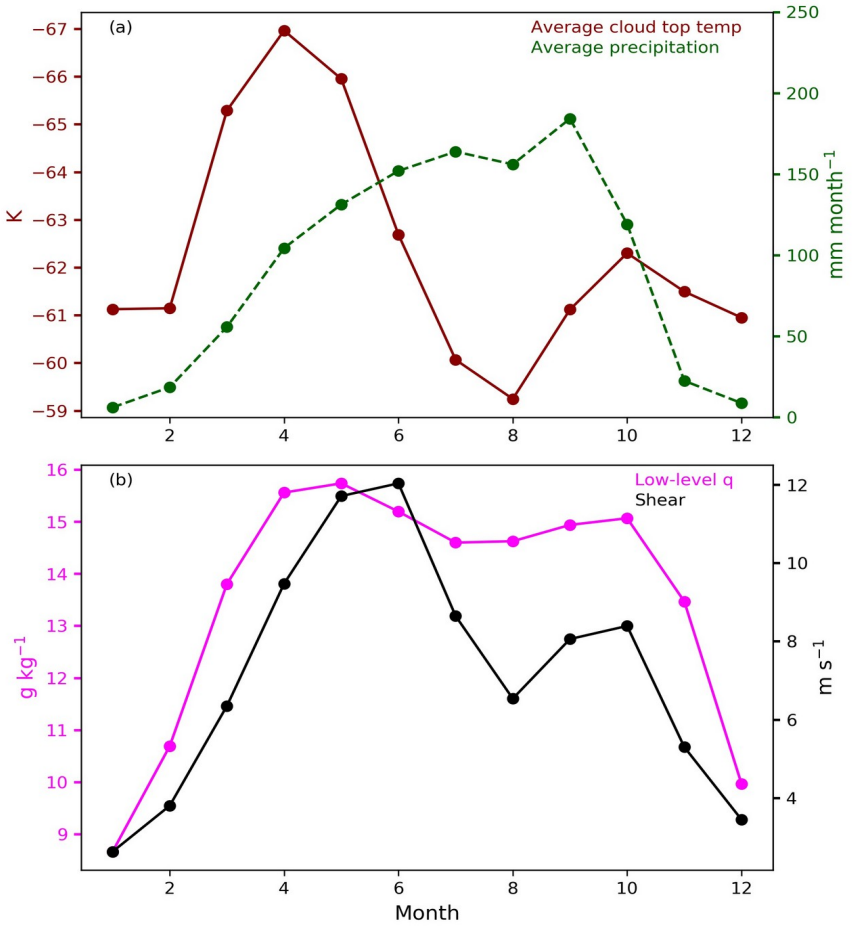

Figure 38: Same as figure 37, but for the Inland sub-division of SWA.

Over the Inland sub-division, average cloud top temperature pattern remained same as in the Coastal region but with a clear second peak in October (Figure 38a). Rainfall in this region did not show a clear peak in the first rainy season, but displayed a second peak in the month of September. Peaks in low-level moisture and wind shear tend to shift forward to May and June respectively but both observed a second peak in October during the second rainy season (Figure 38b). Low-level atmospheric moisture remained high across the year as wind shear activities diminished during the second rainy season. It can be pointed out that wind shear and low-level moisture tend to travel northward with the movement of the the ITCZ and the AEJ and

therefore seem to peak at other times in the year depending on their latitudinal location.

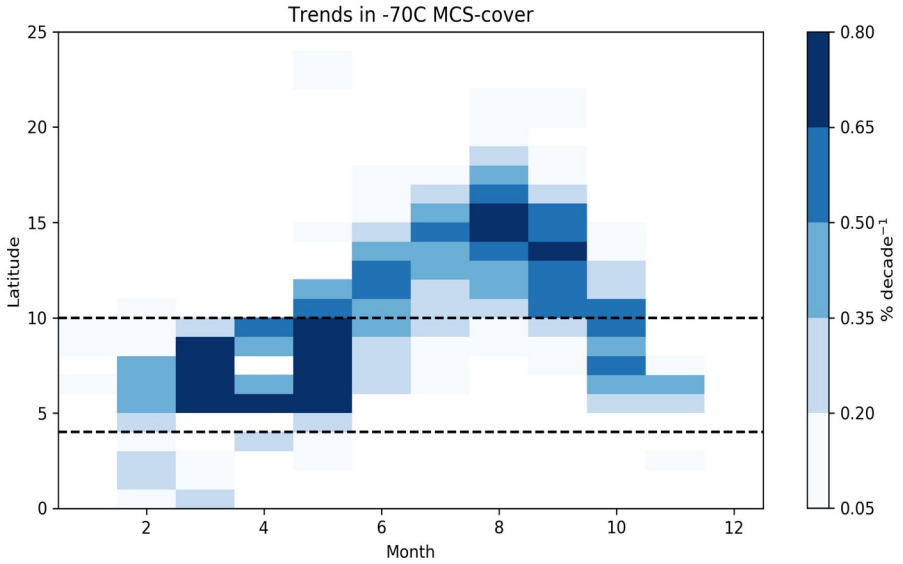

Figure 39: Significant trends at -70°C cold cloud cover of storms larger than 5000 km^2 (shading, %, p ≤ 0.05) at 1800 UTC

Trends in cloud cover of intense MCS (-70°C) was depicted in Figure 39. It can be observed that an overall strong trend in intense MCS cover (dark blue, significant at $p < 0.05$) was observed in March, April and May. Following the movement of the WAM, cloud cover intensification was realized throughout the year over the West African region. The SWA region (area between dashed lines) observed significant intensification in February, March, April, May, October and November.

These trends were then linked to trends in wind shear and atmospheric humidity over both the Coastal and Inland sub-divisions of SWA. Figure 40 shows negative correlation coefficients between mean MCS temperatures and wind shear all through the year, with the exception of October which displays a positive trend. Significant trends were observed in February and March, with

the month of March reaching a minimum coefficient of -0.68. This means that wind shear tend to increase as cloud tops become colder and decrease as cloud tops become warmer.

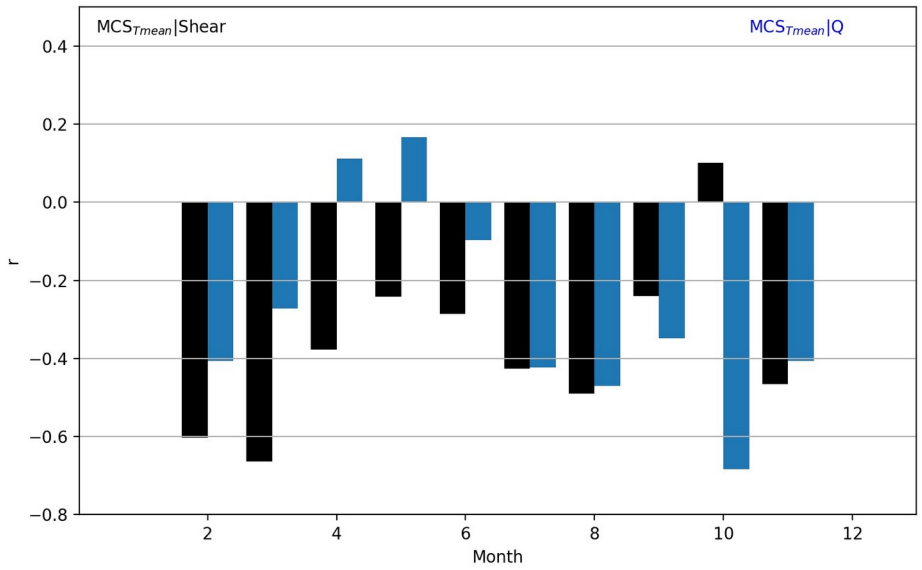

Figure 40: Mean MCS temperatures with wind shear (black bars) and 925 hPa specific humidity (blue bars) over Coastal sub-division of SWA.

The correlation between MCS and shear seem to be weak in the second rainy season. This suggests that the intensity of MCSs is modulated by the activities of wind shear during the first rainy season, with intense modulation in the early months of the season as compared to the second rainy season. A stronger correlation of MCS trends with low-level moisture took over from July onwards and reached a minimum of -0.61 in October. The Inland sub-division showed similar relationship between MCS trend with shear and low-level moisture as observed in the Coastal region (Figure 41), although appreciable correlation was observed between MCS and low-level moisture during the second rainy season in the Coastal region than in the Inland region. There also existed no correlation between MCS temperatures and shear in the

month of October over the Inland sub-division although the month of November gains more contribution from shear activities in the development of cold clouds. It is worth noting that there existed a change in convective regime where low-level moisture dominates the second rainy season over SWA. This allude to the different storm drivers that control the early first and second rainy season over SWA. It can be said therefore that the month of May serves as a transitional month between the shear-driven season and the moist-driven season (Klein et al., 2021).

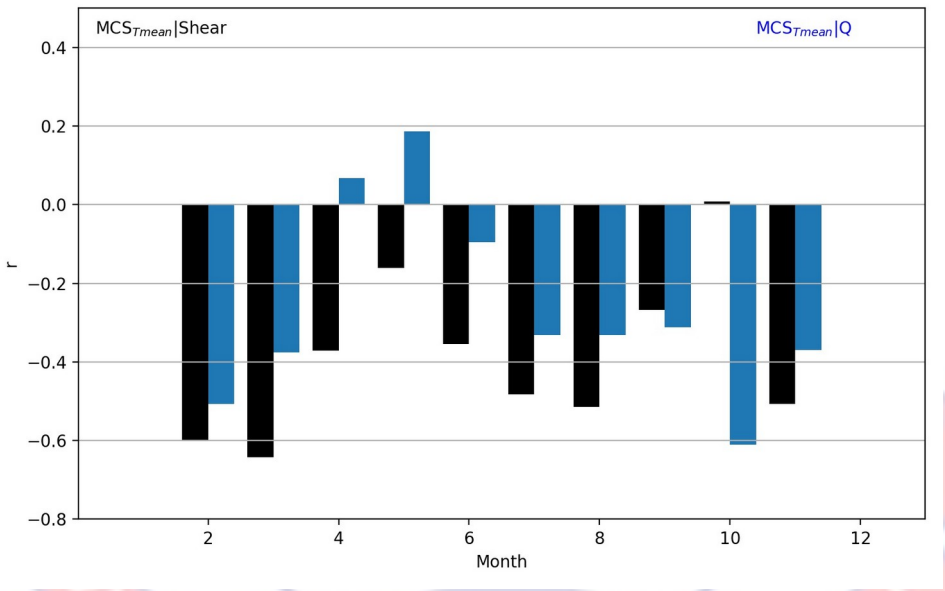

Figure 41: Mean MCS temperatures with wind shear (black bars) and 925 hPa specific humidity (blue bars) over Inland sub-division of SWA.

Rainfall versus average and intense mesoscale convective systems

A comparison of rainfall patterns to the number of MCS observed at the different MCS thresholds over the years was carried out to understand their association. This was done for the Coastal and Inland regions of SWA.

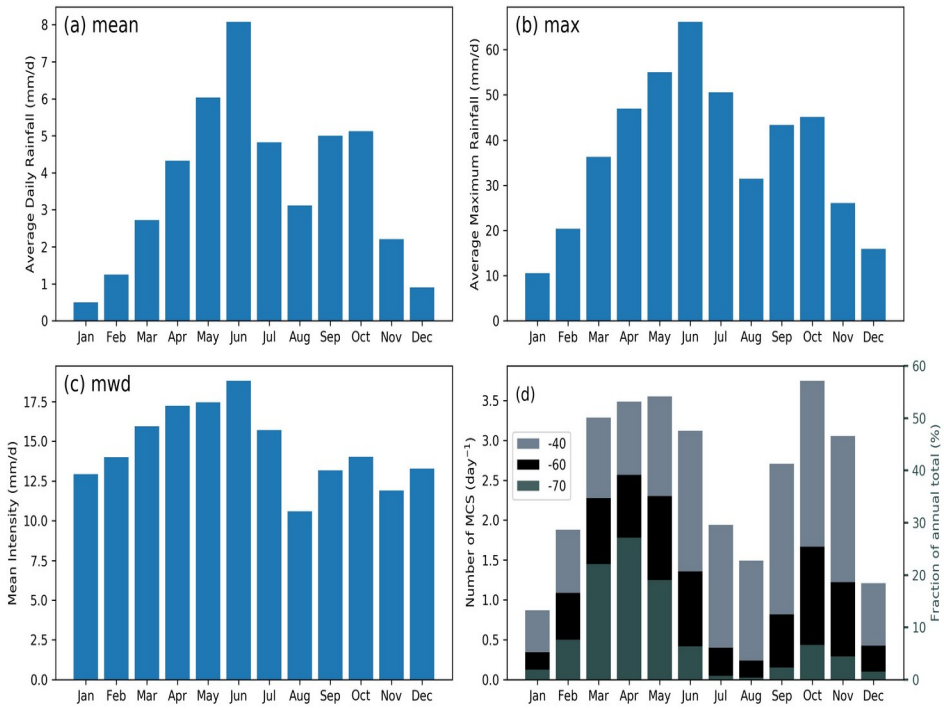

Figure 42: Average annual cycle (1983 - 2017) of (a) mean daily rainfall (b) average maximum (c) MWD and MCS at 1800 UTC, within the Coastal sub-division (d) the monthly average of MCS number per day at different temperature thresholds (left axis) and contribution to the annual total of intense (-70ºC) MCSs (right axis, %).

Comparing the various MCS thresholds (-40ºC, -60ºC and -70ºC) with mean daily rainfall, maximum and mean intensity rainfall patterns over the Coastal region, it was observed that the mean daily and average monthly rainfall clearly depicted the bi-modal system over Coastal regions of SWA with a high peak in the first rainy season (Figure 42 a, b and c). It was clearly seen that June received the highest daily mean and the highest daily maximum rainfall across the year. Mean wet day events, Figure 42c, tend to portray similar amounts, in the first rainy season and almost equal intensities in the

second. In Figure 42d, thresholds of -40ºC (-60ºC and -70ºC) depicted a first peak in number of MCS per day in May (April) and a second peak in October.

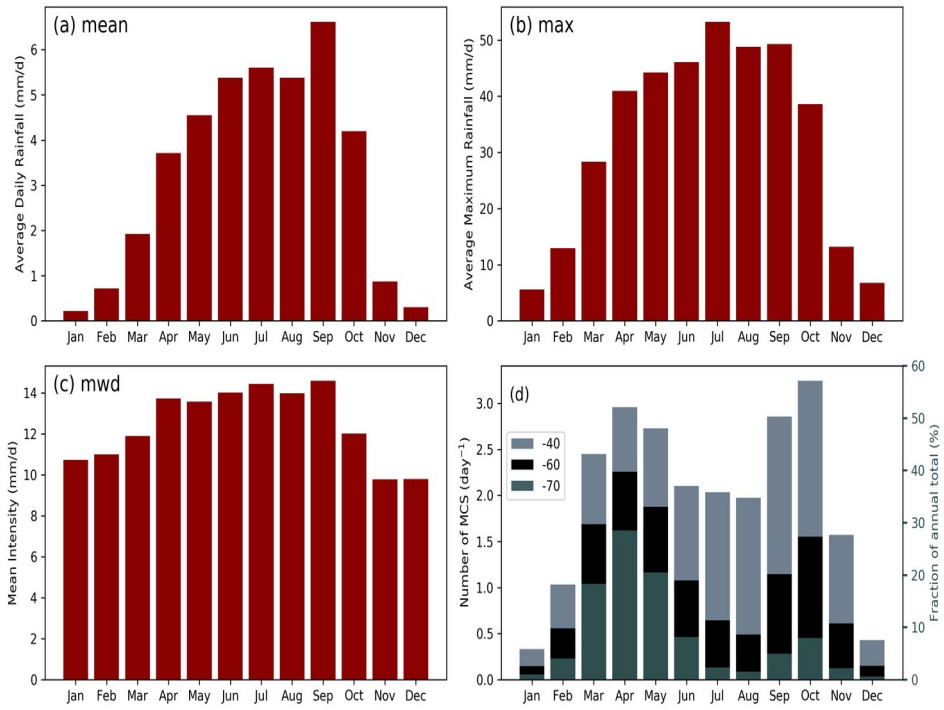

Figure 43: Same as figure 42, but for the Inland sub-division.

The month of November realised more MCS events under all thresholds as compared to September. It was realised that the second peak of number of MCS per month coincided with the second peak of rainfall in the Coastal region. The contribution of intense MCSs (-70ºC) to the annual total of MCS showed that early part of the first rainy season (i.e. MAM) observed almost about 70% whilst the second rainy season (SON) stays just below 20% over the Coastal Region.

Over the Inland region, it was observed that mean daily rainfall was high in the month of September, whilst average monthly maximum was high in July (Figure 43a, b). There seem not to be a clear distinction between the two rainy seasons in terms of mean daily rainfall, average maximum and mean

intensity of rainfall. In Figure 43d, all thresholds depicted a first peak in number of MCS per day in April and a second peak in October, with similar contribution of intense MCS to annual totals in the Coastal region. It was interesting to know that over the Inland region, September tends to record more MCS events as compared to November under all cloud top thresholds. It could also be noted that the number of MCS observed monthly over the Inland region does not depict the rainfall behaviour in terms of mean daily, average maximum and mean intensity. It was largely seen that more intense colder storms persist during the first rainy season as compared to the second (Maranan et al. 2018) that most rainbearing systems with deep and wide convective cores occur in March – May (MAM).

Trend analysis between rainfall events and MCS

A further investigation was made to understand the changes in trends of rainfall events in relation to MCS trends over the Coastal and Inland regions. Figure 44 depicts trend in average and intense MCS numbers respectively, with significant trends ($p \leq 0.05$) in darker shades of colours. Over the Coastal region, it was observed that February, June and November show significant trends under all MCS thresholds. It should be noted that majority of months with significant increase in average MCS are "moisture-sensitive". This confirms results in rainfall trends observed by Sanogo et al. (2015) which shows a strong trend in June for the first rainy season with a 25% contribution to annual precipitation and a coherent recovery in November during the second rainy season (Sanogo et al., 2015).

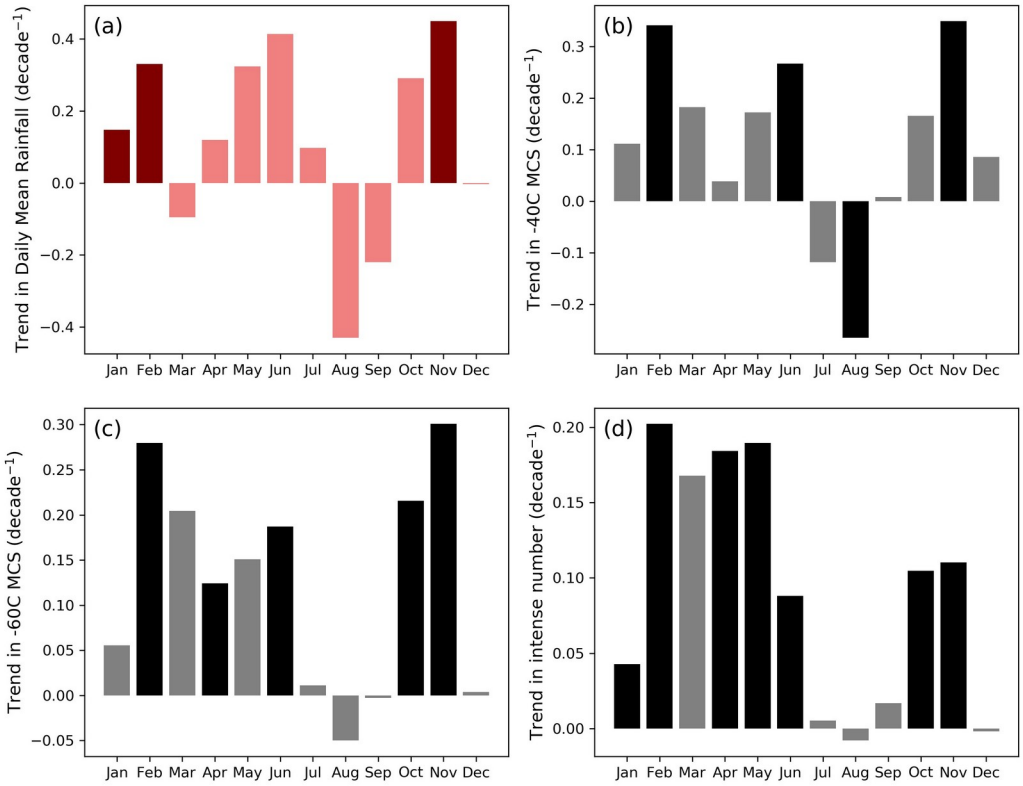

Figure 44: Trends in (a) mean daily rainfall and trends in MCS numbers at 1800 UTC within the Coastal region of SWA for (b) average MCSs, (c) -60°C MCSs, (d) intense MCS (decade^{-1}). Significant trends ($p \leq 0.05$) are shown in dark shade

This significance in trends of MCS in the months of February and November was well depicted in mean daily rainfall over the Coastal region (Figure 44a, b, c, d). It was also realised that January observed a significant trend with mean daily rainfall. This behaviour was noticed in intense MCS with a significant trend also in January (Figure 44d). There was a general increasing trend in rainfall and MCS events during both rainy seasons, with a high volatility in September and August showing a clear decreased trend.

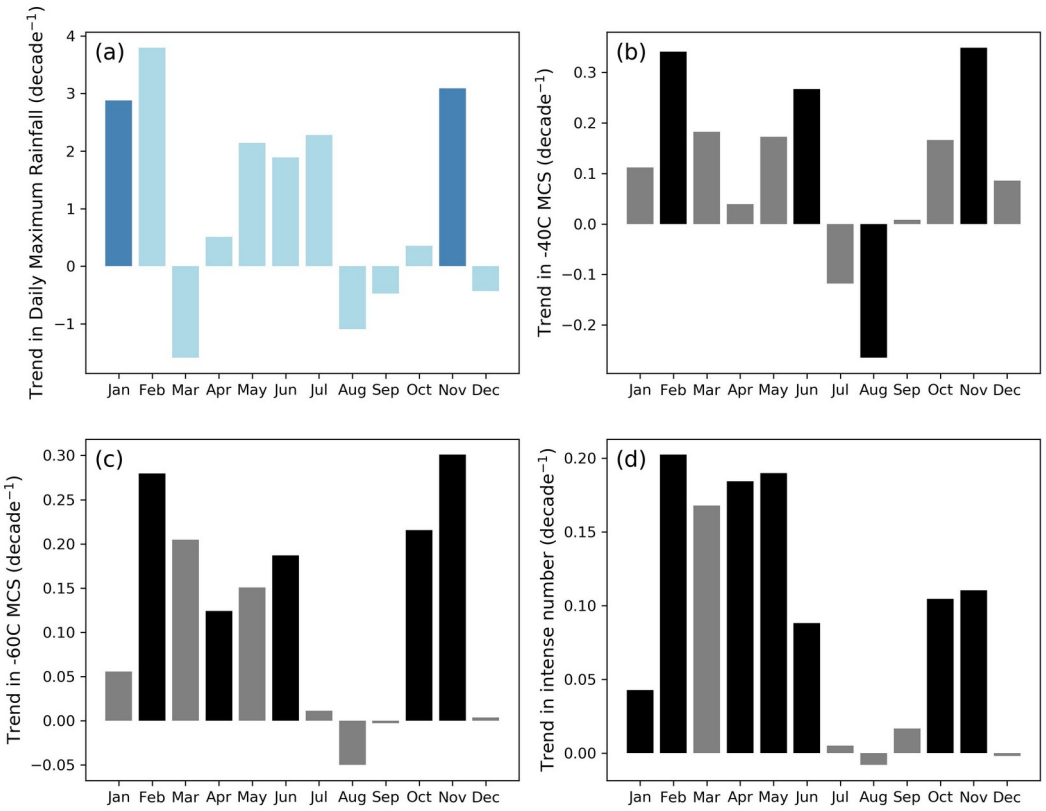

Figure 45: Same as figure 44, but for average monthly maximum rainfall

Trends in average monthly maximum rainfall were observed to be significant in the months of January and November, as seen in MCS trends over the Coastal region (Figure 45a). Average maximum tend to realised a decrease in March, which was not evident in MCS trends over the region. It can be noticed that trends in intense MCS increased significantly in most months across the year due to the abundace of moisture throughout the year. It could also be seen that intense MCS showed significant trends throughout the first part of the year, during the shear-dominated period leading to the first rainy season.

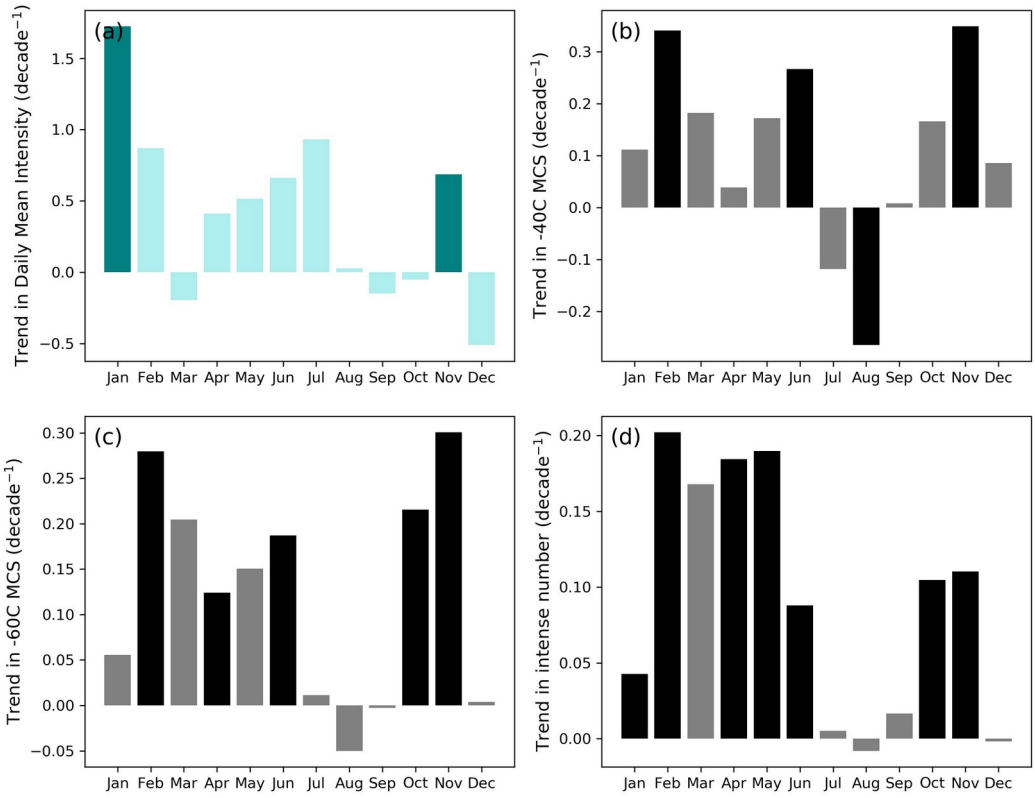

Figure 46: Same as figure 44, but for mean intensity of rainfall

The first rainy season, although realising increases in trends in average maximum rainfall, does not witness significant increase.

MWD observed an increasing trend throughout the first rainy season, and realised a significant increase in November and January. The months of March, September, October and December clearly observed decreases in trends, which were not depicted in MCS trends. It can be noted that the increase in mean intensity in recent decades over the second rainy season as displayed in figure 46 was mainly due to the increase in trends in mean intensity in November.

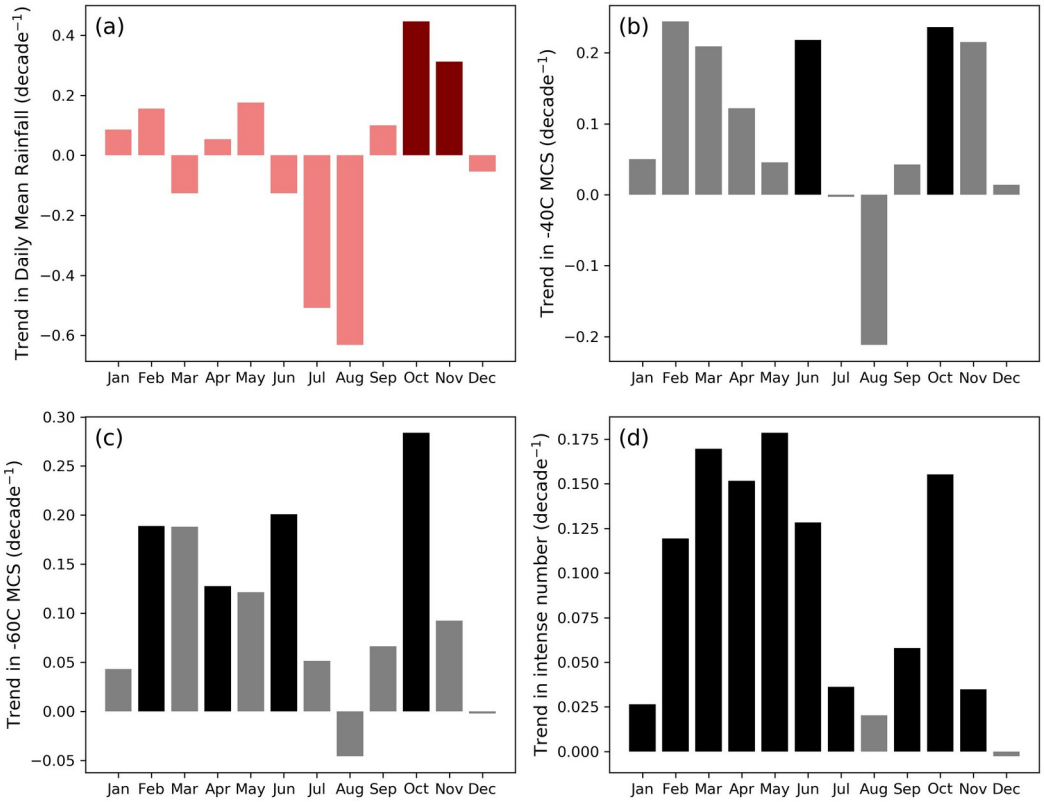

Figure 47: Trends in (a) mean daily rainfall and trends in MCS numbers at 1800 UTC within the Inland region of SWA for (b) average MCSs, (c) -60°C MCSs, (d) intense MCS (decade^{-1}). Significant trends ($p \leq 0.05$) are shown in dark shade

Over the Inland region, trends in mean daily rainfall realised significant increase in October and November (Figure 47a). This behaviour was depicted in both average and intense MCSs, as both observed significant increase in the month of October, with the intense MCS recording a significant increase also in November (Figure 47b, d). It was also clear over the Inland region that the first rainy season which was mainly shear-driven observed significant increase in intense MCS trends throughout the period.

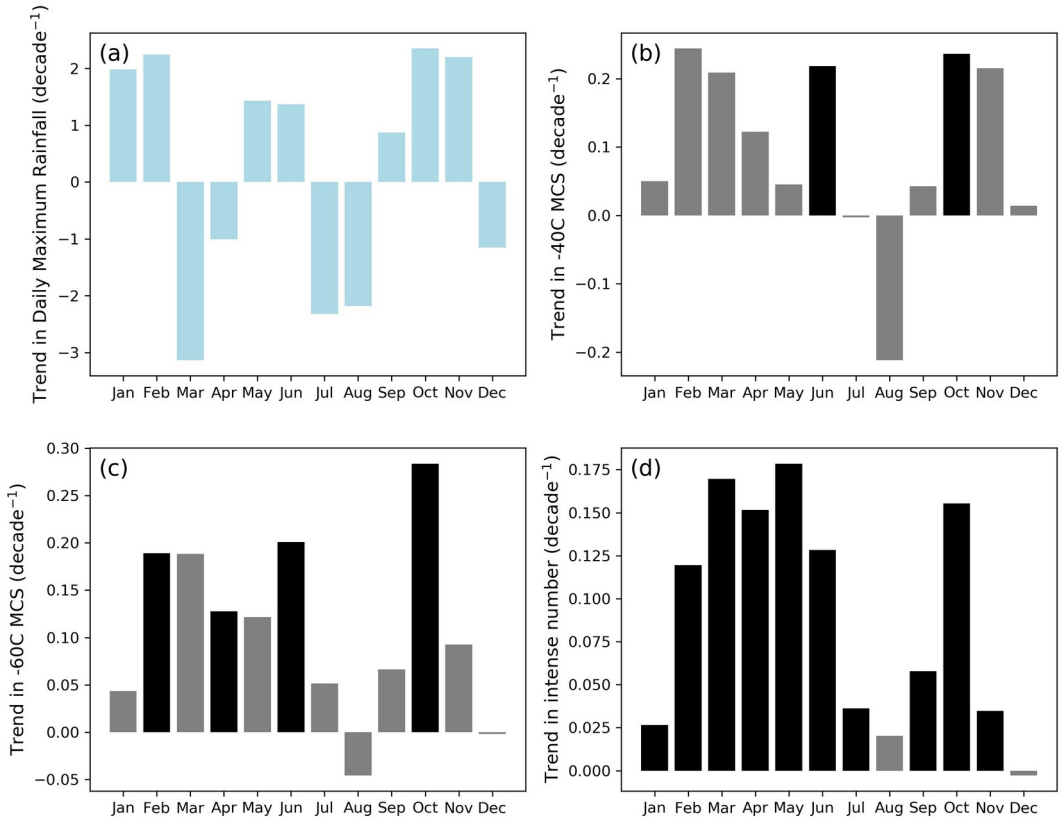

Figure 48: Same as figure 47, but for average monthly maximum rainfall

Patterns in figure 47 and 48 suggested that the increase in cloud cover at -70°C during the first rainy season is majorly linked to growth of storm tops and stronger convection. Although the month of June recorded significant increase in MCS trend under all observed thresholds (Figure 48 b, c, d), the mean daily rainfall and monthly maximum rainfall decreased. Average maximum rainfall over the Inland region recorded decreasing trends in March, April, July, August and December (Figure 48a). The rest of the months which are rainy periods observed increases but not significant trends.

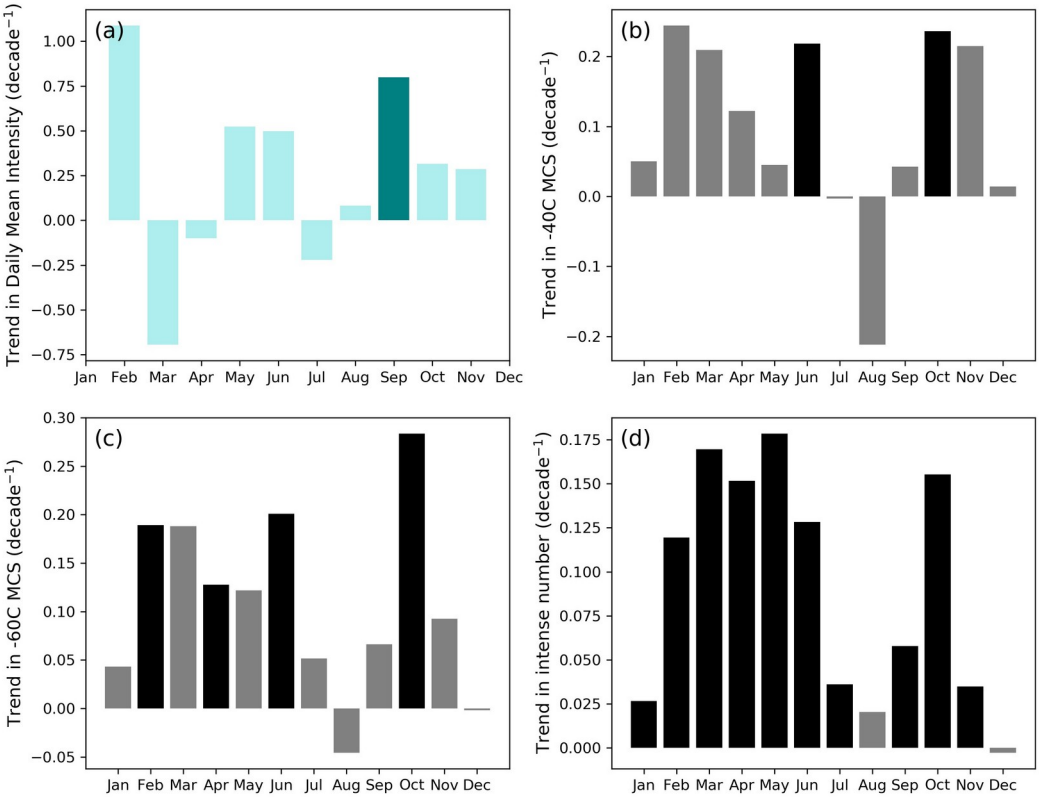

Figure 49: Same as figure 47, but for mean intensity of rainfall

Mean intensities over the inland region realised an increasing trend in all months except March and April (Figure 49a). Mean intensity tends to record a significant increase in September, which is not evident in the activities for average and -60°C MCSs (Fiure 49 c, d). This could be attributed to the significant increase in frequency of intense MCS trends in that same month over the Inland region (Figure 49d).

Looking at changes in MCS numbers over both Coastal and Inland regions, trends in February to June are only significant for intense rather than average MCSs, suggesting a dominant contribution from MCS intensification. Numbers in average and intense MCSs over both regions showed also significant increases later in the year, pointing to a tendency of more frequent

as well as more intense events. The fact that only the cold MCS subgroup shows significant trends during the shear-dominated part before and early in the first rainy season suggests that it is directly linked to MCS intensification (i.e., stronger convection and therefore higher storm tops). It can be pointed out from these findings that trends in rainfall during the first rainfall season is dominated by extreme rainfall events. The second rainy season, on the other hand, has realized a significant increasing trend in total rainfall amounts. This is projected by Nkrumah et al. (2019) in their study on rainfall trends with rain gauge data over the SWA (Nkrumah et al., 2019). In their analysis, it was observed that total rainfall amounts increased significantly in the SON season whilst extreme rainfall realized a significant increase in the first rainy season (Sanogo et al., 2015). Bichet and Diedhiou in 2018 observed similar trend patterns in rainfall in relation to significant trends in the first and second rainy seasons using remotely sensed data (Bichet & Diedhiou, 2018).

Storm environments over SWA

The different atmospheric large-scale conditions in which storms occur throughout the annual cycle, to understand why wind shear is a more important driver for storm trends during the early part of the first rainy season, whilst low-level moisture persist until November, were analysed. Much emphasis was placed on annual cycle of MCS intensity and its relationship to rainfall and its environment.

Over SWA, it was observed that average temperatures of MCS displayed regional variabilities with the cold systems taking place in the early part of the first rainy season (MAM) in the course of the year (Figure 50a).

The other peak of average temperatures of MCS was found in the second rainy season (SON) with storms 5°C warmer than in the first season. It could be noted then that storm systems in the early part of the first rainy season were more intense than what was observed in the second season. It can also be said that the areas of intense MCS do not coincide with the rainiest months in SWA (June, September and October). Figure 50b illustrates that average temperatures of MCS are characterised by high θ_e, depicting areas experiencing great warm air advection and moisture advection. Wind shear was high over areas of cold storms with a further coastal stretch during the early part of the first rainy season (Figure 50d). It can be observed in figure 50c that the rainiest months were dominated by total column water vapour. Low level moisture was realised to be high over areas with cold cloud systems and lower during rainiest months (Figure 50e). The combination of a high-instability and high shear environment produced coldest storms during MAM, and also resulted in high instantaneous rainfall rates from the MCSs (Figure 50f). This was confirmed in Maranan et al. (2018), who found that MAM mostly featured storms with deep and wide cores, which in more than 90% of the cases developed into mature MCSs with a vast stratiform cloud shield (Maranan et al., 2018). Therefore, those months actually receive a lot of rainfall from the trailing part of an active MCS and while the convective portion of rain might be intense, the monthly totals might be dominated more by long-lasting stratiform rainfall.

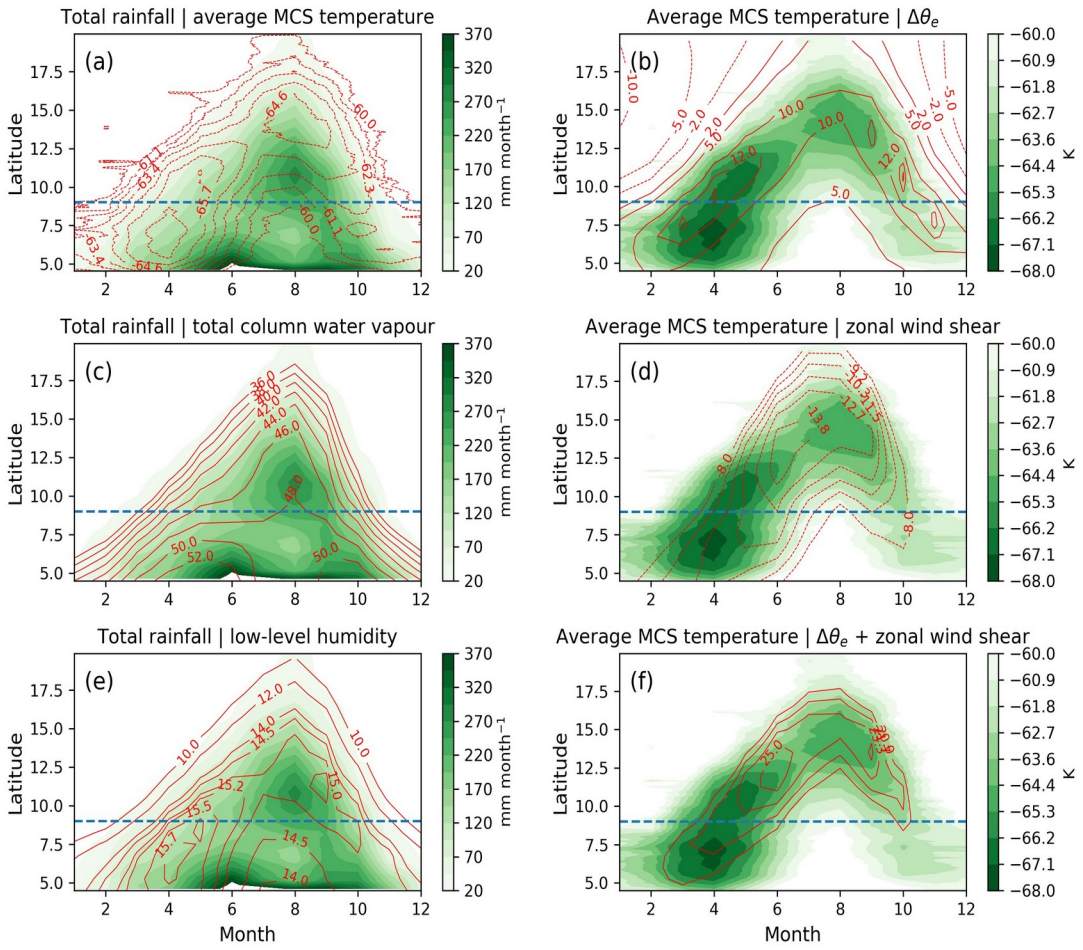

Figure 50: Average annual cycle across 10°W to 10°E for (a,c,e) CHIRPS rainfall (1981 - 2017, shading, mm month^{-1}) and (a) average MCS temperature (contours, K), (c) total column water vapour (kg m^{-2}), (e) 925 hPa specific humidity (contours, g kg^{-1}) and (b,d,f) average MCS temperature (shading, K) with contours showing (b) the 925 - 650hPa equivalent potential temperature difference Δθe in K, (d) the absolute 650 - 925hPa zonal wind shear in m s^{-1} and (f) the sum of wind shear and Δθe (Km s^{-1}).

Correlation between cloud top temperature and rainfall was therefore not strictly linear, but a trend to colder temperatures implied an intensification

of updraughts, which in most cases was linked to more intense rainfall even though this was limited by overall available atmospheric moisture.

Cloud top temperatures are therefore only a decent indicator for instantaneous convective rainfall amounts but correlates well with total rainfall amounts if convective rainfall dominates the total. This was true more in the moist second rainy season than in the first, when storms were smaller, more frequent and had shorter lifetimes than during the early rainy season (Maranan et al., 2018). From the relationship in seasonal changes established between MCS temperature and rainfall, it was noted that the atmospheric conditions that prevail during MAM was shear dominated whilst conditions that existed during the SON period was moisture dominated. This seasonal variation in the convective regime over SWA was identified also by (Klein et al., 2021).

The shift from shear regime to moist regime

Figure 51 displays atmospheric variations observed in the change from a shear regime to a moist regime for different months in the year with interest in the period of rainfall. Starting from the pre-monsoon period where mean MCS temperature tend to be very cold, it was realised that the SWA region sat just around the northernmost position of the AEJ. The dashed vertical lines mark the boundaries of the SWA region with the two sub-divisions, which was the region of focus. Looking at how some atmospheric variables behave during the rainy season, an understanding of what might contribute to the regime changes in the rainfall events was realised.

Moist static energy (MSE) tend to be very high over the focused region at lower levels of the atmosphere. The maximisation of MSE over lower levels in this region may be due to increasing moisture content and increasing temperatures close to the coast. This region of increased humidity is capped with a very warm and dry air of the Saharan air layer (SAL) around 750 - 650hPa, leading to adequate instability areas that serve as burst points for thunderstorms and MCSs. In March, average (black line) and intense MCS (red line) both occur over the same region with little or no systems forming in the sahelian region. It was observed that as the months progressed from March to May for the pre-monsoon season, the frequency of average and intense MCSs reduced over the SWA region. It was noted also that the decrease in MCS activity over the SWA region corresponded with the northward shift in the AEJ. As the AEJ moves northward, it takes the peak of intense MCS along with it. This was evident in June, which showed high instability/high shear conditions just north of 10N, as the SWA remained more stable with an evenly distributed moist conditions prevailing to the south of the AEJ. As a consequence of this increased atmospheric stability, developing MCSs over SWA were predominantly of a warmer, less explosive type.

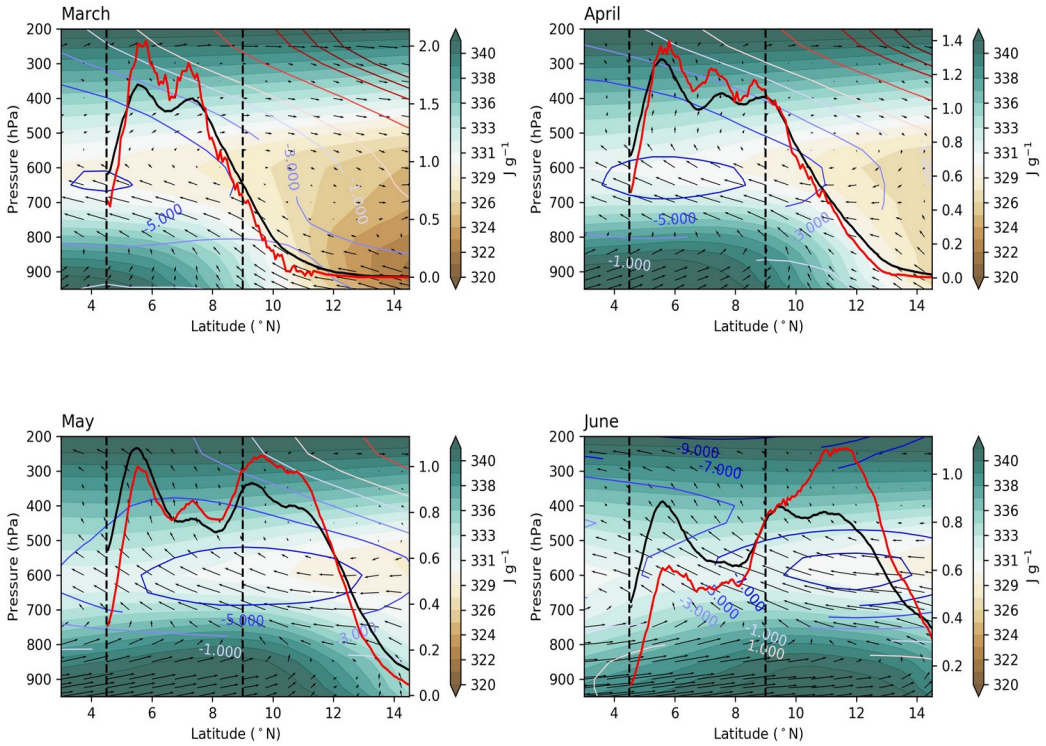

Figure 51: Monthly average 1200 UTC cross-sections between 10°W to 10°E of the moist static energy (shading, J g^{-1}), meridional wind vectors (m s^{-1}, w-component was multiplied by 10 for better visibility) and average frequency of MCSs (black line) and intense MCSs (red line) at 1800 UTC for March, April, May and June.

As the AEJ retreated from it northernmost position from September, the peak of MCS intensity also retreated with it, reintroducing a cap of dry air over the SWA region (Figure 52). This increased the low-level wind shear over SWA. The moist regime introduced in June stayed through to October, creating adequate instability due to the high MSE which in turn provided the needed environment for storm intensification. Convection developed towards regions of high MSE. Since high values of low-level MSE (equivalent to θ_e) imply high CAPE, areas of maximum MSE favour convection. A lifting mechanism within an area of high MSE enhances convection. At the same

time, a strong capping inversion or subsidence aloft may suppress convection in a high MSE environment. Although fewer MCS systems occur during the SON season, rainfall events take place frequently due to existing high moisture content in the atmosphere around this period.

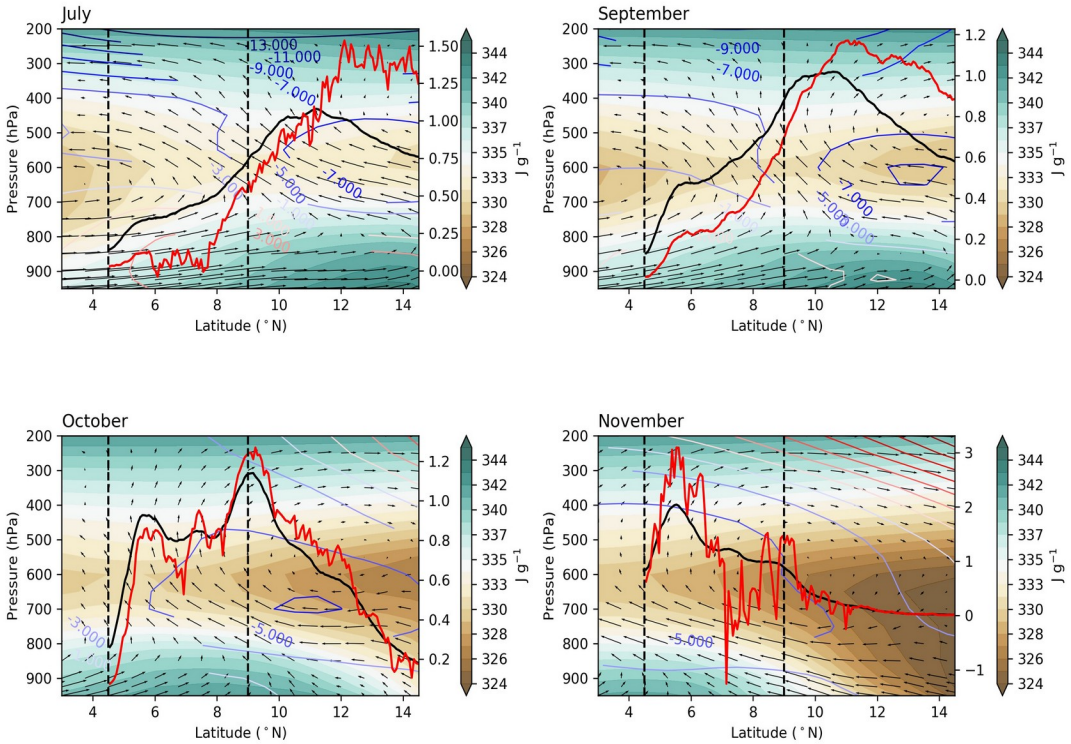

Figure 52: Same as in Figure 51 but for July, September, October and November

The transport of the total column water vapour and equivalent potential temperature difference ($\Delta\theta_e$) were further analysed over the SWA region. It was noticed that total column water vapour mostly stayed below 50 kg m^{-2} with $\Delta\theta_e$ maximised over the coastal region of SWA in March and April (Figure 53). The peak of $\Delta\theta_e$ moved northward as the AEJ moved northward. It was observed that MCSs that fall into the 'intense' category contribute to

about 30% of cloud systems over SWA in March. The contribution of intense MCSs increased to about 40% in April and May. In June, $\Delta\theta_e$ reduced drastically over the SWA region. As a result of this, there was increased stability, with developing MCSs which are less explosive type with only 18% reaching intense characteristics.

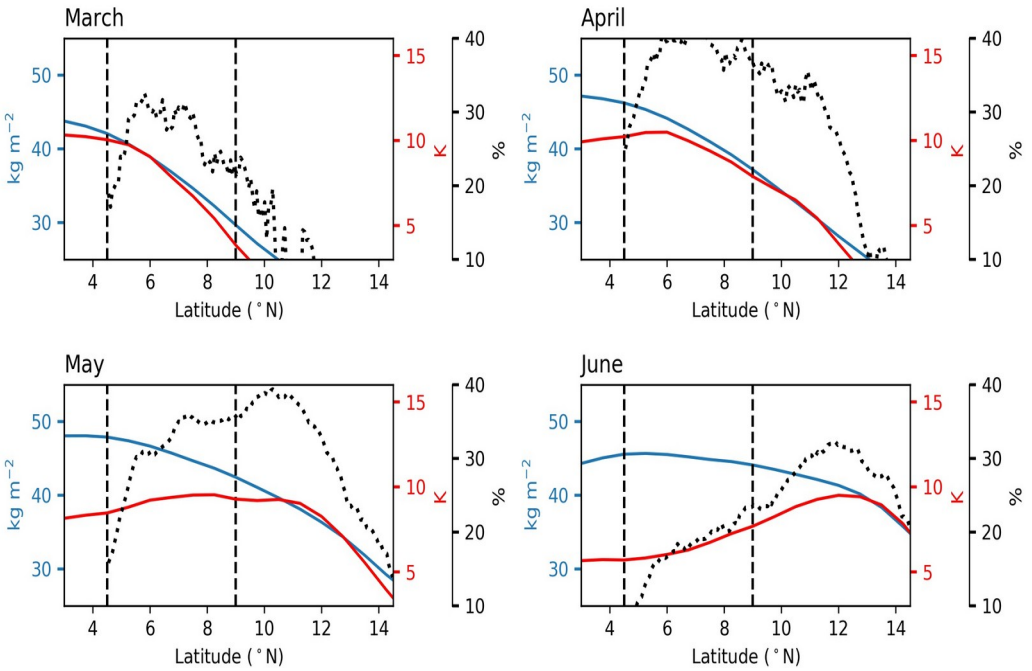

Figure 53: Plots of total column water vapour (blue, kg m^{-2} , Δθe (red, K) and the contribution of intense MCSs to the total of MCSs (dotted, %).

The second rainy season realised similar levels of total column water vapour as the first. In August, which marked the break in the rainfall season over SWA, there seemed to be no MCSs with intense characteristics (Figure 54). As the AEJ retreats to the south in September, the contribution of intense MCSs to convective activities started to appreciate southwards. In the SON season, the contribution of intense MCS seemed to be at its peak of about 17% in October over SWA. Due to increase in $\Delta\theta_e$ in October and November,

instability conditions started developing and traveled along the edge of the AEJ as it moved northward and southward.

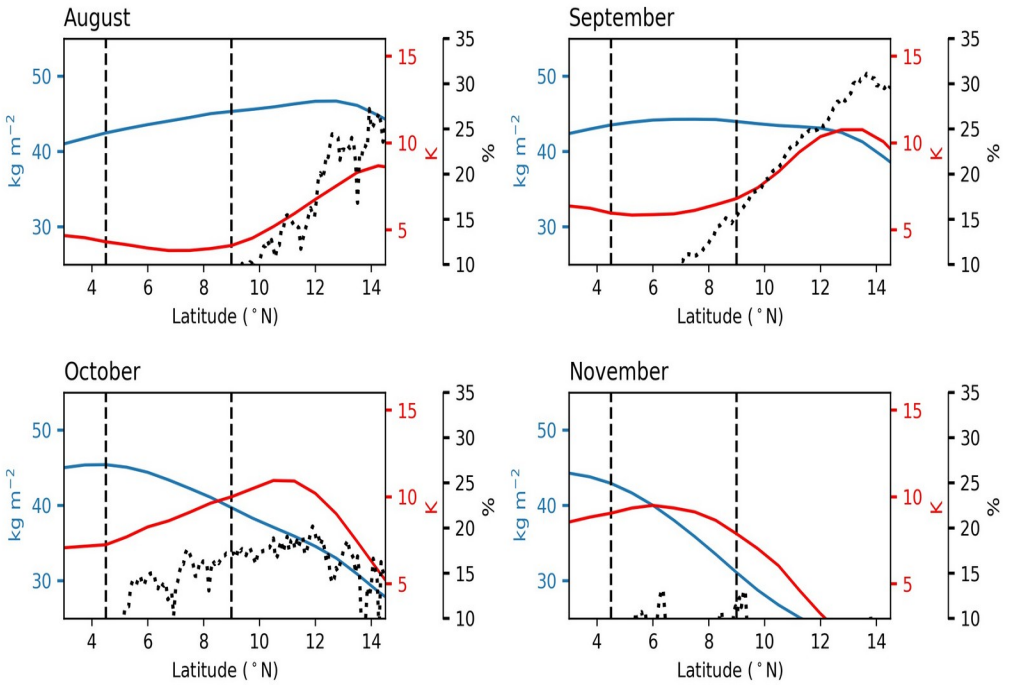

Figure 54: Same as in Figure 53 but for August, September, October and November

Atmospheric environment before event-time

Dependence of drivers for intense MCSs on the atmospheric regime

It was noted that shear conditions were prominent in the atmosphere during the ascent of the AEJ to the sahel and switch into a more moisture dominated regime as soon as the jet moves past SWA. These observed trends can be said to be highly sensitive to the timing of the movement of the entire monsoon system over the West African region. An evaluation of whether different intensities of MCSs occuring during the two rainy seasons might be intense due to different atmospheric drivers was carried out. In doing this, a

composite of pre-convective atmospheric conditions from the reanalysis ERA-interim data at 1200 UTC on the days of the storm (MCS between 1800 UTC) and at the storm location were compiled.

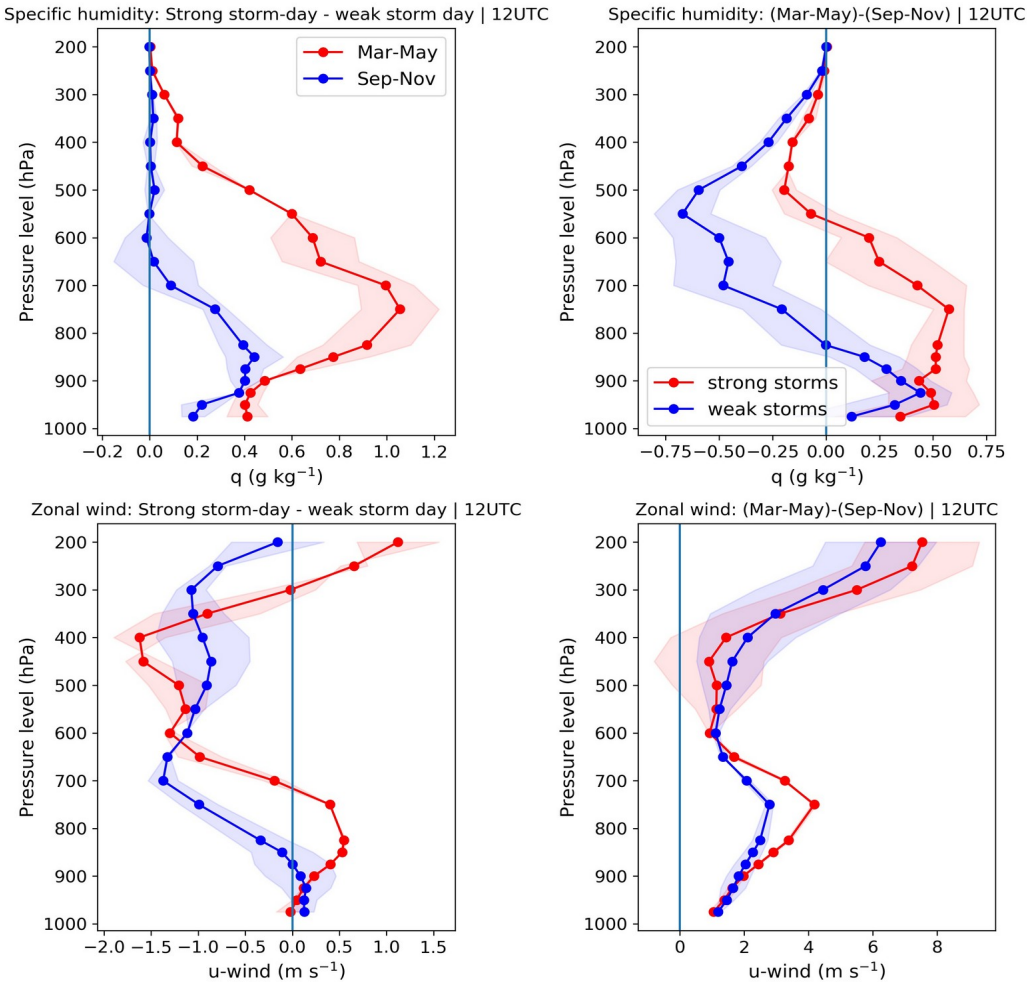

Figure 55. Difference in vertical profiles of 1200 UTC specific humidity (g kg^{-1} and zonal wind (m s^{-1}) composited on days with intense (coldest decile of mean MCS temperature) and weak (warmest decile of mean MCS temperature) MCSs for MAM (red) and SON (blue) on the left and for strong storms (red) and weak storms (blue) on the right .

Figure 55 compares different atmospheric drivers (specific humidity and zonal wind shear) at the event time scale for the most intense decile of

MCSs to the weakest decile of MCSs for both regimes. It can be observed that low-level moisture tend to be high during both rainy seasons. Moisture tend to reduce at mid-level through to high levels in the atmosphere. Mid-level moisture during MAM remained sligthly high for intense convection to take place. In comparing the two rainy seasons in terms of which season has higher moisture environment for storm intensities, it was realised that at low levels the early part of the first rainy season (MAM) had more moisture in the atmosphere than the SON season during both weak and strong storms. Easterly winds around 700hPa were intensified by 1.5 ms^{-1} during intense convection in the SON season. Higher levels in the atmosphere observed intense easterly winds of about 2 ms^{-1} in the early part of the first season of rains, therefore increasing the vertical shear conditions. This is usual of an environment with adequate instability and a strong shear. It showed that most intense storms in both seasons were fueled by similar atmospheric conditions although most storm systems during SON developed in an environment with abundant moisture condition. Moisture availability is observed to dominate the characteristics of MCS over SWA. It can be seen also that for more intense convection to occur, there should be abundance of low-level moisture, drier mid level and an increase in vertical shear due to intensified mid level easterly winds.

Chapter Summary

This chapter confirmed an intensification in the rainfall regime of SWA and also the dominating environmental conditions suitable for rainfall events in the two rainfall seasons over the region of study. Trends in MCS frequencies at different temperature thresholds and their influence on rainfall events are outlined, with an increasing trend in cold cloud temperatures depicting a regime of more intense rainfall. The sensitivity of MCS intensity and total rainfall to changes in wind shear in the pre-storm environment than to changes in low-level moisture during the first rainy season and the opposite happening in the second rainy season are clearly pointed out also in the chapter.

CHAPTER FIVE

SUMMARY, CONCLUSION AND RECOMMENDATIONS

Summary and Conclusion

As global intensification of the hydrological cycle has started over the long term with global warming, the possibility of detecting changes in the hydrological cycle at regional scales remains a challenge for the scientific community. Yet it is at these regional scales that adaptation strategies could be implemented and should enable a better understanding of the risks associated with hydrological extremes, whether due to droughts or floods. Africa, and in particular the West African region, appears to be a region of the world where these questions of the evolution of the hydrological cycle are the most critical. Recognized as one of the climatic hot spots due to its high sensitivity to global warming, this region is also recognized as one of the most vulnerable from a socio-economic point of view to climate variability. The subsistence of populations largely depend on rain-fed agriculture. The exponential growth of urban populations leaves little room for planning and the possibility of protecting urban populations from extreme rainfall events and floods.

The scientific challenges of documenting trends in the hydrological cycle in the WA region are multifaceted. First, they lie in the regional specificities of a highly variable climate for which trend signals are sometimes weak compared to the high intrinsic variability of the climate. Added to this is the difficulty of collecting sufficient data to document these signals. These constraints specific to the region all the more justify opting for robust scientific approaches which, in the dynamics of international climate research, must combine advanced statistical approaches to detect the weak signals in the

data and physical approaches to analyse the underlying mechanisms. It is in such an approach that this thesis work particularly focuses on the rainfall regime of the SWA, which is much less documented in the literature than its related region. A consistent and unique dataset has been compiled from in-situ and satellite data covering the study area densely at daily resolutions. This dataset allows to document the recent evolution of the precipitation regime at the scale of monsoon storms.

In determining the presence of an intensification in rainfall regime over SWA, rain gauge data from 97 stations for the period of 1970 – 2014 were used. An intensification was clearly observed over the SWA region with latitudinal variations while the occurrence of rainfall events seem to be stable. Recent studies, pointed out the latitudinal dependence of total rainfall on convective systems, with local thunderstorms dominating the rainfall fraction at the coast (Maranan et al., 2018); Acheampong, 1982; Omotosho, 1985) and long-lived, organized convective systems dominating in the sudanian region further north. Intensification in rainfall events over SWA was mainly due to significant increases in mean intensities of wet days with little or no increase in number of wet days. This is more pronounced in the Coastal and Inland regions than Sudan, which shares boundaries with the Sahel. This extends the results obtained by Sanogo et al. (2015), and suggests a trend towards more intense rainfall in SWA in the last decade with a seemingly steady occurrence of rainfall events. These trends appear to be similar to patterns observed over the Sahel region, with (Panthou et al., 2018; Panthou et al., 2014; Sanogo et al., 2015; Taylor et al., 2017) indicating similar intensification of rainfall events. A similar analysis of precipitation extremes in tropical Singapore has

been recently reported with some methodological and meteorological similarities (Li et al., 2018). One notable outcome in the analysis of seasonal trends is the change observed between the two rainfall seasons over the study region. Amidst a steady trend in annual rainfall in recent years over the AMJJ rainfall period, the intensity of the events have been increasing significantly in both the Coastal and Inland regions. This is in agreement with Taylor et al. (2017) indicating that the intensification signal of MCSs emerges above the strong decadal variability of total rainfall even in SWA during the boreal spring, aiding unusual cumulative rainfall (Taylor et al., 2017). The recent intensification of the rainfall regime generated the concern of the likely changes in the spatial extent and organization of MCSs. The second rainfall season also realized similar trends in rainfall regime as compared to the AMJJ season, although the Coastal region records a unique pattern during the 90's. The SON season realised liitle hyro-climatic intensification due to significant increases in number of wet days as the mean intesity of wet days increased (Giogi et al., 2011).

In examining the interannual variability and trends in MCSs and their drivers, MCS trends in SWA and their dynamic and thermo-dynamic drivers and their evolution over the last thirty years were evaluated. While Taylor et al. (2017) detected a tripling of extreme MCSs in the Sahel (Taylor et al., 2017), an underlying question was whether mechanisms similar to those identified by Taylor et al. (2017) may also have contributed to the intensification of rainfall in SWA. The diurnal passage of MCS trends showed that the first rainy season (AMJJ) observed a more westward propagation (portraying attributes of long lived storms), with storm trends in the second

rainy season (SON) not traveling far enough west. The SON season also showed stronger positive trends in recent MCS frequencies mainly over the coastal region, although the general outlook suggested a decrease of the contribution of MCSs to rainfall totals over SWA during the southward propagation (Fink et al., 2006). It was obvious during the diurnal passage that MCS frequencies intensify around 1800 UTC in both rainy seasons, with rainfall trends over SWA taking on more of the appearance of MCS trends at 1800 UTC. MCSs over SWA were mainly influenced by positive trends in wind shear in the early first rainy season from February to May. This behaviour looked different from June onwards with the inter-annual variability more strongly controlled by the availability of moisture which creates adequate instability due to high moist static energy (MSE). The second rainy season which exhibited strong low-level moisture also demonstrated a weaker wind shear due to the position of the African Easterly Jet. The AEJ was predominantly located north of SWA during the most intense MCS events, which agrees with observations from Mohr & Thorncroft (2006), who found that the most intense convective systems occurred south of the jet axis in September (Mohr & Thorncroft, 2006). It is worth noting that the passage of the African Easterly Jet from its southernmost position to its northernmost position caused a decline in the contribution of intense MCSs over the course of the year. This agrees with Maranan et al. (2018), who quantified MCS distribution and other rainfall types and observed that the deepest, most organised MCSs occur in MAM (early first rainy season), whilst MCSs with lower cloud tops and isolated storms dominate the SON season (Maranan et al., 2018). It can be said that an observation of the WAM cycle depicts that

MCSs that develop over SWA from late February to May to be the most convectively intense. The SON season on the other hand, sees the development of MCS peak around the same as the mean total rainfall.

Considering the effect of pre-convective environments, it can be clearly seen that changes occuring in both wind shear and atmospheric moisture play a role for MCS trends in SWA. The coldest cloud tops (intense MCSs) for both rainy seasons occur mostly under similar conditions although there exists a change in convective regime. In particular, MCS intensity and total rainfall is more sensitive to changes in wind shear in the pre-storm environment than to changes in low-level moisture during the first rainy season. The opposite happens during the second rainy season. This demonstrate the abundant low-level moisture in SWA on days that favour MCS development and would be less pronounced in a drier environment. Convection develops towards regions of high MSE. Since high values of low-level MSE (equivalent to theta-e) imply high CAPE, areas of maximum MSE favour convection.

In understanding the relationship between trends in storm frequency and rainfall, it was concluded that rainfall events in the moist regime occurred more frequently due to weaker convective inhibition, less entrainment and adequate total column water vapour compared to the shear regime, and the occurring MCSs tend to be less intense (Maranan et al., 2018). Clearer relationships were observed between rainfall events and trends in MCS frequency in the Coastal region than in the inland region, prompting the obvious intensification in rainfall events in the Coastal region as trends in storm system frequencies increased. Over the Inland region, only the second

rainy season showed clear trend increases in rainfall events as MCS frequency increased, whilst the Coastal region observed increasing trends in the early part of the first rainy season and during the second rainy season with the early detection of increasing MCS frequencies over SWA. This is consistent with previous studies over the region which stated that while rainfall extremes showed increasing trends in both rainy seasons, rainfall totals only show a trend in the second rainy season (Sanogo et al. 2015; Nkrumah et al. 2019; Bichet and Diedhiou 2018). Since extremes are very likely linked to MCSs, it gives confidence that all these studies identify robust trends in daily extreme rainfall characteristics. Depending on season, about 56% - 71% of SWA total rainfall comes from MCSs with increasing contribution away from the coast (Maranan et al., 2018). Consequently, the translation of MCS intensification trends into total rainfall trends is likely affected by other types of rain events such as isolated convection, warm-rain events, and stratiform rain.

Recommendations

To fully put this research into perspective, there will be the need to address these scientific opportunities:

To deepen the characterization of monsoon storms and their recent trends at finer (sub-day) scales and to refine the understanding of the physical mechanisms of intensification. In view of the mechanisms identified from the thesis data, there is now a need for a better understanding of the future evolution of the rainfall regime and in particular of the most extreme storms. The use of advanced regional atmospheric models with explicit convection schemes such as CP4-Africa have great potential in this respect. However, these new simulations need to be compared with global climate models, which to date are the only ones capable of projecting global warming under different greenhouse gas emission scenarios.

REFERENCES

Abiodun, B. J., Pal, J. S., Afiesimama, E. A., Gutowski, W. J., & Adedoyin, A. (2008). Simulation of West African monsoon using RegCM3 Part II: impacts of deforestation and desertification. *Theoretical and Applied Climatology*, *93*(3–4), 245–261.

Abiodun, B. J., Adeyewa, Z. D., Oguntunde, P. G., Salami, A. T., & Ajayi, V. O. (2012). Modeling the impacts of reforestation on future climate in West Africa. *Theoretical and Applied Climatology*, *110*(1-2), 77-96.

Acheampong, P. K. (1982). Rainfall anomaly along the coast of Ghana—Its nature and causes. *Geografiska Annaler: Series A, Physical Geography*, *64*(3–4), 199–211.

Alexander, L. V., Zhang, X., Peterson, T. C., Caesar, J., Gleason, B., Klein Tank, A. M. G., ... & Tagipour, A. (2006). Global observed changes in daily climate extremes of temperature and precipitation. *Journal of Geophysical Research: Atmospheres*, *111*(D5).

Alfaro, D. A. (2017). Low-tropospheric shear in the structure of squall lines: Impacts on latent heating under layer-lifting ascent. *Journal of the Atmospheric Sciences*, *74*(1), 229–248.

Alpert, P., Ben - Gai, T., Baharad, A., Benjamini, Y., Yekutieli, D., Colacino, M., ... & Michaelides, S. (2002). The paradoxical increase of Mediterranean extreme daily rainfall in spite of decrease in total values. *Geophysical research letters*, *29*(11), 31-1.

American Meteorological Society. Meteorology Glossary. URL glossary.ametsoc.org/ . Accessed:17-6-2019.

Balme-Debionne, M. (2004). *Analyse du régime pluviométrique sahélien dans une perspective hydrologique et agronomique: étude de l'impact de sa variabilité sur la culture du mil*. Grenoble INPG: Doctoral dissertation.

Berry, G. J., & Thorncroft, C. (2005). Case study of an intense African easterly wave. *Monthly Weather Review*, *133*(4), 752–766.

Bichet, A., & Diedhiou, A. (2018). Less frequent and more intense rainfall along the coast of the Gulf of Guinea in West and Central Africa. *Climate Research*, *76*(3), 191–201.

Blanchet, J., Molinié, G., & Touati, J. (2018). Spatial analysis of trend in extreme daily rainfall in southern France. *Climate Dynamics*, *51*(3), 799–812.

Burpee, R. W. (1974). Characteristics of North African easterly waves during the summers of 1968 and 1969. *Journal of the Atmospheric Sciences*, *31*(6), 1556–1570.

Burpee, R. W. (1972). The origin and structure of easterly waves in the lower troposphere of North Africa. *Journal of the Atmospheric Sciences*, *29*(1), 77–90.

Camberlin, P., Janicot, S., & Poccard, I. (2001). Seasonality and atmospheric dynamics of the teleconnection between African rainfall and tropical sea-surface temperature: Atlantic vs. *ENSO*. *International Journal of*

Climatology: A Journal of the Royal Meteorological Society, *21*(8), 973–1005.

Change, I. C. (2014). *Mitigation of climate change. Contribution of Working Group III to the Fifth Assessment Report of the Intergovernmental Panel on Climate Change*.

Charney, J. G., & Stern, M. E. (1962). On the stability of internal baroclinic jets in a rotating atmosphere. *Journal of the Atmospheric Sciences*, *19*(2), 159–172.

Cornforth, R. J. (2013). West african monsoon 2012. *Weather*, *68*(10), 256–263.

Dee, D. P., Uppala, S. M., Simmons, A. J., Berrisford, P., Poli, P., Kobayashi, S., & Bechtold, P. (2011). The ERA-Interim reanalysis: Configuration and performance of the data assimilation system. *Quarterly Journal of the Royal Meteorological Society*, *137*(656), 553–597.

Diatta, S., & Fink, A. H. (2014). Statistical relationship between remote climate indices and West African monsoon variability. *International Journal of Climatology*, *34*(12), 3348–3367.

Dirmeyer, P. A., Gao, X., Zhao, M., Guo, Z., Oki, T., & Hanasaki, N. (2006). GSWP-2: Multimodel analysis and implications for our perception of the land surface. *Bulletin of the American Meteorological Society*, *87*(10), 1381–1398.

Donat, M. G., Lowry, A. L., Alexander, L. V, O'Gorman, P. A., & Maher, N. (2016). More extreme precipitation in the world's dry and wet regions. *Nature Climate Change*, *6*(5), 508–513.

Doswell III, C. A., Brooks, H. E., & Maddox, R. A. (1996). Flash flood forecasting: An ingredients-based methodology. *Weather and Forecasting*, *11*(4), 560–581.

Douville, H., Conil, S., Tyteca, S., & Voldoire, A. (2007). Soil moisture memory and West African monsoon predictability: artefact or reality? *Climate Dynamics*, *28*(7–8), 723–742.

Efron, B., & Tibshirani, R. J. (1994). *An introduction to the bootstrap*. CRC press.

El Houssein, T. A. L. E. B., & Decleir, H. (1998). Upper air characteristics of wet and dry days in tropical West Africa during the rainy season. *IAHS-AISH publication*, 55-62.

Eltahir, E. A., & Gong, C. (1996). Dynamics of wet and dry years in West Africa. *Journal of Climate*, *9*(5), 1030–1042.

Federal Aviation Administration, 1987, Wind-shear Training Aid, Washington, DC.

Fink, A. H., & Reiner, A. (2003). Spatiotemporal variability of the relation between African easterly waves and West African squall lines in 1998 and 1999. *Journal of Geophysical Research: Atmospheres*, *108*(D11).

Fink, A. H., Vincent, D. G., & Ermert, V. (2006). Rainfall types in the West African Sudanian zone during the summer monsoon 2002. *Monthly Weather Review*, *134*(8), 2143–2164.

Flaounas, E., Bastin, S., & Janicot, S. (2011. Regional climate modelling of the 2006 West African monsoon: sensitivity to convection and planetary boundary layer parameterisation using WRF. *Climate Dynamics*, *36*(5–6), 1083–1105.

Fontaine, B., Garcia-Serrano, J., Roucou, P., Rodriguez-Fonseca, B., Losada, T., Chauvin, F., & Janicot, S. (2010). Impacts of warm and cold situations in the Mediterranean basins on the West African monsoon: observed connection patterns (1979–2006) and climate simulations. *Climate Dynamics*, *35*(1), 95–114.

Fontaine, B., & Janicot, S. (1996). Sea surface temperature fields associated with West African rainfall anomaly types. *Journal of Climate*, *9*(11), 2935–2940.

Fontaine, B., & Janicot, S. (1992). Wind-field coherence and its variations over West Africa. *Journal of Climate*, *5*(5), 512–524.

Frich, P., Alexander, L. V, Della-Marta, P. M., Gleason, B., Haylock, M., Tank, A. K., & Peterson, T. (2002). Observed coherent changes in climatic extremes during the second half of the twentieth century. *Climate Research*, *19*(3), 193–212.

Friesen, J., & Diekkriuger, B. (2002). *Spatio-temporal rainfall patterns in Northern Ghana*. Bonn.

Fujita, T.T. (1985). Downburst: microburst and macroburst. Report of Projects NIMROD and JAWS. *Satellite and Micrometeorology Research Project paper- 210, Univ. of Chicago, Chicago, IL*, 122pp

Futyan, J. M., & Del Genio, A. D. (2007). Deep convective system evolution over Africa and the tropical Atlantic. *Journal of Climate*, *20*(20), 5041–5060.

Giannini, A., Saravanan, R., & Chang, P. (2005). Dynamics of the boreal summer African monsoon in the NSIPP1 atmospheric model. *Climate Dynamics*, *25*(5), 517–535.

Giannini, A., Saravanan, R., & Chang, P. (2003). Oceanic forcing of Sahel rainfall on interannual to interdecadal time scales. *Science*, *302*(5647), 1027–1030.

Giorgi, F., Im, E. S., Coppola, E., Diffenbaugh, N. S., Gao, X. J., Mariotti, L., & Shi, Y. (2011). Higher hydroclimatic intensity with global warming. *Journal of Climate*, *24*(20), 5309-5324.

Grist, J. P., & Nicholson, S. E. (2001). A study of the dynamic factors influencing the rainfall variability in the West African Sahel. *Journal of Climate*, *14*(7), 1337–1359.

Groisman, P. Y., Knight, R. W., & Karl, T. R. (2001). Heavy precipitation and high streamflow in the contiguous United States: Trends in the twentieth century. *Bulletin of the American Meteorological Society*, *82*(2), 219–246.

Gu, G., Adler, R. F., Huffman, G. J., & Curtis, S. (2004). African easterly waves and their association with precipitation. *Journal of Geophysical Research: Atmospheres*, *109*(D4).

Hall, N. M., Kiladis, G. N., & Thorncroft, C. D. (2006). Three-dimensional structure and dynamics of African easterly waves. Part II: Dynamical modes. *Journal of the Atmospheric Sciences*, *63*(9), 2231–2245.

Hartmann, D. L. (1994). *Global Physical Climatology (International geophysics; v*. Academic Press.

Hastenrath, S. (1991). Diurnal forcings and local circulations. In *Climate dynamics of the tropics* (pp. 6–24). Dordrecht: Springer.

Hastenrath, S. (1991). Regional circulation systems. In *Climate dynamics of the tropics* (pp. 114–218). Dordrecht: Springer.

Hayward, D. F., & Oguntoyinbo, J. S. (1987). *Climatology of West Africa*. Rowman & Littlefield.

Hodges, K. I., & Thorncroft, C. D. (1997). Distribution and statistics of African mesoscale convective weather systems based on the ISCCP Meteosat imagery. *Monthly Weather Review*, *125*(11), 2821–2837.

Holton, J. R. (2004). Synoptic-scale motions I: quasi-geostrophic analysis. In F. Cynar (Ed.), *An introduction to dynamic meteorology* (4th edn, pp. 139–176). Amsterdam: Elsevier Academic Press.

Houghton, J. T., Ding, Y. D. J. G., Griggs, D. J., Noguer, M., Linden, P. J., Dai, X., & Johnson, C. A. (2001). *Climate change 2001: the scientific basis*. The Press Syndicate of the University of Cambridge.

Hountondji, Y., De Longueville, F., & Ozer, P. (2011). Trends in extreme rainfall events in Benin (West Africa), 1960-2000. *Proceedings of the 1st International Conference on Energy, Environment and Climate Change*.

Houze Jr, R. A., Rutledge, S. A., Biggerstaff, M. I., & Smull, B. F. (1989). Interpretation of Doppler weather radar displays of midlatitude mesoscale convective systems. *Bulletin of the American Meteorological Society*, *70*(6), 608-619.

Houze Jr, R. A. (1989). Observed structure of mesoscale convective systems and implications for large - scale heating. *Quarterly Journal of the Royal Meteorological Society*, *115*(487), 425-461.

Houze Jr, R. A. (2004). Mesoscale convective systems. *Reviews of Geophysics*, *42*(4).

Huntington, T. G. (2006). Evidence for intensification of the global water cycle: review and synthesis. *Journal of Hydrology*, *319*(1–4), 83–95.

I.P.C.C. (2013). Climate Change 2013: The Physical Science Basis. An overview of the Working Group 1 contribution to the Fifth Assessment Report of the Intergovernmental Panel on Climate Change (IPCC. *EGU General Assembly Conference Abstracts*, *16*.

Jackson, B., Nicholson, S. E., & Klotter, D. (2009). Mesoscale convective systems over western equatorial Africa and their relationship to large-scale circulation. *Monthly Weather Review*, *137*(4), 1272–1294.

Janicot, S., Trzaska, S., & Poccard, I. (2001). Summer Sahel-ENSO teleconnection and decadal time scale SST variations. *Climate Dynamics*, *18*(3–4), 303–320.

Janicot, S., Caniaux, G., Chauvin, F., De Coëtlogon, G., Fontaine, B., Hall, N., ... & Taylor, C. M. (2011). Intraseasonal variability of the West African monsoon. *Atmospheric Science Letters*, *12*(1), 58-66.

Janiga, M. A., & Thorncroft, C. D. (2016). The influence of African easterly waves on convection over tropical Africa and the east Atlantic. *Monthly Weather Review*, *144*(1), 171–192.

Jirak, I. L., & Cotton, W. R. (2007). Observational analysis of the predictability of mesoscale convective systems. *Weather and Forecasting*, *22*(4), 813–838.

Jirak, I. L., Cotton, W. R., & McAnelly, R. L. (2003). Satellite and radar survey of mesoscale convective system development. *Monthly Weather Review*, *131*(10), 2428–2449.

Kamara, S. I. (1986). The origins and types of rainfall in West Africa. *Weather*, *41*(2), 48–56.

Kingston, D. G., Todd, M. C., Taylor, R. G., Thompson, J. R., & Arnell, N. W. (2009). Uncertainty in the estimation of potential evapotranspiration under climate change. *Geophysical Research Letters*, *36*(20).

Klein, C., Nkrumah, F., Taylor, C. M., & Adefisan, E. A. (2021). Seasonality and Trends of Drivers of Mesoscale Convective Systems in Southern West Africa. *Journal of Climate*, *34*(1), 71-87.

Koster, R. D., Dirmeyer, P. A., Guo, Z., Bonan, G., Chan, E., Cox, P., & Liu, P. (2004). Regions of strong coupling between soil moisture and precipitation. *Science*, *305*(5687), 1138–1140.

Kuettner, J. P. (1974). General description and central program of GATE. *Bull. Amer. Meteor. Soc*, *55*(7), 712–719.

Kundzewicz, Z. W., Kanae, S., Seneviratne, S. I., Handmer, J., Nicholls, N., Peduzzi, P., … Sherstyukov, B. (2013). Flood risk and climate change: global and regional perspectives. *Hydrological Sciences Journal*. https://doi.org/10.1080/02626667.2013.857411

Lafore, J. P., Chapelon, N., Diop, M., Gueye, B., Largeron, Y., Lepape, S., & Roehrig, R. (2017). Deep convection. In *Meteorology of tropical West Africa: The forecasters' handbook* (pp. 90–129).

Laing, A. G., Carbone, R., Levizzani, V., & Tuttle, J. (2008). The propagation and diurnal cycles of deep convection in northern tropical Africa. *Quarterly Journal of the Royal Meteorological Society: A Journal of the Atmospheric Sciences, Applied Meteorology and Physical Oceanography*, *134*(630), 93–109.

Laing, A. G., Fritsch, J. M., & Negri, A. J. (1999). Contribution of mesoscale convective complexes to rainfall in Sahelian Africa: Estimates from

geostationary infrared and passive microwave data. *Journal of Applied Meteorology*, *38*(7), 957–964.

Laing, A., & Evans, J. L. (2011). Introduction to tropical meteorology. *Educational material from The COMET Program*.

Lamb, P. J. (1978). Case studies of tropical Atlantic surface circulation patterns during recent sub-Saharan weather anomalies: 1967 and 1968. *Monthly Weather Review*, *106*(4), 482–491.

Le Barbé, L., Lebel, T., & Tapsoba, D. (2002). Rainfall variability in West Africa during the years 1950–90. *Journal of Climate*, *15*(2), 187–202.

Lebel, T., & Ali, A. (2009). Recent trends in the Central and Western Sahel rainfall regime (1990–2007. *Journal of Hydrology*, *375*(1–2), 52–64.

Lebel, T., Diedhiou, A., & Laurent, H. (2003). Seasonal cycle and interannual variability of the Sahelian rainfall at hydrological scales. *Journal of Geophysical Research: Atmospheres*, *108*(D8).

Lebel, T., Parker, D. J., Flamant, C., Bourlès, B., Marticoréna, B., Mougin, E., & Polcher, J. (2010). The AMMA field campaigns: multiscale and multidisciplinary observations in the West African region. *Quarterly Journal of the Royal Meteorological Society*, *136*(S1), 8–33.

Leroux, S., & Hall, N. M. (2009). On the relationship between African easterly waves and the African easterly jet. *Journal of the Atmospheric Sciences*, *66*(8), 2303–2316.

Li, X., Wang, X., & Babovic, V. (2018). Analysis of variability and trends of precipitation extremes in Singapore during 1980–2013. *International Journal of Climatology*, *38*(1), 125–141.

Lindzen, R. S., & Nigam, S. (1987). On the role of sea surface temperature gradients in forcing low-level winds and convergence in the tropics. *Journal of the Atmospheric Sciences*, *44*(17), 2418–2436.

Losada, T., Rodríguez-Fonseca, B., Janicot, S., Gervois, S., Chauvin, F., & Ruti, P. (2010). A multi-model approach to the Atlantic Equatorial mode: impact on the West African monsoon. *Climate Dynamics*, *35*(1), 29–43.

Maddox, R. A. (1980). Mesoscale convective complexes. *Bulletin of the American Meteorological Society*, 1374–1387.

Maddox, R. A., Chappell, C. F., & Hoxit, L. R. (1979). Synoptic and meso-α scale aspects of flash flood events. *Bulletin of the American Meteorological Society*, *60*(2), 115–123.

Maidment, R. I., Allan, R. P., & Black, E. (2015). Recent observed and simulated changes in precipitation over Africa. *Geophysical Research Letters*, *42*(19), 8155–8164.

Mann, H. B., & Whitney, D. R. (1947). On a test of whether one of two random variables is stochastically larger than the other. In *The annals of mathematical statistics* (pp. 50–60).

Maranan, M., Fink, A. H., & Knippertz, P. (2018). Rainfall types over southern West Africa: Objective identification, climatology and

synoptic environment. *Quarterly Journal of the Royal Meteorological Society*, *144*(714), 1628–1648.

Market, P., Allen, S., Scofield, R., Kuligowski, R., & Gruber, A. (2003). Precipitation efficiency of warm-season Midwestern mesoscale convective systems. *Weather and Forecasting*, *18*(6), 1273–1285.

Mathon, V., & Laurent, H. (2001). Life cycle of Sahelian mesoscale convective cloud systems. *Quarterly Journal of the Royal Meteorological Society*, *127*(572), 377–406.

Mathon, V., Laurent, H., & Lebel, T. (2002). Mesoscale convective system rainfall in the Sahel. *Journal of Applied Meteorology*, *41*(11), 1081–1092.

Menzel, W. P., & Satellite, N. O. A. A. (2005). Remote sensing applications with meteorological satellites. *The Solar Spectrum*, *3*(10).

Met Office. Learn about weather. URL https://www.metoffice.gov.uk/. Accessed: 17-6-2019.

Meynadier, R., Bock, O., Guichard, F., Boone, A., Roucou, P., & Redelsperger, J. L. (2010). West African Monsoon water cycle: 1. A hybrid water budget data set. *Journal of Geophysical Research: Atmospheres*, *115*(D19).

Min, S. K., Zhang, X., Zwiers, F. W., & Hegerl, G. C. (2011). Human contribution to more-intense precipitation extremes. *Nature*, *470*(7334), 378–381.

Mohr, K. I. (2004). Interannual, monthly, and regional variability in the wet season diurnal cycle of precipitation in sub-Saharan Africa. *Journal of Climate*, *17*(12), 2441–2453.

Mohr, K. I., & Thorncroft, C. D. (2006). Intense convective systems in West Africa and their relationship to the African easterly jet. *Quarterly Journal of the Royal Meteorological Society: A Journal of the Atmospheric Sciences, Applied Meteorology and Physical Oceanography*, *132*(614), 163–176.

Murakami, M. (1979). Large-scale aspects of deep convective activity over the GATE area. *Monthly Weather Review*, *107*(8), 994–1013.

Murray, S. J., Foster, P. N., & Prentice, I. C. (2011). Evaluation of global continental hydrology as simulated by the Land-surface Processes and eXchanges Dynamic Global Vegetation Model. *Hydrology and Earth System Sciences*, *15*, 91–105.

Nesbitt, S. W., Cifelli, R., & Rutledge, S. A. (2006). Storm morphology and rainfall characteristics of TRMM precipitation features. *Monthly Weather Review*, *134*(10), 2702–2721.

Nguyen, H., Thorncroft, C. D., & Zhang, C. (2011). Guinean coastal rainfall of the West African Monsoon. *Quarterly Journal of the Royal Meteorological Society*, *137*(660), 1828–1840.

Nicholson, S. E. (2009). A revised picture of the structure of the “monsoon” and land ITCZ over West Africa. *Climate Dynamics*, *32*(7–8), 1155–1171.

Nicholson, S. E. (1981). Rainfall and atmospheric circulation during drought periods and wetter years in West Africa. *Monthly Weather Review*, *109*(10), 2191–2208.

Nicholson, S. E. (2013). The West African Sahel: A review of recent studies on the rainfall regime and its interannual variability. *ISRN Meteorology*.

Nkrumah, F., Vischel, T., Panthou, G., Klutse, N. A. B., Adukpo, D. C., & Diedhiou, A. (2019). Recent Trends in the Daily Rainfall Regime in Southern West Africa. *Atmosphere*, *10*(12), 741.

Noble, E., Druyan, L. M., & Fulakeza, M. (2014). The sensitivity of WRF daily summertime simulations over West Africa to alternative parameterizations. *Part I: African Wave Circulation. Monthly Weather Review*, *142*(4), 1588–1608.

Norman, J. M., & Becker, F. (1995). Terminology in thermal infrared remote sensing of natural surfaces. *Remote Sensing Reviews, 12(3-4), 159–173*. doi:10.1080/02757259509532284

O'Gorman, P. A. (2015). Precipitation extremes under climate change. *Current Climate Change Reports*, *1*(2), 49–59.

Omotosho, J. (1985). The separate contributions of line squalls, thunderstorms and the monsoon to the total rainfall in Nigeria. *Journal of Climatology*, *5*(5), 543–552.

Paeth, H., Hall, N. M., Gaertner, M. A., Alonso, M. D., Moumouni, S., Polcher, J., & Gaye, A. T. (2011). Progress in regional downscaling of West African precipitation. *Atmospheric Science Letters*, *12*(1), 75–82.

Panthou, G., Lebel, T., Vischel, T., Quantin, G., Sane, Y., Ba, A., … Diopkane, M. (2018). Rainfall intensification in tropical semi-arid regions: The Sahelian case. *Environmental Research Letters*, *13*(6). https://doi.org/10.1088/1748-9326/aac334

Panthou, G., Vischel, T., & Lebel, T. (2014). Recent trends in the regime of extreme rainfall in the Central Sahel. *International Journal of Climatology*, *34*(15), 3998–4006.

Panthou, G., Vischel, T., Lebel, T., Blanchet, J., Quantin, G., & Ali, A. (2012). Extreme rainfall in West Africa: A regional modeling. *Water Resources Research*, *48*(8).

Parker, D. J., Thorncroft, C. D., Burton, R. R., & Diongue-Niang, A. (2005). Analysis of the African easterly jet, using aircraft observations from the JET2000 experiment. *Quarterly Journal of the Royal Meteorological Society: A Journal of the Atmospheric Sciences, Applied Meteorology and Physical Oceanography*, *131*(608), 1461–1482.

Parker, M. D., & Johnson, R. H. (2000). Organizational modes of midlatitude mesoscale convective systems. *Monthly Weather Review*, *128*(10), 3413–3436.

Peters, J. M., & Schumacher, R. S. (2014). Objective categorization of heavy-rain-producing MCS synoptic types by rotated principal component analysis. *Monthly Weather Review*, *142*(5), 1716–1737.

Pytharoulis, I., & Thorncroft, C. (1999). The low-level structure of African easterly waves in 1995. *Monthly Weather Review*, *127*(10), 2266–2280.

Sanogo, S., Fink, A. H., Omotosho, J. A., Ba, A., Redl, R., & Ermert, V. (2015). Spatio-temporal characteristics of the recent rainfall recovery in West Africa. *International Journal of Climatology*, *35*(15), 4589–4605. https://doi.org/10.1002/joc.4309

Schrage, J. M., Fink, A. H., Ermert, V., & Ahlonsou, E. D. (2006). Three MCS cases occurring in different synoptic environments in the sub-Sahelian wet zone during the 2002 West African monsoon. *Journal of the Atmospheric Sciences*, *63*(9), 2369–2382.

Schumacher, R. S., & Johnson, R. H. (2006). Characteristics of US extreme rain events during 1999–2003. *Weather and Forecasting*, *21*(1), 69–85.

Schumacher, R. S., & Johnson, R. H. (2005). Organization and environmental properties of extreme-rain-producing mesoscale convective systems. *Monthly Weather Review*, *133*(4), 961–976.

Selase, A. E., Agyimpomaa, D. E., Selasi, D. D., & Hakii, D. M. (2015). Precipitation and rainfall types with their characteristic features. *Journal of Natural Science Research*, *5*(20), 89-92.

Smull, B. F., & Houze Jr, R. A. (1987). Rear inflow in squall lines with trailing stratiform precipitation. Monthly weather review, 115(12), 2869-2889.

So, D & Shin, D. B (2018). Classification of precipitating clouds using satellite infrared observations and its implications for rainfall estimation. Q J R Meteorol Soc 2018;144 (Suppl. 1):133–144. https://doi.org/10.1 002/q j. 3288

Stensrud, D. J., & Fritsch, J. M. (1993). Mesoscale convective systems in weakly forced large-scale environments. *Part I: Observations. Monthly Weather Review*, *121*(12), 3326–3344.

Stephens, G. L., & Kummerow, C. D. (2007). The remote sensing of clouds and precipitation from space: A review. *Journal of the Atmospheric Sciences*, *64*(11), 3742–3765.

Taylor, C M, Fink, A. H., Klein, C., Parker, D. J., Guichard, F., Harris, P. P., & Knapp, K. R. (2018). Earlier seasonal onset of intense mesoscale convective systems in the Congo Basin since 1999. *Geophysical Research Letters*, *45*(24), 13–458.

Taylor, C. M., Lambin, E. F., Stephenne, N., Harding, R. J., & Essery, R. L. (2002). The influence of land use change on climate in the Sahel. *Journal of Climate*, *15*(24), 3615–3629.

Taylor, C. M., Parker, D. J., Kalthoff, N., Gaertner, M. A., Philippon, N., Bastin, S., & Baldi, M. (2011). New perspectives on land–atmosphere

feedbacks from the African Monsoon Multidisciplinary Analysis. *Atmospheric Science Letters*, *12*(1), 38–44.

Taylor, C. M., Belusic, D., Guichard, F., Parker, D. J., Vischel, T., Bock, O., … Panthou, G. (2017). Frequency of extreme Sahelian storms tripled since 1982 in satellite observations. *Nature*, *544*(7651), 475–478. https://doi.org/10.1038/nature22069

Thorncroft, C. D., & Blackburn, M. (1999). Maintenance of the African easterly jet. *Quarterly Journal of the Royal Meteorological Society*, *125*(555), 763–786.

Thorncroft, C. D., Hall, N. M., & Kiladis, G. N. (2008). Three-dimensional structure and dynamics of African easterly waves. *Part III: Genesis. Journal of the Atmospheric Sciences*, *65*(11), 3596–3607.

Thorncroft, C. D., Nguyen, H., Zhang, C., & Peyrillé, P. (2011). Annual cycle of the West African monsoon: regional circulations and associated water vapour transport. *Quarterly Journal of the Royal Meteorological Society*, *137*(654), 129–147.

Thorncroft, C. D., Parker, D. J., Burton, R. R., Diop, M., Ayers, J. H., Barjat, H., & Price, N. M. (2003). The JET2000 project: aircraft observations of the African easterly jet and African easterly waves: aircraft observations of the African easterly jet and African easterly waves. *Bulletin of the American Meteorological Society*, *84*(3), 337–352.

Tschakert, P., Sagoe, R., Ofori-Darko, G., & Codjoe, S. N. (2010). Floods in the Sahel: an analysis of anomalies, memory, and anticipatory learning. *Climatic Change*, *103*(3–4), 471–502.

Uppala, S. M., Kållberg, P. W., Simmons, A. J., Andrae, U., Bechtold, V. D. C., Fiorino, M., & Li, X. (2005). The ERA-40 re-analysis. *Quarterly Journal of the Royal Meteorological Society: A Journal of the Atmospheric Sciences, Applied Meteorology and Physical Oceanography*, *131*(612), 2961–3012.

Vizy, E. K., & Cook, K. H. (2001). Mechanisms by which Gulf of Guinea and eastern North Atlantic sea surface temperature anomalies can influence African rainfall. *Journal of Climate*, *14*(5), 795–821.

Vizy, E. K., & Cook, K. H. (2017). Seasonality of the observed amplified Sahara warming trend and implications for Sahel rainfall. *Journal of Climate*, *30*(9), 3073–3094.

Vollmert, P., Fink, A. H., & Besler, H. (2003). Ghana Dry Zone" und "Dahomey Gap": Ursachen für eine Niederschlagsanomalie im tropischen Westafrika. *Erde*, *134*(4), 375–393.

Weisman, M. L., & Klemp, J. B. (1984). The structure and classification of numerically simulated convective storms in directionally varying wind shears. *Monthly Weather Review*, *112*(12), 2479–2498.

Westra, S., Alexander, L. V, & Zwiers, F. W. (2013). Global increasing trends in annual maximum daily precipitation. *Journal of Climate*, *26*(11), 3904–3918.

Westra, S., Fowler, H. J., Evans, J. P., Alexander, L. V, Berg, P., Johnson, F., & Roberts, N. M. (2014). Future changes to the intensity and frequency of short-duration extreme rainfall. *Reviews of Geophysics*, *52*(3), 522–555.

Wilcoxon. (1945). Individual Comparisons by Ranking Methods. *Biometrics Bulletin*, 80–2.

World Meteorological Organisation. International Cloud Atlas: Manual on the Observation of Clouds and Other Meteors, 2017. URL https://cloudatlas.wmo.int/ .

Xue, Y., & Shukla, J. (1993). The influence of land surface properties on Sahel climate. Part 1: desertification. *Journal of Climate*, *6*(12), 2232–2245.

Xue, Y., & Shukla, J. (1996). The influence of land surface properties on Sahel climate. Part II. *Afforestation. Journal of Climate*, *9*(12), 3260–3275.

Yabi, I., & Afouda, F. (2012). Extreme rainfall years in Benin (West Africa. *Quaternary International*, *262*, 39–43.

Zaroug, M. A., Sylla, M. B., Giorgi, F., Eltahir, E. A., & Aggarwal, P. K. (2013). A sensitivity study on the role of the swamps of southern Sudan in the summer climate of North Africa using a regional climate model. *Theoretical and Applied Climatology*, *113*(1–2), 63–81.

Zeng, N., Neelin, J. D., Lau, K. M., & Tucker, C. J. (1999). Enhancement of interdecadal climate variability in the Sahel by vegetation interaction. *Science*, *286*(5444), 1537–1540.

Zipser, E. J. (1982). Use of a conceptual model of the life-cycle of mesoscale convective systems to improve very-short-range forecasts. Nowcasting.

PUBLICATIONS

Nkrumah, F., Vischel, T., Panthou, G., Klutse, N. A. B., Adukpo, D. C., & Diedhiou, A. (2019). Recent Trends in the Daily Rainfall Regime in Southern West Africa. *Atmosphere*, *10*(12), 741.